Amphiphile-coated magnetic iron oxide nanoparticles for the extraction of contaminants from the aqueous media

A dissertation submitted with the requirements for the degree

Magister Scientiae

in the

DEPARTMENT OF CHEMISTRY

FACULTY OF NATURAL and AGRICULTURAL SCIENCES

at the

UNIVERSITY OF THE FREE STATE

by

Viwe Mzinjani

Supervisor: Prof. VA Azov

Co-Supervisor: Dr EH Langner

2023

DECLARATION

I, Viwe Mzinjani declare that this work was written by me with the help of my supervisor and co-supervisor. It has never been submitted to any institution of higher learning for acquiring a degree.

_____

Signed by Mzinjani Viwe in Bloemfontein (January 2023)

ACKNOWLEDGEMENTS

I would like to acknowledge the following persons for the support they gave me during my MSc project at the University of the Free State.

Prof V. A. Azov and Dr E. H. Langner, my supervisors for guiding and helping me throughout the duration of the project.

My parents Lindelwa Mzinjani and Mxolisi Cebani for the words of encouragement when the going was getting tougher.

The BAM Group from the University of the Free State for moral support, pieces of advice, and technical assistance in the Laboratory.

Dr D. V. Kama for running my PXRD samples and Mr Yuel Abraha for TGA.

The University of the Free State Microscope Centre for performing TEM, SEM, and EDS analysis.

My friends for cheering me up when the chemistry was not working.

The University of the Free State for allowing me to use their equipments.

My funder, the Nanoscience program for making this project a success.

Iminyanya nezihlwele zamaTshezi namaCirha and the Almighty Lord for the strength they gave me to finish this project.

ABSTRACT

The availability of clean water to the community/ society is becoming a huge problem for its ecosystem. These toxic contaminants come from surface and subsurface water systems such as dams, rivers, and oceans that are eluted from industrial, domestic, agricultural, and recreational activities. Both organic and inorganic contaminants are found in these water systems in high concentrations, which put aquatic life at tremendous risk and the environment in general.

Thus, the need for synthetic materials that can be used to solve this ongoing problem of water contamination is becoming an obvious research goal that needs urgent attention. Nanomaterials such as nanoparticles are currently being investigated as a tool to remove various contaminants in wastewater.

Nanoparticles are very small particles with sizes ranging from 1 to 100 nm. Depending on their type, these nanomaterials may demonstrate various unique properties, such as strong catalytic activity, superparamagnetism, quantum confinement, and extremely high surface-to-volume ratios. In this project, the high surface-to-volume property was explored during the adsorption of methylene blue dye in spiked water samples. Magnetic iron oxide nanoparticles were chosen because of their magnetic susceptibility and most availability of iron metal on earth, making them cheaper materials since they can be prepared from cheap iron precursors. Magnetite NPs were prepared using the co-precipitation method, where iron precursors of Fe^{2+} and Fe^{3+} were dissolved in de-ionized water and ammonium hydroxide was used as the precipitating agent under an inert atmosphere.

Better adsorption capacities of these nanoparticles can be achieved by functionalizing them with different organic and inorganic molecules. In this study, mono-alkyl phosphate esters of varying alkyl chain lengths were synthesized and used to functionalize the as-synthesized magnetite NPs to render better affinity towards organic dyes (**Figure 1**).

The as-prepared magnetite NPs were characterized using techniques such as TEM, SEM, FTIR, EDS, and PXRD, and the organic functionalization molecules were characterized using NMR (^{1}H, ^{13}C, and ^{31}P), FTIR, and mass spectrometry. These characterization techniques confirmed the successful synthesis of the nanoparticles

and mono-alkyl phosphate esters of varying alkyl chain lengths. TEM and SEM micrographs showed close to spherical shapes of the prepared nanoparticles with particle diameters ranging from 12 – 16 nm for bare Fe_3O_4 NPs and 17 – 22 nm for functionalized NPs. Comparable particle size was also obtained from the PXRD results using the Scherrer equation (**eq. 3.1**) where a particle size of 13 nm was obtained. PXRD characteristic peaks confirmed the inverse spinel structure of the Fe_3O_4 NPs. The presence of iron (Fe) and oxygen (O) in the EDS results confirmed the formation of the magnetite nanoparticles and the presence of carbon (C) and phosphorus (P) on the coated nanoparticles confirmed the successful coating of the Fe_3O_4 NPs. FTIR, NMR, and MS results showed comparable results to those found in the literature.

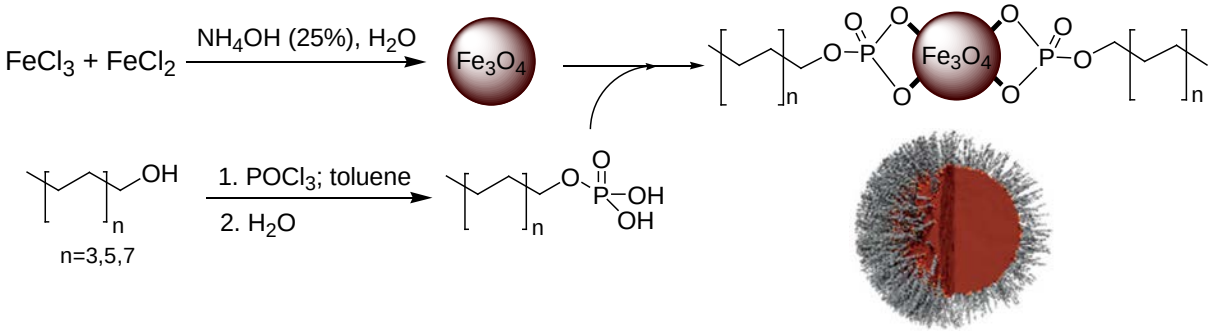

Figure 1: Reaction scheme for the synthesis of the magnetite nanoparticles, mono-alkyl phosphate esters, and coating of the nanoparticles with the esters.

The coated magnetite nanoparticles (**Figure 1**) were applied for the adsorption of MB dye. The optimum dye removal percentages of the as-synthesized nanoparticles were obtained at high temperatures (60 ^oC), with a pH of 10. Experimental adsorption capacities of 445, 329, 296, and 275 mg/g for Fe_3O_4@C16, Fe_3O_4@C12, Fe_3O_4@C8, and Fe_3O_4 Bare NPs, respectively were obtained showing that the longer the alkyl chain the better the affinity of the adsorbent for methylene blue via dispersion forces and hydrophobic effect. Experimental data fitted well the Langmuir isotherm model and the kinetic models were fitted with pseudo-second order showing better R^2 and adsorption capacities that were comparable to the experimentally obtained values.

TABLE OF CONTENTS

LIST OF FIGURES

LIST OF TABLES

ABBREVIATIONS

NPs – Nanoparticles

C8 – $C_8H_{17}O_4P$

C12 – $C_{12}H_{27}O_4P$

C16 – $C_{16}H_{35}O_4P$

TGA – Thermogravimetric analysis

EDS/ EDX – Energy Dispersive X-ray

TEM – Transmission Electron Microscopy

SEM – Scanning Electron Microscopy

UV/Vis – Ultraviolet-Visible Spectroscopy

FTIR – Fourier-Transform Infrared spectroscopy

NMR – Nuclear Magnetic Resonance Spectroscopy

PXRD – Powder X-ray Diffraction

BET Surface area – Brunauer-Emmett-Teller Surface area

MS – Mass Spectrometry

s – Singlet

d – Doublet

t – Triplet

q – Quartet

m – Multiplet

Chapter 1

Introduction

1.1 Background

Deposition of waste substances into subsurface groundwater, rivers, dams, oceans, *etc*. without a proper purification process leads to worldwide water pollution. Such harmful substances can come from agricultural, industrial, domestic, and recreational wastes. Healthy aquatic life and humans require clean water without any toxic or harmful impurities [1,2].

Nowadays, environmental pollution is becoming a major threat to the ecosystem [3]. Most research groups working in the field of environmental analysis report an increase in contamination levels in the environment (water, soil, and air) as an alarming factor for ecosystems all over the world [3–6]. The discharge of toxic substances into rivers from industrial activities and during agricultural runoffs without proper treatment leads to the contamination of the environment and aquatic life and poses tremendous risks. Organic (such as oils, pharmaceuticals, personal care products, and pesticides) and inorganic (such as metal ions) compounds and bacteria are the common toxic contaminants that pollute our water systems [7].

Researchers around the world are trying to find materials that can be used for water purification processes. Such a material that is stable in both acidic and basic conditions, with good adsorption properties and a high reusability factor, easy to synthesize, environmentally friendly, cost-effective, will be highly desirable [8].

In this project, we investigate the use of functionalized magnetite nanoparticles with mono-alkyl phosphate esters and their derivatives as adsorbents for the removal of organic contaminants from wastewater. The as-synthesized magnetite nanoparticles are functionalized with mono-alkyl phosphates to render affinity and selectivity towards nonpolar organic contaminants (dyes) in water.

1.2 Problem statement

Municipalities and industries are facing a huge problem of water contamination every day. Contaminants from industrial activities, such as mining, pharmaceutical

companies, and agricultural run-offs, as well as natural sources, such as heavy metals from ore deposits, enter water systems in different ways. These contaminants can be removed from water using different chemical processes and techniques. The currently used conventional techniques for water treatment usually include oxidation or chemical degradation processes using chlorination or ozonation (O_3), adsorption or biodegradation with the use of activated carbon, and advanced photooxidation using ultraviolet light or electrochemical processes. Still, these processes are not always sufficient for the removal of new emerging pollutants, pharmaceuticals, and personal care products [8,9]. Thus, over the last decades, disposed pharmaceuticals, bioactive organic compounds, and other similar pollutants have been slowly accumulating in the environment [10]. Many of these contaminants are present in very low concentrations in the environmental matrixes, and there are no regulations yet set regarding their acceptable concentration levels since they are still being developed [11–13].

Superparamagnetic iron oxide nanoparticles (SPION) are magnetite/hematite nanoparticles (NPs) prepared from cheap and affordable starting materials, i.e., iron salts, such as $FeCl_2$ and $FeCl_3$, using environmentally friendly techniques and solvents (green synthesis). Over the years, they have gained attention since they are easily prepared and of a benign nature [14,15]. The size of these nanoparticles can be tailored during synthesis; synthetic procedures for the preparation of NP of different sizes have been developed. SPION NPs have been tested in drug delivery systems, electromagnetism, magnetic hyperthermia, and enhancing magnetic resonance imaging (MRI), to name a few applications [16], and also as adsorbents for both organic and inorganic contaminants in the water purification process [17]. These NPs can easily be functionalized with organic (such as phosphate monoesters, etc.) and inorganic (silica, etc.) ligands to increase their affinity towards the contaminants of interest.

1.3 Justification

The currently used methods for water purification are not well suitable for the removal of multiple emerging pollutants, both organic and inorganic. Advanced adsorption techniques show promising removal capabilities; often they are effective enough to remove contaminants at trace (parts per billion) levels [18]. The commonly used adsorbents are activated carbon, chitosan, and carbon nanotubes. They have a greater affinity towards organic pollutants than inorganic pollutants, as they struggle to remove certain contaminants at trace levels to a safe drinking level [19].

However, these metal-based nano-adsorbents have a high sorption surface area, low preparation cost, and easy preparation procedures. They have the advantage of possible surface modification: their surfaces can be easily modified by various methods.

Most metal-based nano-adsorbents have hydroxyl groups on their surfaces that are formed during the synthesis and purification processes. These hydroxyl groups help to easily functionalize the adsorbent and form supramolecular assemblies with contaminants that have -NH, -COOH, and -OH functional groups through weak interactions, such as electrostatic attraction and hydrogen bonding [20–22]. The iron-oxide nano-adsorbents possess positively charged surfaces that attract negatively charged species. Research has been done on magnetite (Fe_3O_4) and maghemite (γ-Fe_2O_3) nanoparticles as possible metal-based nano-adsorbents for the development of wastewater treatment technologies from organic and inorganic water pollutants [3,8,17,18,22].

These NPs can easily be functionalized with different substances like graphite sheets, chitosan, calixarenes, phosphate esters, etc., to remove organic and inorganic pollutants. To bind organic modifiers to the NP surface, functionalizing them with phosphate esters is one of the possible methods [23]. Halik and colleagues reported successful pesticide (glyphosate) removal using SPION coated with phosphate mono-alkyl asters [14,15]. To our knowledge, no comprehensive study has been done on the removal of various pollutants from wastewater using iron oxide nanoparticles with mono-alkyl phosphate ester shells. The SPION NP shell consisting of the hydrophobic alkyl chain should increase its affinity towards binding hydrophobic organic molecules which will bind to coated NPs because of the hydrophobic effect [14,19].

1.4 Objectives of the study

This project was due to test the ability to functionalize SPION with long-chain alkyl phosphate monoesters and the capacity of such coated SPION to remove organic and inorganic (anionic) contaminants from contaminated water. The specific objectives of this project were as follows: -

(a) To synthesize and coat Fe_3O_4 nanoparticles with long alkyl chain phosphate monoesters.
(b) To characterize the as-synthesized nanoparticles, mono-alkyl phosphate esters and the coated nanoparticles with Fourier transformation infrared spectroscopy (FTIR), thermal gravimetric analysis (TGA), transmission electron microscope (TEM), scanning electron microscope (SEM), Energy dispersive spectroscopy (EDS), and nuclear magnetic resonance (NMR), and Powder X-ray diffraction (PXRD).
(c) To test the ability of the as-synthesized nanoparticles to remove pollutants of interest from polluted water, and their reusability factor. Experiments were performed with organic dyes and spectroscopic methods as well as with certain organic compounds using solvent extraction.

1.5 Outline of the dissertation

This dissertation outline gives a summary of the contents of this dissertation.

Chapter 1 (Introduction): In this chapter, the background of the project, justification for this project to be done, and objectives of this project are discussed.

Chapter 2 (Literature survey): The literature on Fe_3O_4 nanoparticles, phosphate mono-alkyl esters, and their properties and applications are reviewed.

Chapter 3 (Results and discussion): The results obtained and their interpretation including the characterization (of Fe_3O_4, Fe_3O_4@Phosphate ester, phosphate esters) results are discussed in this chapter.

Chapter 4 (Methodology): The experimental and analytical procedures used are described in this chapter.

Chapter 5 (Conclusions and Recommendations): Conclusions drawn from the interpretation of the obtained results in **Chapter 3**, also given the recommendations for what can be done to improve the obtained results are laid in this last chapter.

Chapter 2

Literature review

2.1 Nanotechnology

Nanotechnology is a rapidly developing field that specializes in nanoscale innovation and has a wide range of real-world applications. It deals with nanoparticles with at least one dimension between 1 and 100 nanometers [24–26]. Extensive research in the field of nanotechnology began in the 1980s and has continued to be a modern-day marvel of scientific discovery [27]. The use of nanotechnology in our everyday life has changed our societies into a new era [28]. It provides a wide range of possibilities for our everyday life, giving improvements in our gadgets and computers [29] and also providing marvellous new properties in areas such as food packaging, agriculture, environmental analysis, medicine, etc. [30]. These new properties (small particle size, large surface-to-volume ratios, magnetic, catalytic, etc.) provided by nanomaterials are promising to be utilized during wastewater treatment for the removal of both inorganic and organic contaminants, such as toxic metals, pharmaceuticals, pathogens, and dyes [31–33]. To date different metal-based nanoparticles such as zeolites, carbon-based nanomaterials (carbon nanotubes, graphene sheets, graphite oxide sheets, etc.), nanoscale metal oxides (iron oxides (Fe_2O_3/Fe_3O_4), zinc oxide (ZnO), aluminium oxide (Al_2O_3), titanium dioxide (TiO_2), etc.) have been synthesized and tested for water and wastewater treatment using techniques such as photocatalysis, adsorption, filtration, and electrosynthesis [34–37]. These nanomaterials show impressive results with a great affinity towards diverse functionalized organic and inorganic molecules [38]. The iron-based magnetic nanoparticles are receiving greater attention for water and wastewater treatment for the removal of contaminants because of their easy synthesis, environmental friendliness, cheaper cost, and iron being the second most abundant metal on Earth [39,40].

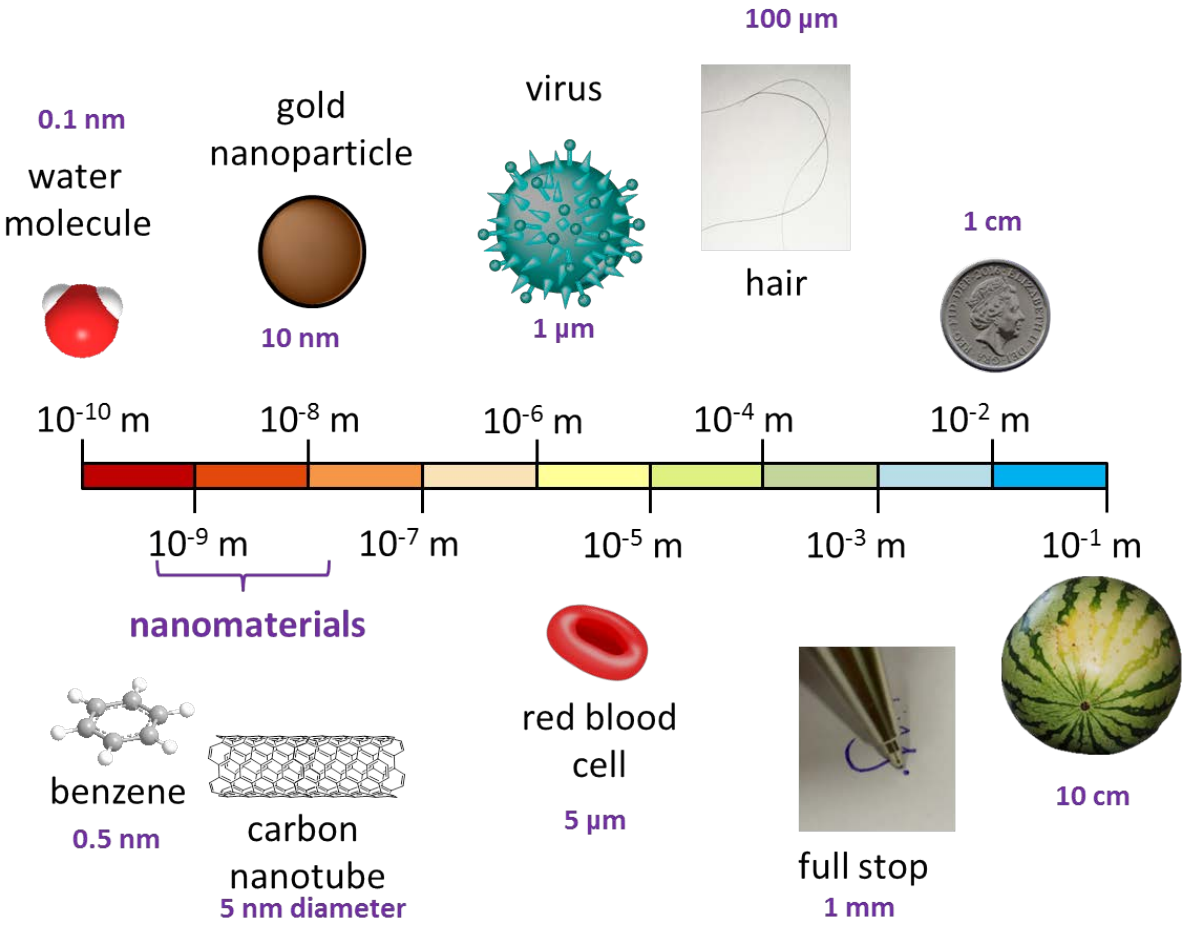

Figure 2.1: Size comparison of nanoparticles with molecules and bulk materials [41]. (Reprinted with permission from: El Sayed Zaki M. Nanotechnol and Adv in Med. 2011;6(5):89–117)

2.2 Classification of nanoparticles

Nanomaterials are materials with at least one dimension in the nano range, i.e., 100 nm or less. Materials with three, two, one, or zero dimensions confined in the nano range are called zero dimension (0D), one dimension (1-D), two-dimension (2-D), and three-dimension (3-D), respectively. Examples of 0D nanomaterials, all three dimensions in the nano range, are nanoparticles and quantum dots. 1D nanomaterials are materials with one dimension outside the nano range, examples are nanotubes, nanorods, nanowires, and nanofibers. 2D nanomaterials are nanomaterials with two dimensions outside the nano range, these materials resemble plate-like shapes, examples are graphene/ graphite sheets, nanofilms, and nanolayers. 3D materials are

materials with none of the dimensions confined in the nano range, examples are bulk powders, multilayers of graphite sheets, and bundles of nanotubes.

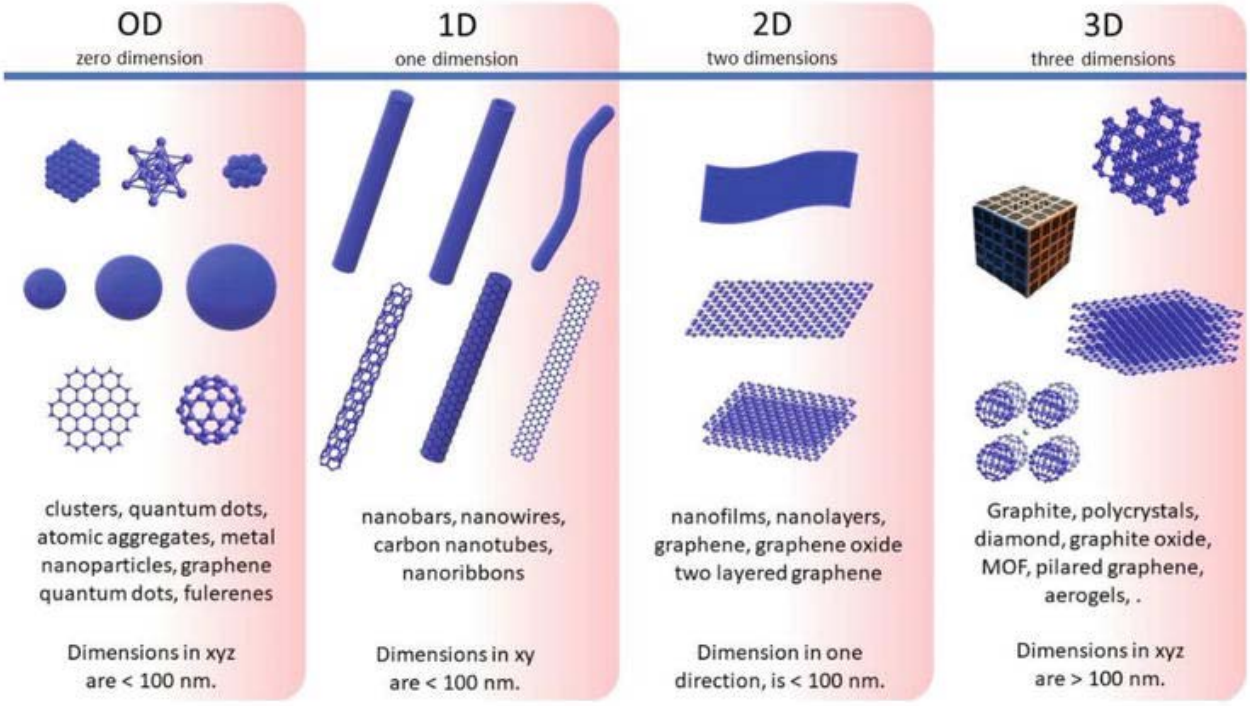

Figure 2.2: Classification of nanomaterials according to their dimensions [42]. (Reprinted with permission from Gaur M, Misra C, Yadav AB, Swaroop S, Maolmhuaidh F, Bechelany M, et al. Biomedical applications of carbon nanomaterials: Fullerenes, quantum dots, nanotubes, nanofibers, and graphene. Materials (Basel). 2021;14(20):5978)

2.3 Different methods used to synthesize magnetic iron oxide nanoparticles

Magnetic iron oxide nanoparticles with desired properties can be prepared using different methods, which can be classified into two major approaches: top-down and bottom-up. Bottom-up methods are common chemical and biological methods whereas top-down methods are physical techniques [43–45]. Chemical methods are the most used technique to synthesize magnetite nanoparticles: 90% of the commercially available magnetite nanoparticles are prepared using chemical methods, 8% by physical methods, and 2% by biological methods [46]. The coprecipitation method is the most used technique to synthesize magnetite nanoparticles because of its simple and effective procedure [47]. Chemical methods

are efficient, simple, allow easy control of the size of the particle, and shape, and have high yields hence they are preferred over the physical and biological methods [48]. Most physical methods suffer from the ability to get the particles in the nano range [49]. On the other hand, biological methods give good results but they use plant extracts which are rare and costly; these methods are also time-consuming [50].

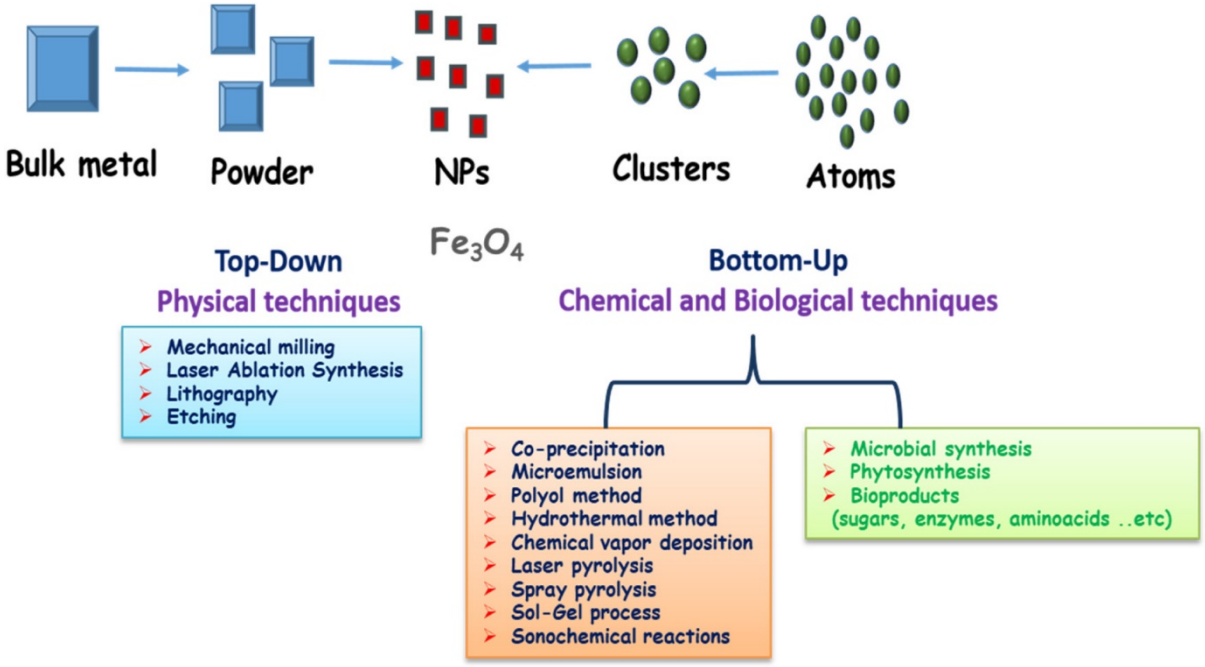

Figure 2.3: Different synthetic methods for preparations of nanoparticles [51]. (Reprinted with permission from Parveen K, Banse V, Ledwani L. Green synthesis of nanoparticles: Their advantages and disadvantages. AIP Conf Proc. 2016;1724(1):2564–965)

2.3.1 Chemical methods.

2.3.1.1 Co-precipitation method

The co-precipitation method is the most widely industrially used method for the synthesis of iron oxide (Fe_3O_4, γ-Fe_2O_3, α-Fe_2O_3, β-Fe_2O_3, etc) nanoparticles because of its efficiency, easiness, greenness, and overall mild conditions [52,53]. During the coprecipitation method, iron oxides are formed from the precipitation of Fe(II) and Fe(III) precursors in the solution in the presence of an alkali (base) acting as a precipitating agent in an inert environment [54]. Fe_3O_4 nanoparticles are prepared according to the chemical reaction:

$Fe^{2+} + 2Fe^{3+} + 8OH^{-} \rightarrow Fe_3O_4 + 4H_2O$

Factors such as the ratio of Fe(II) and Fe(III) in the solution, the temperature at which the reaction takes place, magnetic stirring rate, the rate at which the precipitating agent (alkali media) is added and its concentration, pH of the medium and the ionic strength of the solution affect the size, shape, and composition of the nanoparticles formed [55–57]. Once appropriate synthetic conditions are met, nanoparticles can be reproducible at a laboratory scale. These synthetic magnetite nanoparticles can decompose to maghemite (Fe_2O_3). Magnetite nanoparticles tend to oxidize to maghemite under oxidizing conditions. It is also noted that it is difficult to get monodispersed nanoparticles, hence it is important to optimize the above-mentioned factors [58]. Iron oxide nanoparticles are unstable and easily form aggregates, which is caused by the large surface-to-volume ratio [56]. To stabilize and avoid agglomeration of the nanoparticles, they can be coated with molecules such as carboxylates, polymers, surfactants [59], proteins [60], tetraethyl orthosilicate (TEOS), etc., These coatings also help to control the size, dispersion, and shape of the nanoparticles [61]. All these physicochemical properties of iron oxide obtained from the co-precipitation method make it the best method used to synthesize nanoparticles on a large scale.

Massart et al. prepared magnetic Fe_3O_4 nanoparticles by coprecipitating from $FeCl_2/FeCl_3$ solution in an alkaline medium [62]. They managed to prepare very small nanoparticles roughly with a spherical shape with an average diameter of 8 nm [62,63].

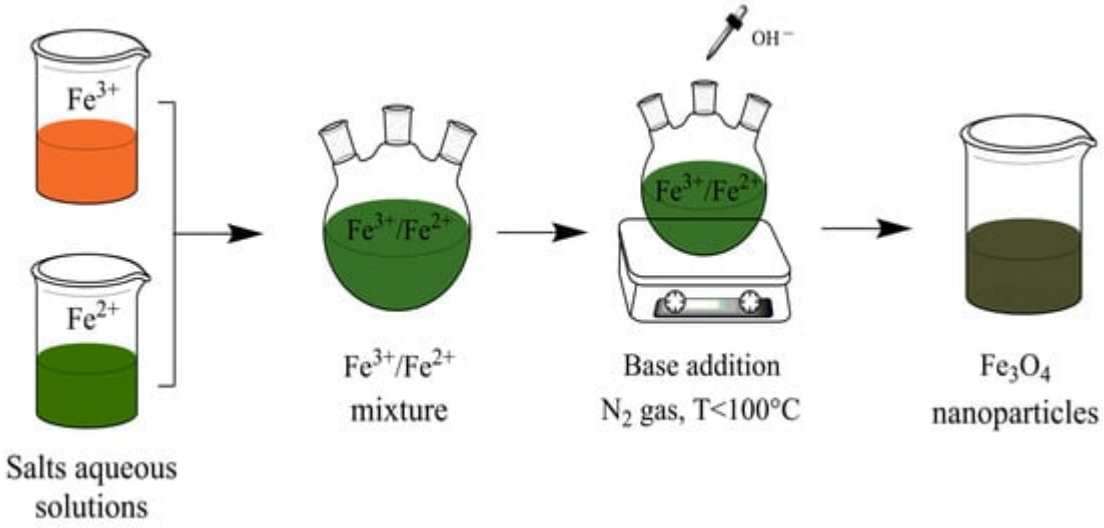

Figure 2.4: Schematic diagram for preparation of iron oxide nanoparticles [64]. (Reprinted with permission from Kumar NS, Kumar KV. Synthesis and Structural Properties of Bismuth Doped Cobalt Nanoferrites Prepared by Sol-Gel Combustion Method. World J Nano Sci Eng. 2015;05(04):140–51)

2.3.1.2 Hydrothermal route

The hydrothermal route which is also known as a solvothermal route or pyrolysis is also one of the most used chemical methods to synthesize nanoparticles and ultrafine powders [65]. This method was adapted by geologists in the 19th century when they studied certain minerals and rocks [66]. In the hydrothermal route nanoparticles and ultrafine powders are prepared via crystal growth in aqueous media at high temperatures (125–250 ^{o}C) and at high pressures of 0.3–4 MPa [67–69] inside reactors or autoclaves that can maintain these conditions [70,71]. Nanoparticles or ultrafine powders can be prepared using this method via three paths: hydrolysis and oxidation or neutralization of mixed oxides. These three paths are very similar in reaction conditions but with hydrolysis and oxidation, only ferrous salts are used as iron precursors [72]. This method used at 140 ^{o}C affords magnetite nanoparticles with 40 nm diameter or less and optimises the saturation magnetization to 85.8 emu.g^{-1} which is much lower than the saturation magnetization of the bulk iron oxide [73]. Hao and Teja investigated the effects of temperature, iron precursor type, and reaction time on morphology and particles size [43,44]: they concluded that the iron precursor concentration affects the particle size, an increase in concentration increases the

particles size whereas monodispersed particles were obtained at shorter reaction times [17]. Guo et al. also reported that the type and concentration of the iron precursors play a vital role in controlling the shape and size of the nanoparticles. They also added that reaction time does affect the size distribution, with a shorter reaction time they obtained a higher ratio of monodisperse particles [74]. Naghibi et al. studied the effect of the iron precursor concentration keeping other parameters constant and they concluded that an increase in the iron precursors concentration led to the formation of spherical particles with an average diameter of 15.6±4 nm [75].

One of the main disadvantages of the hydrothermal route is its slow kinetics, but to overcome this problem one can use microwaves to improve the rate of crystallization [73]. Another disadvantage to this technique is the requirement of costly pressure-resistant reactors at higher temperatures. This method is also energy-, material-, and time-consuming [76].

2.3.1.3 Microemulsion

The microemulsion method is the mixing of immiscible solvents (i.e., oil, water, and surfactant) forming a thermodynamically stable isotropic dispersion with the surfactant molecules forming an interfacial layer. The surfactant molecules have two domains, hydrophilic heads that are soluble in water and hydrophobic tails soluble in the oil phase. They form a monolayer on the interface between these two immiscible liquids decreasing the water-oil interface tension. The main role of the surfactant during the microemulsion synthesis method is to lower the interfacial tension between these two immiscible liquid phases [77,78]. Microemulsions can be subdivided into three groups which are direct emulsions (oil in water), reversed (water in oil), and bi-continuous emulsions. Metal oxide nanoparticles are produced by this method using the reverse microemulsion method with the aid of surfactants producing uniform-size nanoparticles. Different surfactants (anionic, cationic, and non-ionic) have been employed for the synthesis of metal nanoparticles [46,79]. Lopez Perez et al. proposed reverse microemulsion to synthesize iron oxide nanoparticles where they controlled the particle size by forming water droplets at the surface of the organic solvent [77]. When two mixtures of similar microemulsions of water-in-oil with precursors are mixed, they form microdroplets that experience collisions and break, forming a precipitate

inside the micelles. After completion of the formation of the precipitation process acetone or ethyl alcohol is used to extract the precipitate. This property of precipitate forming inside the micelles helps to obtain particles of uniform size and shape. Chin & Yaacob reported similar results when dissolving HTAB (hexadecyltrimethyl ammonium bromide) in n-octane followed by the addition of 1-butane to produce nanoparticles with a 5-10 nm radius [80]. The major drawbacks to this method are the low crystallinity and lower yields obtained [53,77,81].

2.3.1.4 Sol-gel method

The sol-gel technique is a wet chemical process that is used to synthesize nanostructured metal oxides by hydroxylation and condensation of precursor salts in solution forming a “sol” of nanometric particles [82]. This sol is then dried by removing the solvent or by use of a chemical reaction to obtain a 3-D metal oxide network. Hydrolysis can be performed using an acid or a base, but water is used as the solvent. From the literature, it is stated that the use of basic catalysts produces a colloidal gel whereas acidic catalysis produces a polymetric gel [46,83]. These reactions are performed without applying heat, heat is only needed to get the final crystalline particles [84].

Like other methods, the factors that affect the size, shape, kinetics, growth, etc, are temperature, time, pH, the concentration of the iron precursor, and agitation intensity [85,86]. This method is commonly used for the synthesis of maghemite nanoparticles as compared to magnetite nanoparticles because of its oxidative conditions tend to form Fe_2O_3 nanoparticles

A sol-gel reaction mechanism for the formation of magnetite particles from iron (III) precursors in solution is as follows:

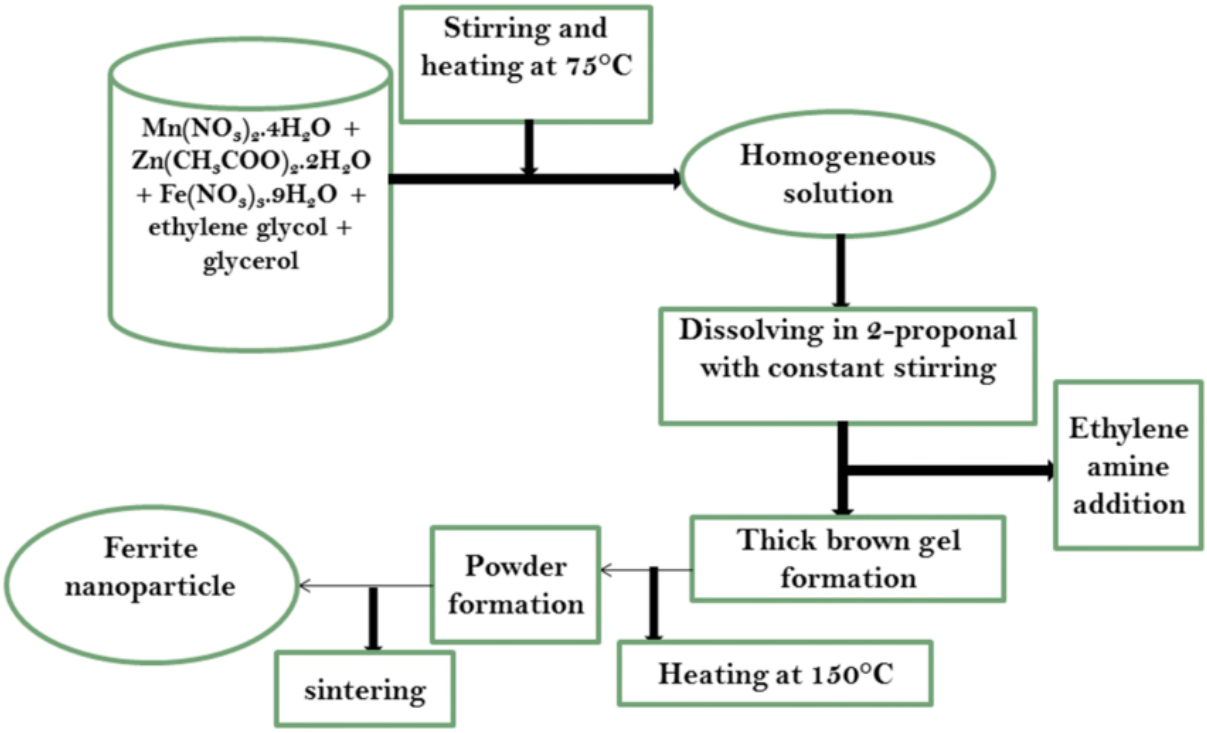

Figure 2.5: Sol-gel schematic diagram for the synthesis of ferrite nanoparticles [86]. (Reprinted with permission from Thakur P, Taneja S, Sindhu D, Lüders U, Sharma A, Ravelo B, et al. Manganese Zinc Ferrites : A Short Review on Synthesis and Characterization. J Supperconductivity Nov Magn. 2020;10(21):1023–40)

2.3.1.5 Thermal decomposition

Thermal decomposition also known as thermolysis, is a chemical method used to synthesize nanoparticles where organometallic compounds are decomposed. The temperature at which these organometallic compounds decompose is known as the thermal decomposition temperature. Since heat energy is used to break the chemical bonds between the atoms of organometallic compounds, this process is an endothermic process [87]. With this method, one can control the size, shape, and dispersion of the synthesized nanoparticles since the decomposition of the organometallic compounds take place in organic solvents with stabilizing surfactants acting as capping agents to control the size of the synthesized nanoparticles, under inert conditions [48,64]. The control over the nanoparticle size, shape, and morphology depends on the reaction conditions, such as reaction time, reaction temperature,

annealing temperature, type of organic solvent used, and the precursor-to-surfactant ratio [53]. This method is not environmentally friendly because of the toxic organic solvents such as chloroform, hexane, and iron pentacarbonyl as a common iron source. Another drawback to this method is the use of high temperatures, and nanoparticles prepared by this method easily oxidise to α-Fe_2O_3 and then to β-Fe_2O_3 when exposed to air [88,89].

2.3.2 Physical methods

2.3.2.1 Gas-phase deposition

Vapour phase deposition also known as gas-phase deposition or aerosol phase method includes two types of vapour deposition which are physical vapour deposition (PVD) and chemical vapour deposition (CVD) [90]. For the synthesis of iron oxide nanoparticles, using iron metal as raw material these methods give different products, i.e. PVD produces both thin films and composite (fine iron oxide) nanoparticles depending on the parameters set and CVD produces iron oxide thin films or nanotubes [91]. During gas phase deposition, the particles form by the supersaturation of the iron precursors, where the solute in the solution condenses and the solvent evaporates while the solution is sprayed in the presence of a reducing agent in an inert environment [92,93]. This method has the advantage of producing purer fine nanoparticles, reducing the risk of contamination, whereas it has a huge disadvantage of requiring high temperatures and difficulty in maintaining the uniform nanosize particles during the experiment [90]. The physicochemical properties of iron oxide nanoparticles synthesized by this method can be further tailored by adding extra processing steps [46,94].

2.3.2.2 Pulsed laser ablation

Pulsed laser ablation in a liquid phase is a promising synthetic method for the preparation of nanoparticles with a better ability to control the process parameters. During this method, a substrate (e.g. iron (III) acetylacetonate [Fe-$(acac)_3$]) is laser ablated producing a plasma plume at high temperatures and pressures leading to the formation of ionized species from the target, and reacts with the solvent to produce

metastable particles via nucleation and growth [95]. Several studies have been reported for the synthesis of iron oxide nanoparticles using this method with different organic solvents, such as ethanol [96], acetone [97], oleic acid, and oleylamine [98], affording NPs with sizes less than 20 nm. This method has the advantages of speed, simplicity, limited exposure to contamination of the synthesized nanoparticles, and lastly, almost no side products are being formed [99–101]. This method has drawbacks, including those inherent to the ablation process on large scale. For example, some species may attain high kinetic energies, causing re-sputtering, and the laser beam's inhomogeneous energy distribution may result in an inhomogeneous energy profile in the plume [102,103].

Experiments conducted by Amendola et al. suggest that the laser ablation method is not good for the synthesis of magnetic nanoparticles: the saturation magnetization value of the nanoparticles produced by this method was lower than the values compared to nanoparticles prepared using wet chemical methods [52,102,104].

2.4 Properties of nanomaterials

Nanomaterials have different structural characteristics than atoms and bulk materials. While the properties of bulk and microstructured materials are comparable, the properties of nanostructured materials are radically different from those of bulk materials. These distinctions are mostly attributable to the materials' nanometer size, as such (i) high percentage of surface atoms, (ii) high surface energy, (iii) spatial confinement, and (iv) reduced defects. Nanomaterials have extraordinarily large surface-to-volume ratios due to their tiny dimensions, which emphasize more surface-dependent material characteristics and a wider area for atom-to-atom interactions. Nanomaterials typically have improved/advanced characteristics in comparison to their bulk counterparts when their sizes are comparable to their lengths. For instance, metallic nanoparticles, which are particularly potent catalysts, are employed in the majority of catalysis plants. Chemical sensors with nanoparticle components are more sensitive and selective. The quantum effects are brought about by the spatial confinement effect of nanomaterials [51].

In bulk materials, electron transition from the valence band to the conduction band is difficult due to larger energy band gaps. Numerous bulk adjustments like reducing the

size of the material improves the energy band structure and charge carrier density of the nanomaterials, leading to better electrical and optical characteristics. Lasers and light-emitting diodes (LED) made from quantum dots and quantum wires have a bright future in optoelectronics. Due to their increased surface area, quantum dots are used as high-density information storage in electronics (like computers, etc). Contaminants in nanostructures and nanomaterials tend to move toward the surface because of heat annealing, favouring a self-purification process. The degree of perfection of nanoparticles affects their characteristics [105].

2.4.1 Magnetic properties

When reduced to their nanoscale level, some bulk materials that are not magnetic become magnetic. Gold and platinum are not magnetic in their natural state, but when they are shaved down to the nanoscale, they become magnetic. The surface atoms on the gold and platinum nanoparticles, which are about 10 nm, differ from those in the bulk materials and can be altered by capping the nanoparticles. By covering the nanoparticles with the certain chemical species, this phenomenon of capping the nanoparticles open the option of changing their physical characteristics. When manufactured in the nano range, most non-ferromagnetic bulk materials behave in a manner resembling ferromagnetism. Some nanoparticles can only exhibit ferromagnetic behaviour when they are coated with the proper molecules, for example, in gold nanoparticles the charge on their surface causes the behaviour to resemble ferromagnetism [27,104]. Iron oxide nanoparticles are only magnetic when there is an external magnetic field in their vicinity and become unmagnetized under the absence of an external magnetic field, with no net dipole. This phenomenon has been observed on the vibrating-sample magnetometry (VSM) graph that has no hysteresis curve meaning that it does not have retention i.e., “magnetic substance’s ability to retain magnetic power”. This type of magnetism is called superparamagnetism and is widely explored the biological applications for drug delivery systems: it easily reacts to strong magnetic fields [52]. At room temperature, magnetite nanoparticles are ferrimagnetic with a Curie temperature of 85 K. Magnetite nanoparticles with a radius smaller than 20 nm are superparamagnetic at room temperature, but their properties are mostly dependent on the synthetic method used, which also affects the size and shape of the

particles. On the other hand, maghemite nanoparticles are unstable at high temperatures and lose their susceptibility over time [106].

2.4.2 Optical properties

The optical characteristics of nanoparticles are among the most researched and practically usable features. The optical properties of nanomaterials are influenced by their shape, size, surface features, coating molecules, and other factors. Some nanomaterials absorb and emit light at various wavelengths because they have distinct colours at different sizes. Similarly, to this, the shape of the nanomaterial can have a significant impact on the characteristics of metal nanostructures. For instance, changing the size and shape of CdSe semiconductor nanoparticles affects their characteristics. Additionally, as seen from the Au nanoparticles in the picture below, when these metal nanoparticles are enlarged and their forms alter, their optical properties also drastically change [27,107,108].

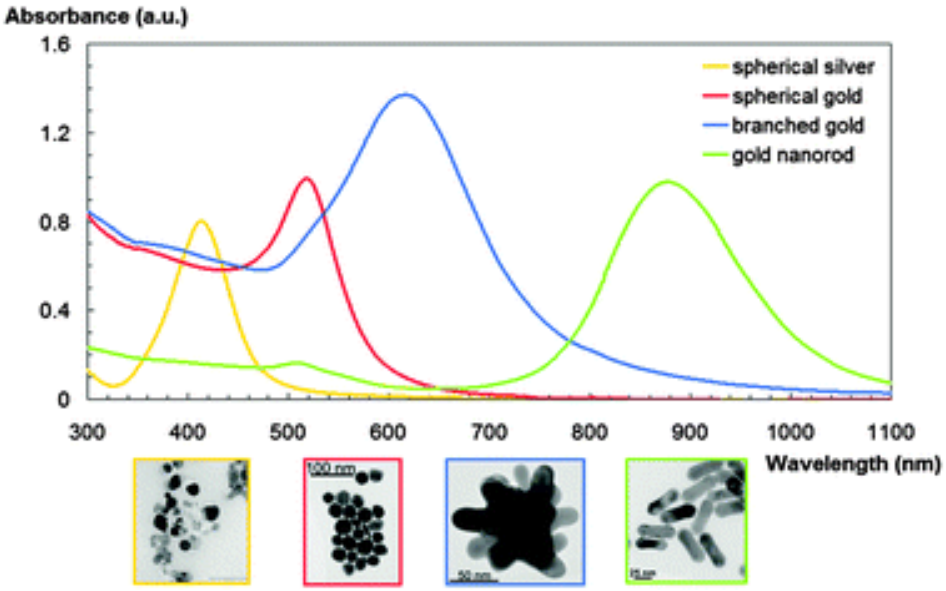

Figure 2.6 (a): Properties of Gold nanoparticles with different shapes [109]. (Reprinted with permission from Samrot AV, Sahithya CS, Selvarani AJ, Purayil SK, Ponnaiah P. A review on synthesis, characterization and potential biological applications of superparamagnetic iron oxide nanoparticles. Curr Res Green Sustain Chem. 2021;4(20):1000–42)

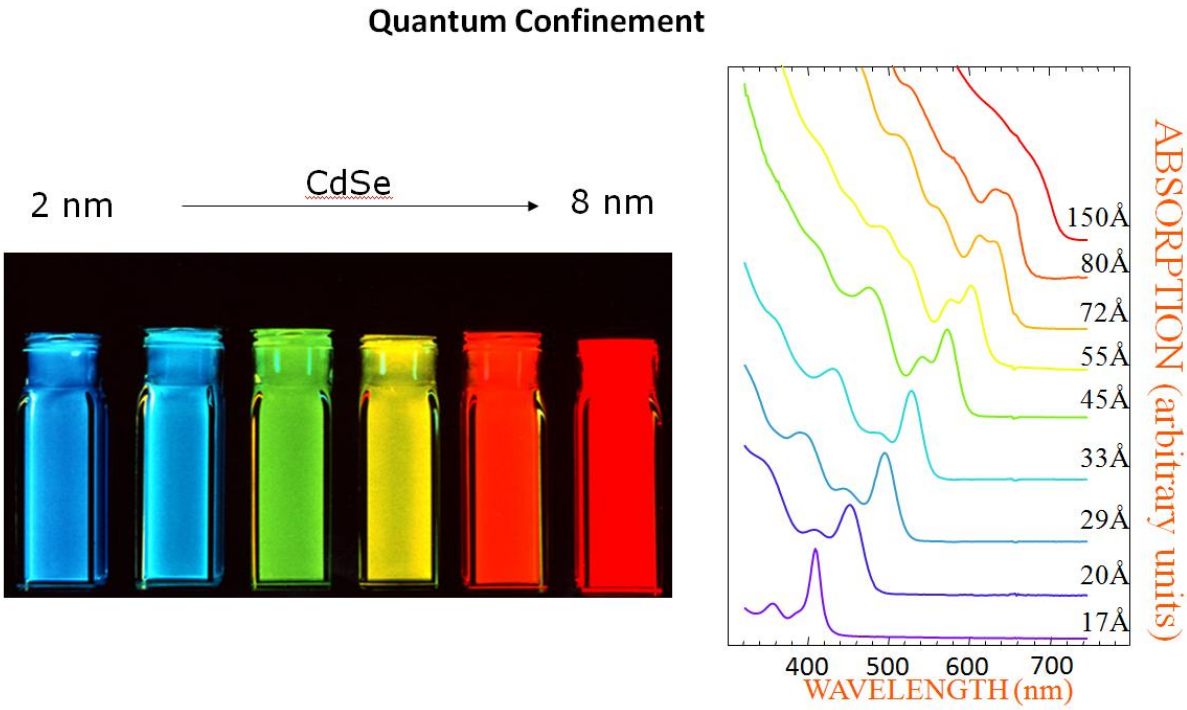

Figure 2.6 (b): Properties of CdSe nanoparticles differing in size [177].

2.4.3 Electrical properties

The mechanical thinning of nanowires and the measurement of the electrical current that flows through a specific point at a constant applied voltage are two techniques that can be used to discuss the electrical conductivity of nanomaterials. This method is typically used with nanotubes and nanowires. There are fewer electrons contributing to the electrical conductivity as the diameter of the nanowire is reduced. Characteristics like diameter cross-sectional area, or twist in the conducting wire have little influence on the conductivity of bulk materials. However, it has been discovered that the absolute conductivity of some nanomaterials, such as carbon nanotubes, depends on the area of the cross-section and also on the shear force applied to them. The conductivity of a multi-walled carbon nanotube is found to be different from that of a single-walled nanotube of the same size. Graphite is a good conductor of electricity; however, carbon nanotubes can be either a conductor or a semiconductor, or an insulator. One electron wave node in a carbon nanotube that conducts electricity serves as a current transporter. The band gap energy (Eg), or the energy difference between the valence band and the conduction band, separates these three types. Whether a substance is a conductor, a semiconductor, or an insulator is determined

by the ability of electrons to move from the valence band to the conduction band. Because the valence band and the conducting band of conducting materials, such as metals, overlap and have very low values of Eg, thermal energy alone can stimulate electrons to move from the valence band to the conducting band in these materials. To stimulate electrons from the valence band to the conducting band in semiconducting materials, a little amount of electron voltage that must be greater than the band gap energy (Eg) is required, leaving electron-hole pairs on the valence band known as excitons. Insulators do not conduct electricity because of their large band gaps, which require high voltages to pass through the threshold [27,108].

2.4.4 Thermal properties

Nanosystems have different thermodynamics compared to those of macroscopic systems because they have a larger number of particles approaching infinity. Antoniammal and Arivuoli reported that an increase in the nanoparticle radius increases their melting point to higher temperatures. They also added that nanoparticles with small radii have higher surface energy, and increased amplitude of atomic vibrations, resulting in the surface growth of thermal vibration energy [106]. Singh and colleagues also reported that the larger the particle size the smaller/lower the specific heat, and the larger the melting entropy and enthalpy particle size increases [110].

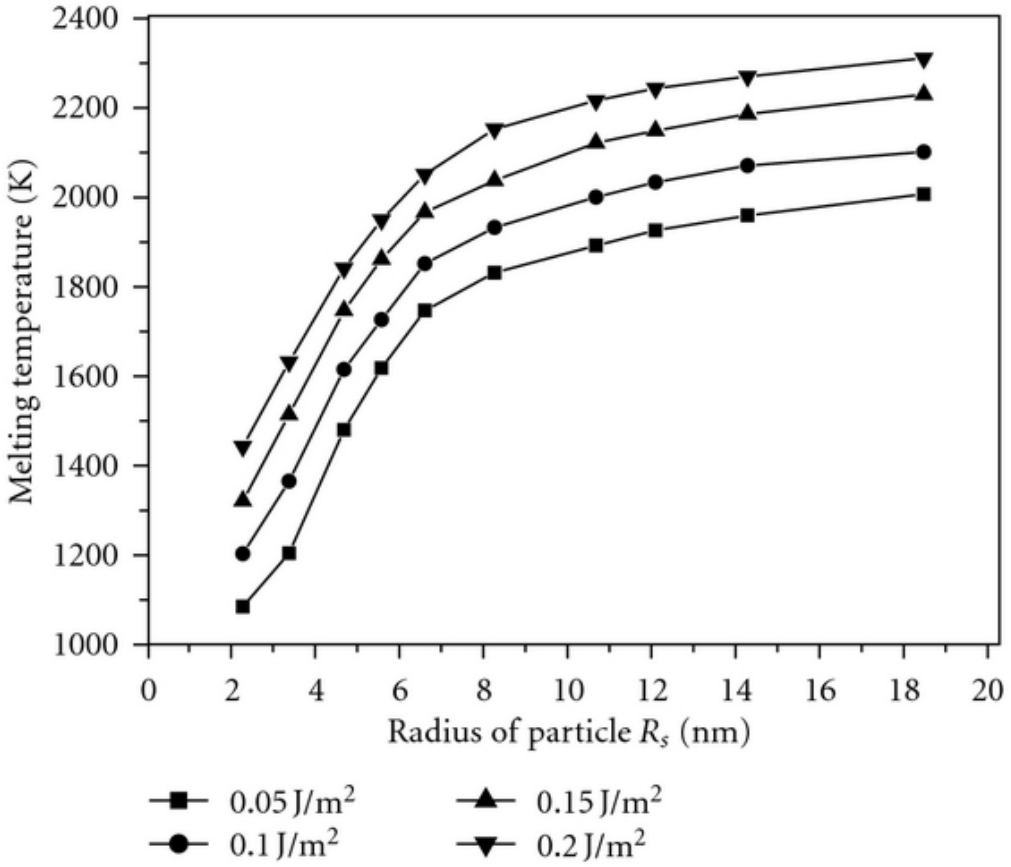

Figure 2.7: Size and shape dependence on melting temperature of Gallium Nitride nanoparticles [106]. (Reprinted with permission from Zysler RD, Fiorani D, Testa AM. Investigation of magnetic properties of interacting Fe_2O_3 nanoparticles. J Magn Magn Mater. 2001;224(1):5–11)

Due to their remarkable thermal properties; nanofluids, another type of nanomaterial, have attracted attention recently [107]. Nanofluids are composite materials made of solid and liquid particles suspended at the nanoscale. Depending on the intended use, a variety of nanofluids have been synthesized using nanoparticles of oxides, nitrides, metals, metal carbides, and nanofibers suspended in various base liquids, including water, ethylene glycol, and oils [108]. Han researched the impact of nanoparticles in liquids and came to the conclusion that nanofluids improve thermal conductivity compared to liquids without nanomaterials. They also promoted the utilization of nanofluids in medical equipment for both diagnosis and treatment [109].

2.5 Applications of Fe_3O_4 nanoparticles

Due to the favourable combination of their properties, magnetic Fe_3O_4 nanoparticles may find use in a variety of applications. Their possible use in the water treatment process will be discussed below (see "**2.8. Different methods used for water treatment**"). In this session, we will discuss several other perspective applications of magnetite nanoparticles.

2.5.1 Imaging

Magnetic iron oxide nanoparticle's application has been explored in the field of diagnostics as Magnetic Resonance Imaging (MRI) nanoparticles. SPIONs are used because of their less toxicity and superparamagnetic effect. For MRI applications SPIONs of sizes less than 5 nm are used because they can easily penetrate organs in the body [111]. When SPIONs are administered for therapy, they can be used to get images of damaged organs. Lee et al show the use of SPIONs in X-Ray imaging. This application of SPIONs is still a new imaging technique that is used for imaging cancer cells, neuroimaging ,and inflammation imaging [111].

Magnetic iron oxide nanoparticles have been widely explored in the medical sciences field, where it has been applied in tissue engineering, for repairing damaged tissues where protein-coated nanoparticles are placed in between the damaged tissues and increased in temperature join the two adjacent damaged tissues. They have been used in cancer therapy, magnetic hyperthermia, and in vitro bioseparation, i.e. where they show a better separation of biomolecules like DNA, protein, and antibodies [3].

2.5.2 Targeted drug delivery

Drugs are traditionally introduced to our bodies intravenously or orally. When a medication is injected into our bodies, it enters the systemic circulation and is lost before it reaches the intended target. The drug's bioavailability is decreased as a result of this procedure [112]. Nevertheless, recent studies have demonstrated that magnetic iron oxide nanoparticles are effective drug carriers when coated with appropriate compounds that inhibit oxidation and can sustain the drug molecules. When these

magnetic nanoparticles are used an external magnet is used to direct/concentrate the magnetic drug-loaded nanoparticles to the specific target site [112]. Additionally, by restricting the reticuloendothelial system's (RES) entry, the in-vivo retention period within the circulatory system is increased [102]. These SPIONs can easily cross biological barriers due to their small size [113]. Utilizing biocompatible and biodegradable coatings, such as biopolymers, improves their bioavailability and keeps them from agglomeration [114], what is very important, because it is difficult for NPs to cross biological barriers when they form agglomerates. Compared to conventional procedures (when a medicine is administered as a bare drug), the coated magnetic iron oxide nanoparticles demonstrate better results in the delivery of drugs to the precise places within the body [115].

2.6 Adsorption process

Removal of impurities during water purification is to the large extent based on the process of adsorption. Therefore, a detailed understanding of the process of adsorption is of paramount importance for the development of effective water treatment techniques.

The adsorption process includes an adsorbent and adsorbate. An adsorbent is a material that is used to treat/adsorb the adsorbate (in water treatment: the contaminant/pollutant). The adsorbent comes in contact with the adsorbate solution/suspension and the adsorption process takes place till the adsorbent is saturated, i.e., till it reaches a point where it can no longer adsorb the adsorbate, we call this the state of equilibrium. The concentration of the adsorbate that remained after the adsorption process can also be determined and the concentration of the pollutant adsorbed (qe) can be determined. The estimation of the amount of pollutant adsorbed is often performed with the use of adsorption isotherm models. The most commonly used isotherm models in water treatment studies are Langmuir and Freundlich isotherms.

2.6.1 Langmuir isotherm

According to the Langmuir adsorption isotherm, the adsorbate forms monolayer adsorption on the surface of the adsorbent and the adsorption process only occurs at certain spots on the adsorbent. According to this hypothesis, once a molecule adsorbs at a certain location on the adsorbent, no other molecules can do the same. Additionally, it is believed that the adsorptive sites' binding energies are equal and that there are no interactions between the molecules or atoms that have been adsorbed. The following mathematical statement can be used to illustrate the Langmuir equation's linear version.:

$$C_e/q_e = 1/q_{max}b + C_e/q_{max} \qquad \text{(eq. 2.1)}$$

Where q_{max} is the Langmuir constant linked to the maximum monolayer adsorption capacity and b is the Langmuir constant related to the energy of adsorption, C_e is the equilibrium concentration (mg/l), q_e is the quantity adsorbed per specific amount of the adsorbent (mg/g) in equilibrium. If the data fit the Langmuir isotherm, a straight-line

graph can be produced from a plot of C_e/q_e against C_e. From this plot, one can determine the maximum monolayer adsorption capacity (q_{max}) from the graph's slope, which has a slope equal to $1/q_{max}$, and one can determine the Langmuir energy adsorption from the intercepts, which has an intercept equal to $1/q_{max}b$ [116]. An example of a Langmuir isotherm plot is shown below:

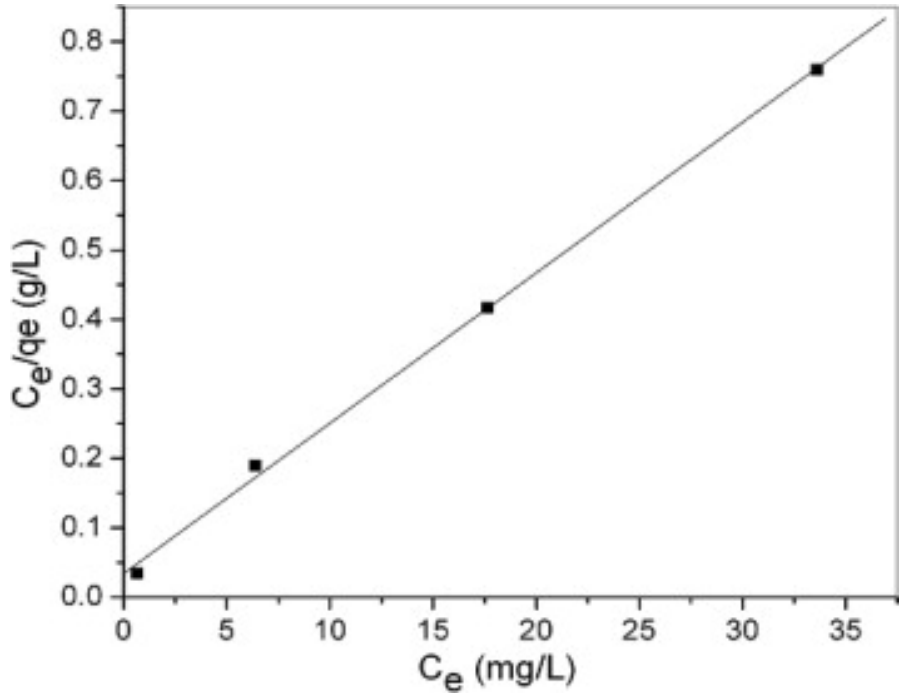

Figure 2.8: Langmuir isotherm plot for adsorption of Pb on DMSA@Fe_3O_4 DMSA-Dimercaptosuccinic acid [116]. (Reprinted with permission from Venkateswarlu S, Kumar BN, Prathima B, SubbaRao Y, Jyothi NVV. A novel green synthesis of Fe_3O_4 magnetic nanorods using Punica Granatum rind extract and its application for removal of Pb(II) from aqueous environment. Arab J Chem. 2019;12(4):588–96)

2.6.2 Freundlich isotherm

The Freundlich isotherm describes adsorption processes where there is multilayer sorption and adsorption on heterogeneous surfaces. The Freundlich isotherm can be described using the following mathematical equation:

$$q_e = K_f C_e^{1/n} \quad \text{(eq. 2.2)}$$

Its linear form, from **eq. 2.2,** can be written as:

$$\text{Log } q_e = \log K_f + 1/n \log C_e \quad \text{(eq. 2.3)}$$

Where C_e is the equilibrium concentration (mg/l), q_e is the equilibrium adsorbed amount of the adsorbate per amount of the adsorbent (mg/g) in equilibrium, and K_f and n are the adsorption capacity and strength of binding energy (intensity) respectively.

A linear graph of log q_e against log C_e from the linearized form of Freundlich isotherm gives a slope equal to 1/n and intercepts equal to log K_f. The graph below is an example of the Freundlich isotherm.

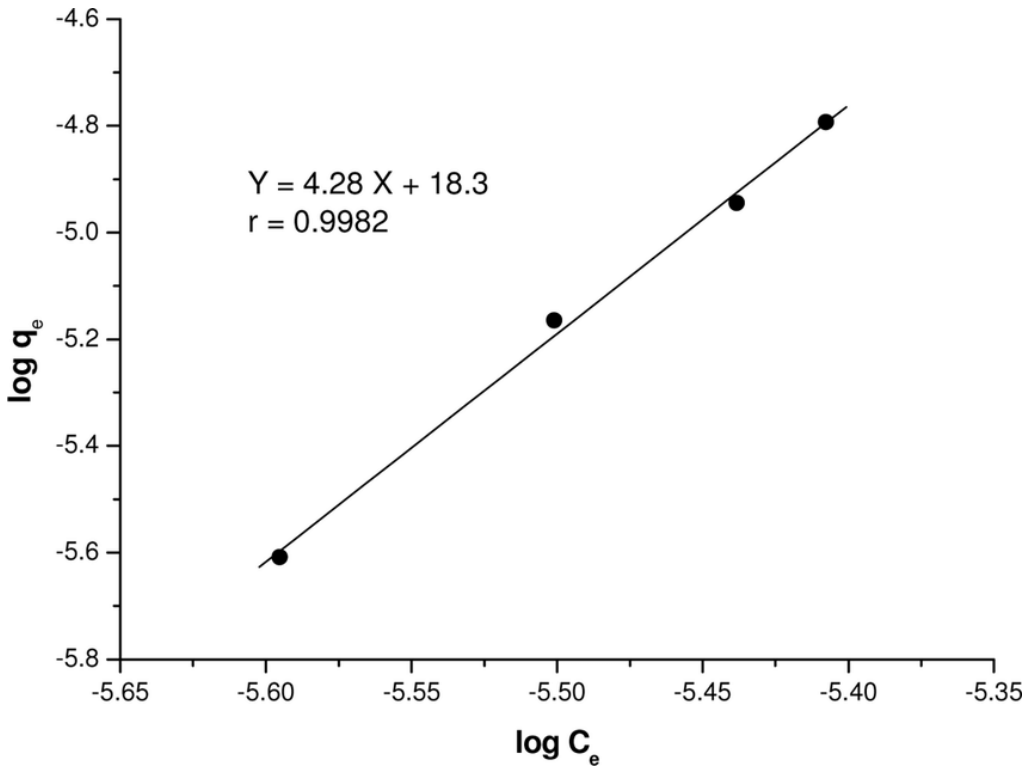

Figure 2.9: Linearized plot of Freundlich isotherm for adsorption of rhodamine B on polyurethane foam [117]. (Reprinted with permission from Baldez EE, Robaina NF, Cassella RJ. Study of rhodamine b retention by polyurethane foam from aqueous medium in presence of sodium dodecylsulfate. Sep Sci Technol. 2009;44(13):3128–49)

From the literature, it is known that many studies show complex behaviour towards adsorption experiments where it is difficult to conclude whether the data conforms with Langmuir or Freundlich isotherm models. To solve this problem many other adsorption isotherms have been developed. But for this project only these two isotherms were used since they are commonly used in water treatment studies.

2.7 Conventional water treatment process

The traditional water treatment plants fail when it comes to removal of viruses, bacteria and many pharmaceutical contaminants are not removed during the treatment processes or pass through at trace level concentrations [3]. Processes including flocculation, sedimentation, filtration, and chlorine disinfection are blended in traditional water treatment facilities. Before, untreated water enters a typical wastewater treatment facility, it is moved slowly through basins so that heavy debris can sink to the bottom before the facility is reached. The microscopic particles in the water are subsequently combined into larger aggregates with the use of chemical coagulants such as aluminium sulphate, ferric sulphate, ferric chloride, etc, and the larger aggregates settle away. After that, the water is softly transported through the flocculation basins where it flows over, submerged paddles to combine smaller particles into larger ones known as flocculation. The pure water flows through the filters as the floc descends to the bottom of the sedimentation basin. The filtering process gets rid of any leftover particles. Sand, granular activated carbon, and other materials are used as the filtration media. After the water has been filtered through the media, a predetermined amount of chlorine is applied as a disinfectant for a predetermined period of time. Clearwell stores the water after purification before it is distributed to the community [3,111].

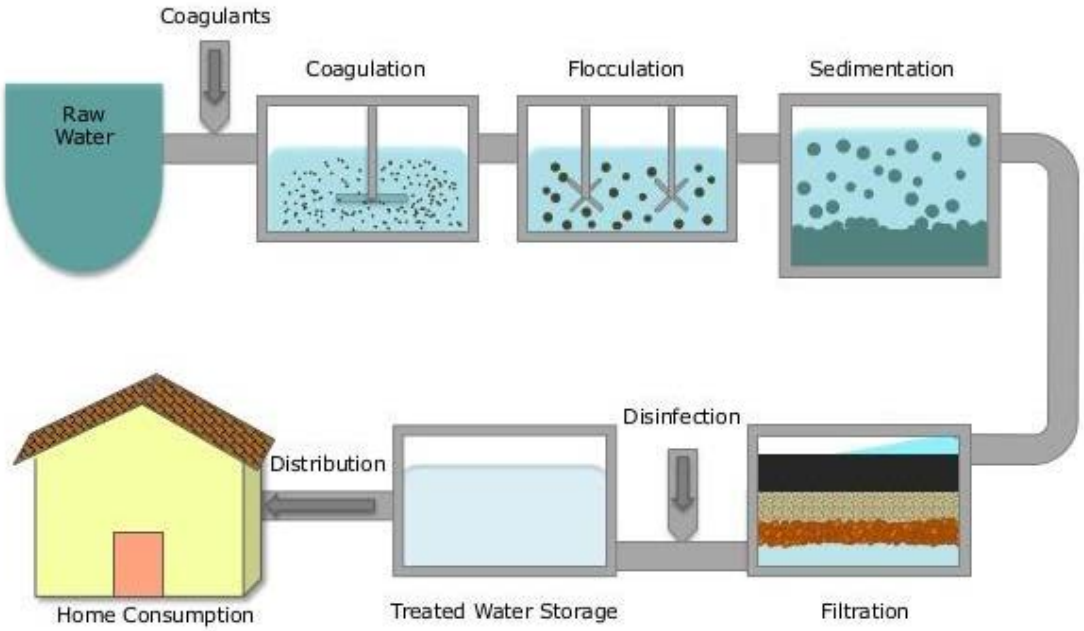

Figure 2.10: A conventional water treatment process [178].

2.8 Different methods used for water treatment

To date, there are many different available techniques used for water and wastewater treatment. The most common techniques are adsorption, membrane separation, reverse osmosis, ion exchange, and filtration. Some of these methods are employed for both removals of organic and inorganic contaminants, some only work best for either of the two. Adsorption techniques show great potential for removing both organic and inorganic contaminants when materials with a better affinity towards the contaminants of interest are used. Studies have been performed where adsorbing materials of chitosan, activated carbon materials, carbon nanotubes, cyclodextrins, and other polymers have been tested for their efficiency towards the removal of both organic and inorganic (heavy metals) contaminants [27].

2.8.1 Adsorption-based techniques

Adsorption is a process whereby ions, atoms, or molecules bind on the surface of a solid material. The species present on the surface of the adsorbent and those involved in bonding on the adsorbate determine the sort of bonding that occurs between the two. Adsorption can occur by either of the two processes, physical adsorption (physisorption) or chemical adsorption (chemisorption). Chemisorption only occurs in systems where there is chemical bonding and is mostly an irreversible process, whereas physical sorption occurs in adsorbate-adsorbent systems under ideal pressure and temperature circumstances, this process is reversible. While chemisorption predominates in processes involving core-shell nanoparticles, physisorption is frequently seen in large surface areas and porous materials like zeolites and activated carbon. A large number of nano-adsorbent materials have been reported in the literature, such as carbon-based, metal-based, polymer-based nano-adsorbents, and zeolites [27].

2.8.2 Carbon-based nano-adsorbents

Carbonaceous nano-adsorbents have a huge potential in water purification because of their advantageous physicochemical properties, nontoxicity, and low preparatory cost. Within the spectrum of carbonaceous nano-adsorbents, there are carbon

quantum dots and fullerenes which are 0D, carbon nanotubes falling under the 1D nanomaterials. Graphene, which is 2D, possess a planar structure suitable for surface chemistry and the adsorption of contaminants. Also, 3D materials like amorphous carbon or porous carbon possess good adsorption capabilities. The porous materials exhibit a larger surface area for the adsorption of both organic and inorganic pollutants found in water.

Numerous studies have been published on the use of fullerenes, graphene, carbon nanotubes (CNTs), and surface-functionalized activated carbon materials for the removal of heavy metals like chromium, lead, and arsenic as well as various organic pollutants like dyes [118]. The hollow and multi-layered structure of carbon nanotubes provides them with high adsorption efficiency and high surface area. However, these properties can further be improved by surface functionalization of the CNTs with strong oxidizing agents like HNO_3, and H_2SO_4, $KMnO_4$ which will lead to a surface densely modified with -COOH, -OH, and -C=O groups. Using these surface functionalized groups, heavy metals can easily bind on the surface via electrostatic bonding [119]. Fullerenes have been mostly used for the removal of hydrophobic organic compounds. Graphene and its composites have been reported in excellent work for the photodegradation of dyes [75,110].

2.8.3 Metal-based nano-adsorbents

Commonly used metal-based nano-adsorbents are iron oxide, titanium dioxide, and aluminium oxide nanoparticles. Uncoated forms of these metal oxide nanoparticles are good adsorbents for the removal of heavy metals and radionuclides. The sorption in these low-cost metal oxide adsorbents is based on the complexation between dissolved heavy metals and the oxygen of the adsorbent (metal oxides). In literature, it is stated that these adsorbents have higher adsorption capacity and faster kinetics because they have shorter intraparticle diffusion distances and more reactive surfaces (because of the relatively high presence of corners, edges, vacancies, etc) [120]. Yean et al. reported in their studies that as the nano-magnetite size decreased from 300 nm to 11 nm they achieved an adsorption capacity of arsenic of more than 100 times higher, these results were attributed to the increased surface area of the magnetite nanoparticles [121]. Metal-based nano-adsorbents have been explored to remove

heavy metals such as chromium, arsenic, mercury, etc, and they often outperform activated carbon.

As the size of the magnetite nanoparticles decreases to a critical value (~30 nm) the nanoparticles become superparamagnetic, losing permanent magnetic moments but responding to an external magnetic field making it easy to remove them from an aqueous media using a low gradient magnetic field. These effective low-cost nano-adsorbents can be used uncoated for the removal of inorganic contaminants, and they can also be coated with inorganic or organic molecules targeting the contaminants of interest. The organic coating can be performed using organic molecules such as calixarenes, chitosan, and dendrimers. In core-shell nanoparticles, the core serves as the magnetic site that responds to the external magnetic field while the shell provides affinity toward the target contaminants [122].

2.8.4 Membranes and membrane process

Depending on their size, membranes act as barriers that let liquids through while obstructing the passage of undesirable substances. Many diverse membrane types, including thin film nanocomposite (TFN) membranes, nanocomposite membranes, nanofiber membranes, and forward and reverse osmosis membranes, are used to purify water [123]. All these membrane types offer various benefits as well as have certain drawbacks in comparison to other materials. The significant energy consumption to induce the high pressure required during the purification process is one of the main disadvantages of adopting membrane technology in water treatment. Additionally, membrane fouling restricts the use of membrane processes because of the relatively short membrane lifespan and reduced their capacity for reuse. The disadvantage of high energy consumption is exacerbated by the complexity of the process design and operation of these membranes. The benefit of these membranes is that depending on the material type used, different functional nanomaterials can be incorporated into the membrane to improve properties like permeability, fouling resistance, mechanical stability, and thermal stability. Additionally, depending on the type of functional groups present on the membrane, some contaminants can not only be isolated, but also degraded [31].

2.8.5 Photocatalysis

In the process of treating water using photocatalysis, ultraviolet light is used to break down (degrade) pollutants in the presence of a substance (sensibilisator). Through this method, trace pollutants, like the species responsible for the microbiological infections, are removed. To increase the removal of hazardous and non-biodegradable pollutants, industries use this method as a pre-treatment step. The slow kinetics, high energy consumption, and high maintenance requirements of the light source are the key downsides of this approach. The benefit of photocatalytic materials is that they can be optimized in terms of size and form to increase their photoactivity. This method has great potential for addressing the issue of clean water scarcity; it is an environmentally friendly and sustainable water treatment technology. However, its large-scale application is limited by several factors, including: i) catalyst optimization to increase quantum yield or use visible light; ii) an effective photocatalytic reactor design and catalyst recovery/removal techniques; and iii) improved reaction selectivity [31].

2.9 Synthesis of phosphate esters.

Phosphate esters are organic molecules containing phosphoric acid residue. In industrial processes mono-alkyl phosphate esters are used as flame retardants, lubricants, surfactants, and corrosion inhibitors [124]. Phosphate esters are prepared from alcohols in the presence of a phosphorylating agent such as P_2O_5, $POCl_3$, and H_3PO_4 [125]. Products of phosphate esters are often formed as mixtures of mono-, di-, and tri-esters and sometimes even with unreacted alcohols. However, monoesters can be selectively formed by adding a phosphorylating agent in excess [111,126]. Phosphate esters can also be formed from activation using a base such as triethylamine (NEt_3) because the nucleophilic attack on $POCl_3$ by the alcohol is slow in the absence of a base. This method is commonly used for the formation of long-chain alkyl phosphate esters. This method takes advantage of NEt_3 being able to act as a nucleophile and a base so that it can easily react with $POCl_3$. The formed positively charged intermediate (as shown in **Figure 11**) is more reactive than the $POCl_3$, which makes it easier to be attacked by the hydroxyl group of the alcohol [124].

The disadvantage of this method is the need to remove the protonated amine residue after the reaction.

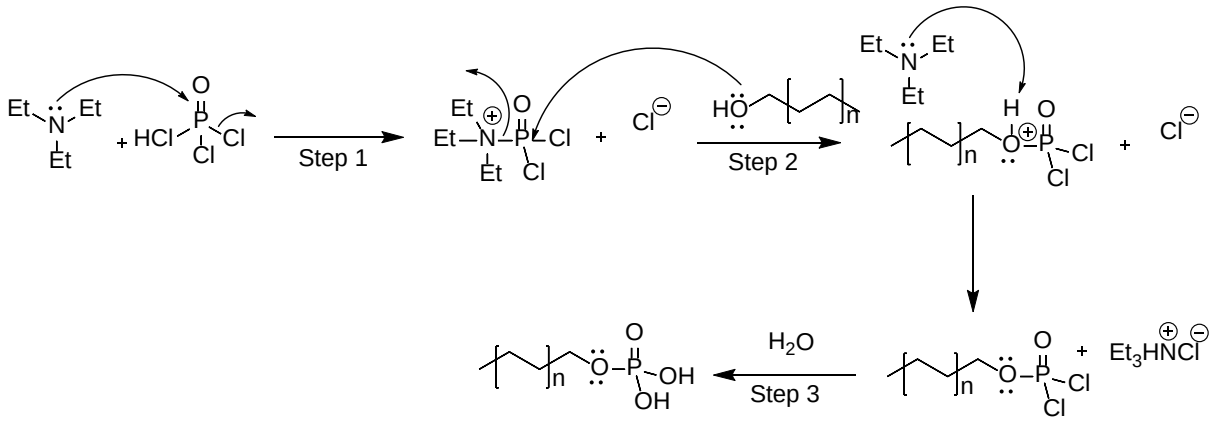

Figure 2.11: Mechanism for the formation of mono-alkyl phosphate esters using $POCl_3$ and triethylamine with n = 3,5,7.

In this project, long chain mono-alkyl phosphates are used as hydrophobic shells for magnetite nanoparticles. Mono-alkyl phosphates were prepared using phosphorus oxychloride as a phosphorylating agent. The relatively low reactivity of phosphorus oxychloride favours the formation of monoesters, and the whole process involves two reaction steps (**Figure 12**). The first step is the formation of the intermediate: phosphorodichloridate formed by the nucleophilic attack of the alcohol at the phosphorus atom of $POCl_3$. The second step is the hydrolysis of the intermediate formed in Step 1 to form the mono-alkyl phosphate ester.

These hydrophobic shells render better affinity towards non-polar organic pollutants (such as organic dyes and pharmaceuticals) from the aqueous media. Their easy synthetic and environmentally friendly methods make them to be better preferred for removal of non-polar contaminants from wastewater compared to other organic shells such as calixarenes, graphene, etc. Whereas the non-coated magnetite nanoparticles suffers from removal of non-polar organic contaminants since their surfaces are positively charged and bind best negatively charged molecules like the mono-alkyl phosphate esters via the phosphoric acid functional group.

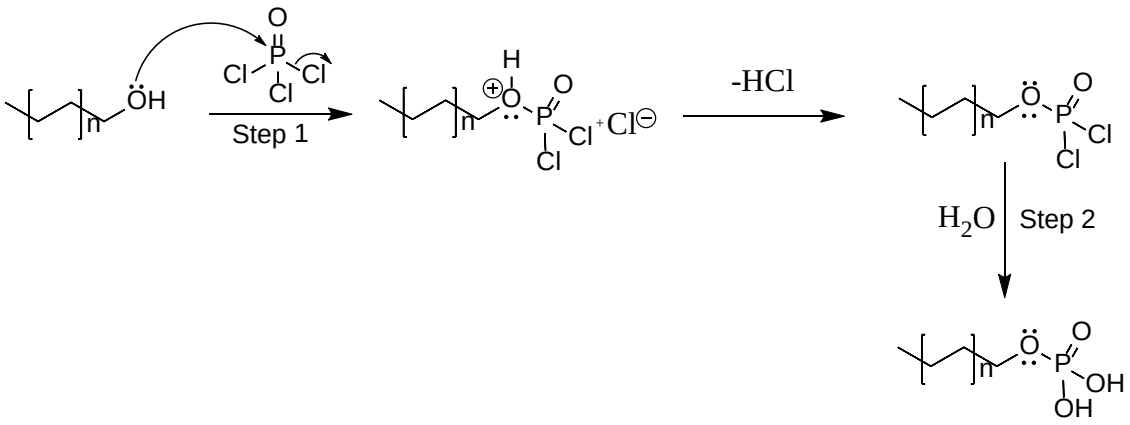

Figure 2.12: Mechanism for the formation of mono-alkyl phosphate esters using $POCl_3$ as a phosphorylating agent with n = 3,5,7

Chapter 3

Results and Discussion

3.1 Chapter background

This chapter will analyse and discuss the results obtained from different characterization techniques performed on the as-synthesized magnetic iron oxide nanoparticles, mono-alkyl phosphate esters, and coated magnetic iron oxide nanoparticles.

3.2 Mono-alkyl phosphate ester: Synthesis and Characterization

3.2.1 Octyl dihydrogen phosphate ester (C8).

For the synthesis of these phosphate esters, phosphorus oxychloride was chosen as the phosphorylating agent because of its relatively low reactivity and selectiveness for the formation of monoesters. This method has only two reaction steps, first step is the formation of the intermediate which is the phosphorodichloridate formed from the nucleophilic attack of the alcohol at the phosphorus atom of the phosphorylating agent. Then follows the hydrolysis step for the formation of the mono-alkyl phosphate ester. Different synthetic procedures were tried but they gave products with high mono/diphosphate ratios [124–126].

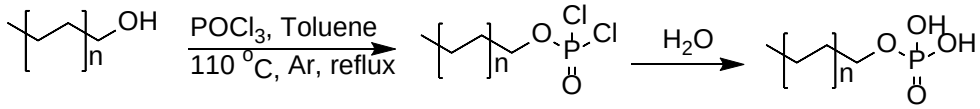

Figure 3.1: Reaction scheme for the synthesis of mono-alkyl phosphates, where n = 3,5,7.

Compound 1 (**C8**) was obtained as a yellowish oil with a 60% percentage yield using a modified procedure described in **Chapter 4** (**4.2.2.1**) [124,127]. This compound was purified by distillation. **Compound 1** ($C_8H_{19}OP$): m/z = 209.2 $[M\text{-}H]^-$. **^{1}H NMR** (400 MHz, Acetone-d_6): ƍ: 10.82 (s, 2H, PO(**OH**)$_2$), 3.99 (q, *J* = 6.7 Hz, 2H, PO**CH$_2$**), 1.70 – 1.61 (m, 2H, POCH$_2$**CH$_2$**), 1.45- 1.21 (m, 10H, -(**CH$_2$**)$_5$-), 0.88 (t, *J* = 6.9 Hz, 3H, -**CH$_3$**). **^{13}C NMR** (101 MHz, Acetone-d_6) ƍ: 67.49 (d, *J* = 5.5 Hz, C8), 32.59 (C6), 31.07

(d, *J* = 7.0 Hz, C7), 30.01 (C5), 29.94 (C4), 26.28 (C3), 23.34 (C2), 14.38 (C1). **^{31}P NMR** (162 MHz, Acetone-d_6): ƍ: -1.15 (O**P**O(OH)$_2$).

From the obtained data it can be said that **Compound 1** was successfully synthesized, it is worth mentioning that from the mass spectrometry results trace amounts of dioctyl phosphate ester formed as also seen in the literature [124]. ^{1}H, ^{13}C, and ^{31}P confirmed the formation of the clean product with no impurities, as shown in the supplementary data in **Figure 5,6&7**. The analytical data matches well with those already published [124,127].

3.2.2 Dodecyl dihydrogen phosphate ester (C12)

The synthetic procedure for **Compound 2** (C12) is discussed in **Session 4.2.2.1** of **Chapter 4**, modified from published papers (124,128). A white amorphous solid was obtained with a percentage yield of 71% and a melting point of 62 ^{o}C (literature percentage yield of 85% (124), and 56% (128)). This compound was purified by recrystallization method in methanol/ ethyl acetate at room temperature with a ¼ ratio (v/v). **Compound 2** ($C_{12}H_{27}O_4P$): mp 62 ^{o}C. m/z = 265.6 $[M-H]^-$. **^{1}H NMR** (400 MHz, Acetone-d_6) δ: 9.52 (s, 2H, PO(**OH**)$_2$), 4.01 (q, *J* = 6.7 Hz, 2H, PO**CH$_2$**), 1.73 – 1.64 (m, 2H, POCH$_2$**CH$_2$**), 1.46 – 1.26 (m, 18H, -(**CH$_2$**)$_9$-), 0.89 (t, *J* = 6.8 Hz, 3H, **CH$_3$**). **^{13}C NMR** (101 MHz, Acetone-d_6) δ: 66.57 (d, *J* = 5.5 Hz, C12), 31.76 (C10), 30.16 (d, *J* = 7.2 Hz, C11), 29.56 – 29.41 (m, C4-C7), 29.02 (m, C8 & C9), 25.37 (C3), 22.45 (C2), 13.47 (C1). **^{31}P NMR** (162 MHz, Acetone-d6) δ:1.11 (O**P**O(OH)$_2$).

Clean ^{1}H, ^{13}C, and ^{31}P NMR spectra were obtained confirming purity of the product. But from the mass spectrometer results trace amount of di-dodecyl phosphate ester (m/ =433) peak was seen, suggesting that this method forms by-products of diphosphate esters as reported the in literature (124,127,128).

3.2.3 Hexadecyl dihydrogen phosphate ester (C16)

The synthetic procedure for **Compound 3** was modified from a paper published by Hanping Li and colleagues [127], this procedure is discussed in **Session 4.2.2.2** of **Chapter 4**. A white amorphous solid powder was obtained with a percentage yield of 76 % and a melting point range of 121–123 ^{o}C. **Compound 3** was purified by

recrystallization method in methanol/ ethyl acetate in a 1/4 ratio (v/v) at room temperature. In ^{31}P NMR a very small peak at 0.32 ppm was observed suggesting the formation of dihexadecyl hydrogen phosphate ester.

Compound 3 ($C_{16}H_{35}O_4P$): mp = 121-123 ^{o}C. m/z = 321.6 $[M-H]^-$. **^{1}H NMR** (400 MHz, Acetone-d_6) **δ**: 4.00 (q, *J* = 6.7 Hz, 2H, PO**CH_2**), 1.68 (p, *J* = 6.6 Hz, 2H, $POCH_2$**CH_2**), 1.44 – 1.26 (m, 26H, -(**CH_2**)$_{13}$-), 0.89 (t, *J* = 6.7 Hz, 3H, **CH_3**). **^{13}C NMR** (101 MHz, Acetone-d_6) δ: 66.46 (d, *J* = 5.5 Hz, C16), 31.75 (C14), 30.18 (d, *J* = 7.2 Hz, C15), 29.50 (q, *J* = 4.4 Hz, C11 – C13), 29.33 (C9 & C10), 29.14 (C6 – C8), 28.94 (C5), 28.75 (C4), 25.38 (C3), 22.44 (C2), 13.46 (C1). **^{31}P NMR** (162 MHz, Acetone-d_6): ƍ = 1.11 (O**P**O$(OH)_2$).

In general, the phosphate esters of three alkyl residues with different chain length were successfully prepared and their identities and purities were confirmed using ^{1}H, ^{13}C, ^{31}P NMR, and MS. Trace amounts of diphosphate esters were observed as mass-to-ratio ion peaks in MS spectra whereas the NMR spectra showed high purity of the mono-alkyl phosphate esters. So, for this compound can say that a salt was formed. The formation of the phosphate esters is confirmed by the presence of the singlet peaks at 10.82 and 9.52 ppm of the hydroxyl groups in ^{1}H NMR in **Compound 1** and **2** respectively. From ^{13}C NMR of all the three compounds two doublet peaks were observed that can be attributed by the coupling of alpha and beta carbons with the phosphate atom. Obtained singlet peaks in ^{31}P NMR confirms high purity of the synthesized compounds. Whereas the MS confirmed the molar masses of the compounds.

For the synthesis of these phosphate esters, phosphorus oxychloride was chosen as the phosphorylating agent because of its relatively low reactivity and selectiveness for the formation of monoesters. This method has only two reaction steps, first step is the formation of the intermediate which is the phosphorodichloridate formed from the nucleophilic attack of the alcohol at the phosphorus atom of the phosphorylating agent. Then follows the hydrolysis step for the formation of the mono-alkyl phosphate ester. Different synthetic procedures were tried but they gave products with high mono/diphosphate ratios [124–126].

3.2.4 Fourier Transform Infrared Spectroscopy of $C_{12}H_{27}O_4P$ and $C_{16}H_{35}O_4P$.

The figure below shows the Fourier Transform Infrared Spectroscopy (FTIR) spectra of the prepared mono-alkyl phosphate ester ($C_{12}H_{27}O_4P$ and $C_{16}H_{35}O_4P$). Characteristic vibrational bands around 2950, 2034–2409, 1465, 770–1230, and 510 cm^{-1} are seen from the FTIR spectra. The two prominent vibration bands around 2950 cm^{-1} can be attributed by the C–H stretching vibrational bands of the alkyl chains in both molecules. The shoulder in 2409 – 2034 cm^{-1} shows the presence of the hydroxyl groups bonded to the phosphorus atom of the phosphoric acid group. The broad strong band ranging from 1230 to 770 cm^{-1} is the P=P, C–O, and P–O vibrational bands. The vibrational frequencies at 520 and 483 cm^{-1} are attributed to the rocking vibrations of C–C and CH_2 and the band around 1610 is the C–O vibrational frequency [14,127,129,130]

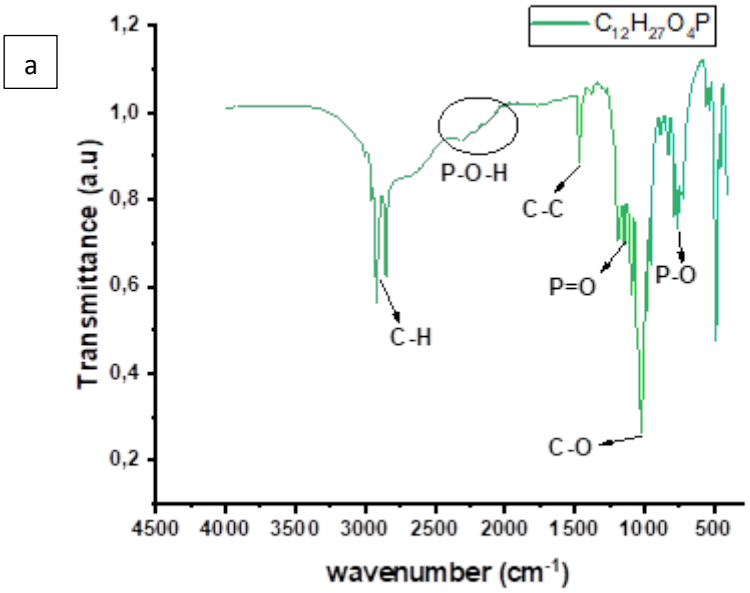

Figure 3.2 (a): FTIR spectra of $C_{12}H_{27}O_4P$.

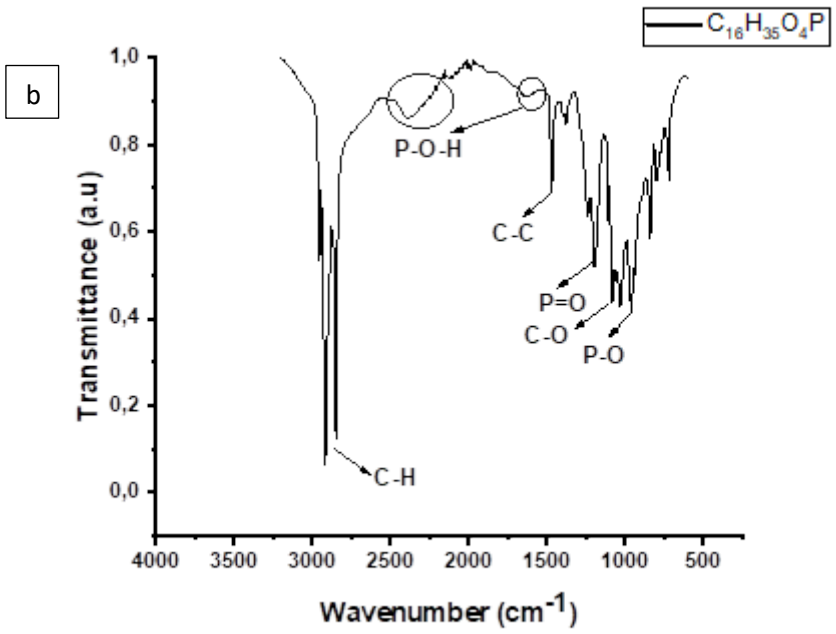

Figure 3.2 (b): FTIR spectra of $C_{16}H_{35}O_4P$.

3.3 Synthesis and characterization of as-synthesized bare and coated magnetite nanoparticles.

3.3.1 Synthesis and coating of magnetite nanoparticles.

Magnetite nanoparticles were prepared using the co-precipitation method, this method was chosen because it is environmentally friendly, an easy synthetic method, and overall mild conditions [52,53]. These nanoparticles were prepared according to this chemical reaction:

$$F_3^{2+} + 2Fe^{3+} + 8OH^- \rightarrow Fe_3O_4 + 4H_2O$$

and the water molecules were removed by drying the as-synthesized magnetite nanoparticles overnight at 60 ^oC in a vacuum oven. The slow addition of ammonium hydroxide i.e., the precipitating agent helped in minimizing the polydispersity of the nanoparticles. As seen from the SEM and TEM micrographs these nanoparticles were polydisperse, similar results were obtained by Ahn and colleagues [58]. Bare magnetite nanoparticles tend to agglomerate and to minimize agglomeration they were functionalized with mono-alkyl phosphate esters via a method discussed in **Chapter 4 (Session 4.3**) they also rendered affinity towards our contaminant of interest

(methylene blue). Black magnetite nanoparticles were collected from the solution using neodymium magnets.

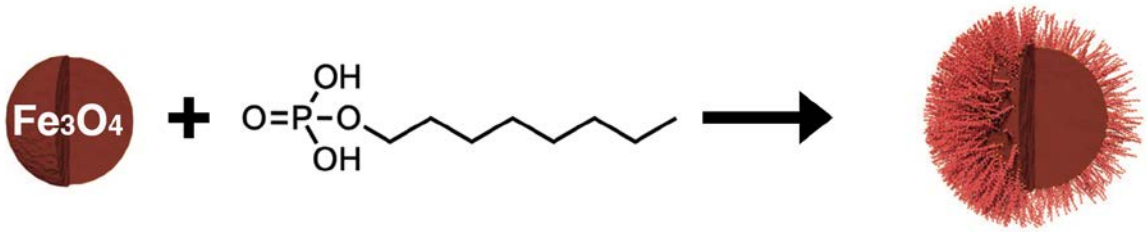

Figure 3.3: Iron oxide nanoparticles covered with amphiphile molecules.

3.3.2 Characterization of as-synthesized nanoparticles.

3.3.2.1 Fourier Transformation Infrared (FTIR) Spectroscopy

The chemical composition of the as-synthesized Fe_3O_4 nanoparticles was characterized using an FTIR spectroscopy as shown in **Figure 3.4 (a)** below. The FTIR experiments were recorded at the wavenumber of 400–4000 cm^{-1} for both experiments. The as-synthesized nanoparticles showed characteristic peaks at 3462, 1630, and 542 cm^{-1}. The presence of the formed Fe_3O_4 nanoparticles is evidenced by the vibrational peak at 542 cm^{-1} for Fe–O bonds [130,131]. The wide stretching frequencies at 1630 and 3462 cm^{-1} are associated with a hydroxyl group on the surface of the nanoparticles and absorbed water molecules, respectively [132,133]. In the coated nanoparticles the vibrational bands at 2917 and 2855 cm^{-1} are attributed to the stretching and bending vibrational bands of CH_3 and CH_2 of the dodecyl phosphate ester; 1465 and 1377 cm^{-1} are the deformation vibrational frequencies of CH_3 and CH_2, respectively. Vibrational frequencies at 764 and 483 cm^{-1} are attributed to the rocking vibrations of C-C and CH_2 [14,127]. Disappearance of the shoulder at 2409–2034 cm^{-1} in the red spectra (coated nanoparticles) shows successful binding of the phosphate ester on the surface of the nanoparticle and the vibration frequency peak at 540 cm^{-1} is associated with the stretching vibrational frequency of Fe-O bonds of the core Fe_3O_4 nanoparticles [130,131]. The broad vibrational peak at 1230–770 cm^{-1} is for the stretching vibrational frequencies of P=O, C–O, and P–O bonds [134]. The presence of the vibrational bands for C–C, P=O, C–O, P–O, and C–H on the $Fe_3O_4@PO_4C_{12}H_{25}$ spectra (red spectra) confirmed the successful coating of the nanoparticles with mono-alkyl phosphate esters.

Figure 3.4 (b) shows the FTIR spectra of $Fe_3O_4@PO_4C_{12}H_{25}$ before and after three usability studies. When comparing these two spectra's there are no major differences observed. Same characteristic vibrational peaks for C–H, C–C, P=O, P–O, C–O and Fe–O are observed in both spectra meaning that even after three recycles these nanoparticles did not lose their composition. The FTIR spectra of the recovered nanoparticles after three recycles shows a more prominent peak for the C–C which this can be attributed by the presence of the methylene blue dye molecules on the surface of the nanoparticles. The MB dye molecules binded via weak hydrophobic effect. The presence of the Fe–O bond confirms that these nanoparticles are stable and they can be used at least three times without losing their stability and composition.

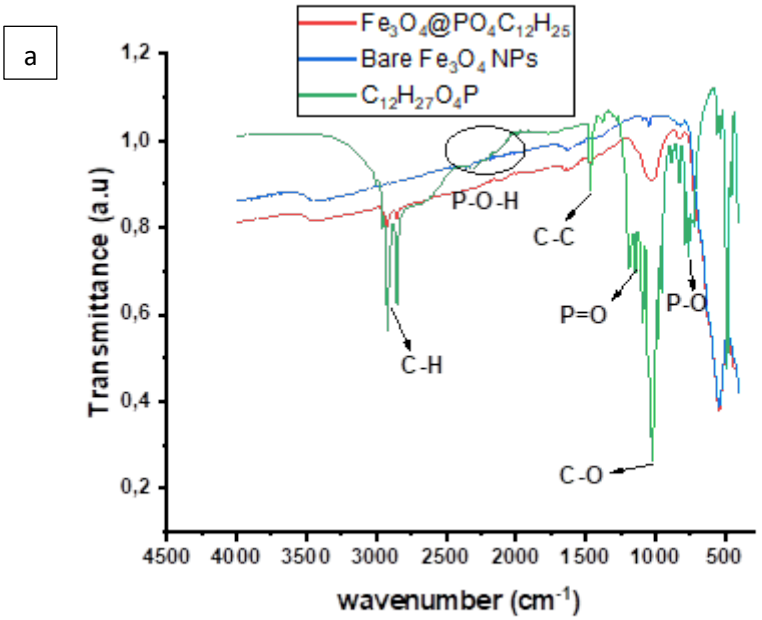

Figure 3.4 (a): FTIR spectra of bare as-synthesized Fe_3O_4 NPs, $Fe_3O_4@PO_4C_{12}H_{25}$, and $PO_4C_{12}H_{25}$.

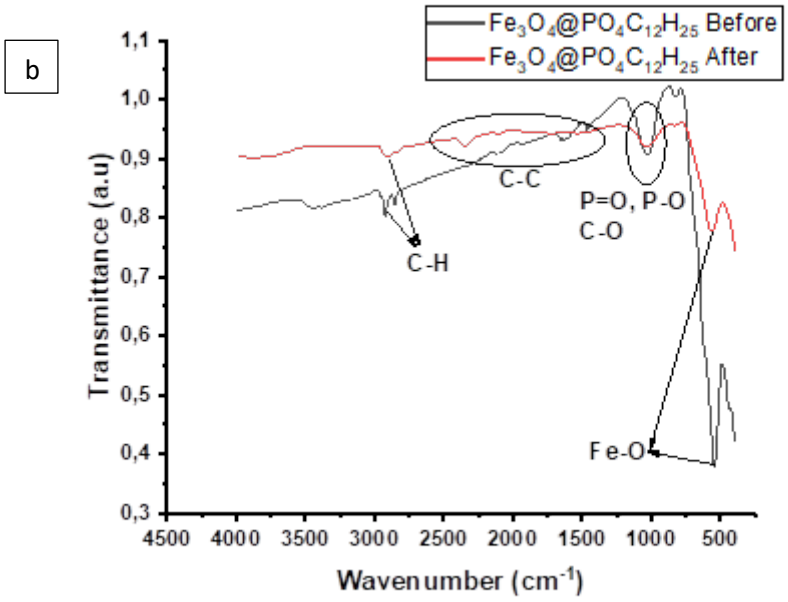

Figure 3.4 (b): FTIR spectra of $Fe_3O_4@PO_4C_{12}H_{25}$ before and after three reusability studies.

3.3.2.2 SEM and EDS analysis

Figure 3.5 (a) & (b) shows SEM images of bare magnetite nanoparticles and mono-alkyl phosphate ester functionalized magnetite nanoparticles respectively. SEM spectroscopy was performed to know the morphological structure of the as-synthesized nanoparticles. Bare magnetite nanoparticle micrographs show uneven circular shape nanoparticles, and they are polydispersive in size with particle diameters ranging from 12-16 nm for the naked and 17-22 nm for the coated nanoparticles, respectively. Literature showed that particles synthesized using the co-precipitation method tend to suffer from polydispersity [58,135]. Bare nanoparticles tend to agglomerate because of their increased surface-to-volume ratios and the formation of aggregates via covalent or metallic bonds [136]. Functionalization of the magnetite nanoparticles can be confirmed by better particle circular shapes as compared to **Figure 3.5 (a)**. No significant changes were observed on the two micrographs except for the nanoparticle diameter sizes ranging from 17-22 nm. These results were comparable to published findings [137].

Energy dispersive X-ray (EDS/EDX) spectroscopy was used to determine the elemental composition of bare and functionalized magnetite nanoparticles. **Figure 3.5 (c&d)** shows EDS spectra of bare magnetite nanoparticles and mono-alkyl phosphate ester functionalization respectively. **Figure 3.5 (c)** shows the presence of iron (Fe) and oxygen (O) confirming that iron oxide nanoparticles were successfully prepared [138]. The presence of carbon (C) and chlorine (Cl) can be residues from the washing of the adsorbent (138). Functionalization of the magnetite nanoparticles was confirmed by the presence of the additional elements, phosphorus (P), and much larger amount of carbon (C) in the sample, **Figure 3.5 (d)**. No foreign elements were observed on the EDS spectra meaning that pure functionalized nanoparticles were obtained. It should also be noted that the EDS instrument cannot detect light elements like hydrogen, helium, and aluminium, also it suffers to quantify elements such as oxygen, carbon, and nitrogen because of their omnipresence in the environment and coating of samples with carbon layer during sample preparation might have affected the results [179].

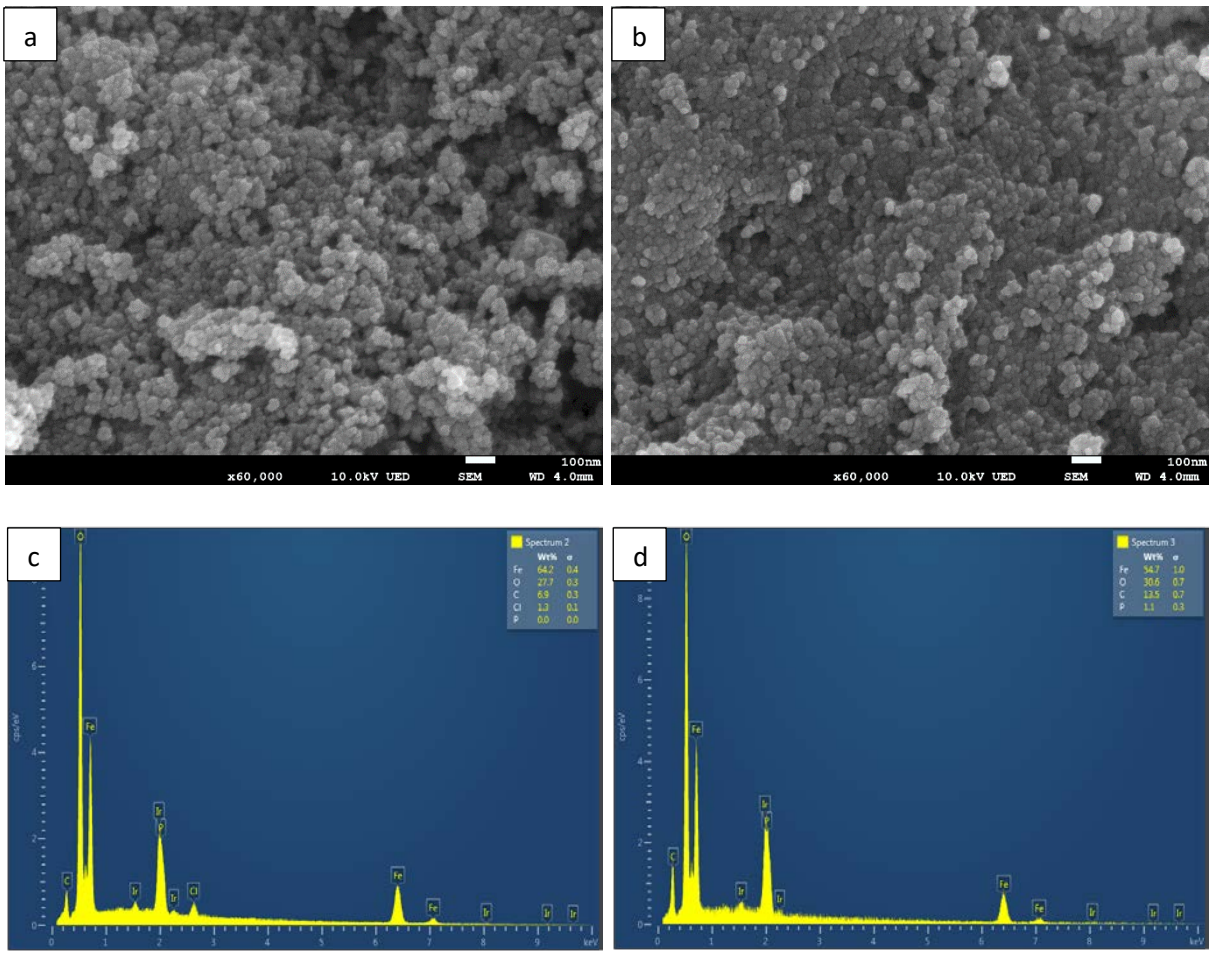

Figure 3.5: SEM images and EDS data. SEM images of (a) bare and (b) coated magnetite nanoparticles. EDS spectra of (c) bare and (d) Fe_3O_4@$PO_4C_{12}H_{25}$.

3.3.2.3 Transmission Electron Microscopy (TEM) analysis

Figure 3.5 below shows the TEM analysis images of the as-synthesized and coated nanoparticles. The as-synthesized nanoparticles show a spherical morphology and the increase in the particle size after coating with mono-alkyl phosphate esters confirms the successful coating of the nanoparticles as shown in **Figure 3.6**. The dark core on the TEM micrograph **Figure 3.6 (b)** shows the magnetite nanoparticles and the shell shows the mono-alkyl ester coating, which confirms the results obtained from FTIR. The coated nanoparticles' coalescence can be caused by the lipophilic intersurfactant interactions [135]. The size increase after coating was confirmed by the TEM micrographs (ImageJ software), where the estimated mean particle sizes

were ranging from 12 to 16 nm and 17 to 22 nm for as-synthesized magnetite nanoparticles and coated magnetite nanoparticles, respectively. These results match well with obtained particle size from the XRD measurements using the Scherrer equation for estimation of the particle size. These particles are polydisperse, this is caused by the difficulty in controlling the particles when using the co-precipitation method for the synthesis of nanoparticles as reported in the literature.

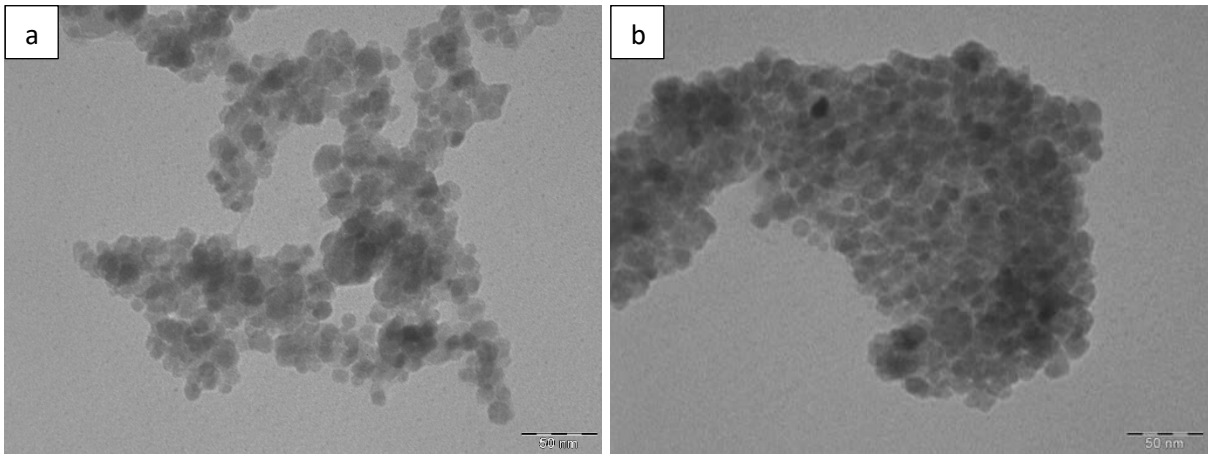

Figure 3.6: TEM images of (a) bare Fe_3O_4 NPs and (b) $Fe_3O_4@PO_4C_{12}H_{25}$.

3.3.2.4 Powder X-ray Diffraction (PXRD)

The X-ray diffraction spectra of the as-synthesized magnetite nanoparticles is shown in **Figure 3.7** below, which clearly shows the well-defined crystallinity of the nanoparticles. The diffraction peaks at 2θ = 19^o, 30^o, 35^o, 36^0, 43^o, 53^o, 56^o, 61^o, 71^o, and 81^o were assigned to (111), (220), (311), (222), (400), 422), (511), (440), (533), and (731) indication reflections of Fe_3O_4. All the diffraction peaks obtained are coherent with the standard characteristic diffractions of Fe_3O_4 inverse spinel structure found in the literature [130,139,140]. No foreign diffraction peaks were observed indicating that the as-synthesized magnetite nanoparticles are pure with no impurities from the unreacted precursors and it can be observed from the PXRD patterns, diffraction peaks are broad indicating smaller particle sizes in the nano range. The particle diameter is calculated using the Scherrer formula:

$$D = \frac{K\,\lambda}{\beta Cos\theta} \qquad \text{(eq. 3.1)}$$

where K is a dimensionless shape factor, λ is the X-ray wavelength, β is the line broadening at half the maximum intensity (FWHM) and θ is the Bragg angle in degrees. The obtained mean particle size of the as-synthesized Fe_3O_4 nanoparticles using the coprecipitation is 13 nm which corresponds well with the particle size results obtained from TEM analysis [130,139,140].

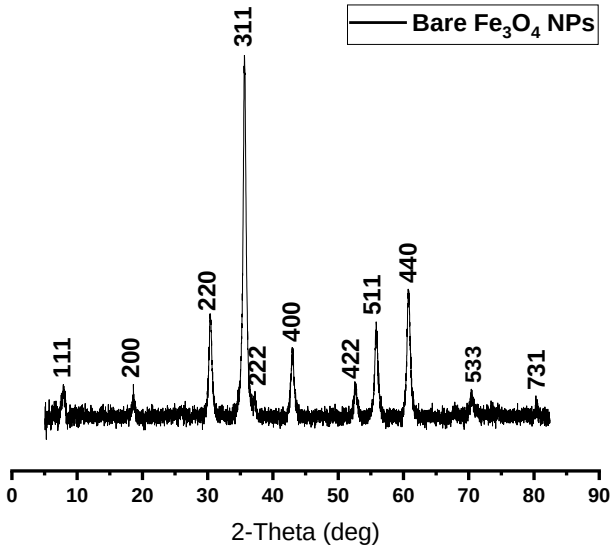

Figure 3.7: PXRD spectra of the as-synthesized magnetite nanoparticles.

3.3.2.5 Thermal Gravimetric Analysis

Thermal gravimetric analysis of as-synthesized magnetite and functionalized nanoparticles was performed on a TGA spectroscopy from room temperature to 700 ^oC under a nitrogen atmosphere. These TGA thermograms were performed to compare the thermal stability of as-synthesized magnetite nanoparticles before and after the introduction of mono-alkyl phosphate esters onto their surfaces. In **Figure 3.8 (a)** the bare magnetite nanoparticles showed thermal stability after 240 ^oC with a weight loss of 4.13% which can be assigned to the loss of water molecules on the surface of the nanoparticles as seen from the FTIR spectra. After the TGA analysis, the colour of the nanoparticles changed to a brown-reddish colour which can be attributed by the formation of Fe_2O_3 nanoparticles at high temperatures. Similar results

were published by Halik and the leagues [129]. TGA thermogram of functionalized magnetite nanoparticles with 50 mg/L of **C12** (**Compound 2**) **Figure 3.8 (b)** shows that these nanoparticles were thermally stable from 500 ^{o}C with a total weight loss of 19.15%. The weight loss was attributed to the decomposition of the alkyl chain and the phosphate group. Similar thermograms were published in the literature [129].

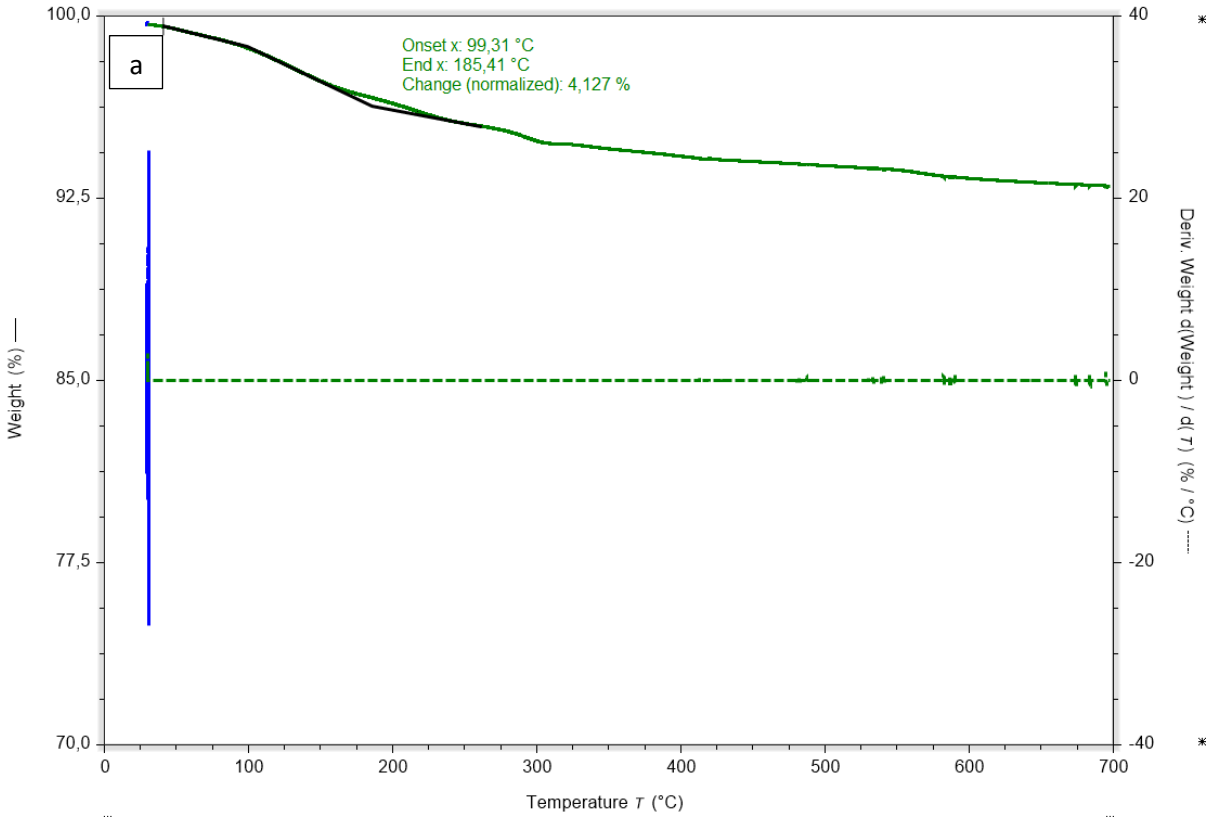

Figure 3.8 (a): TGA thermogram of bare Fe_3O_4 NPs

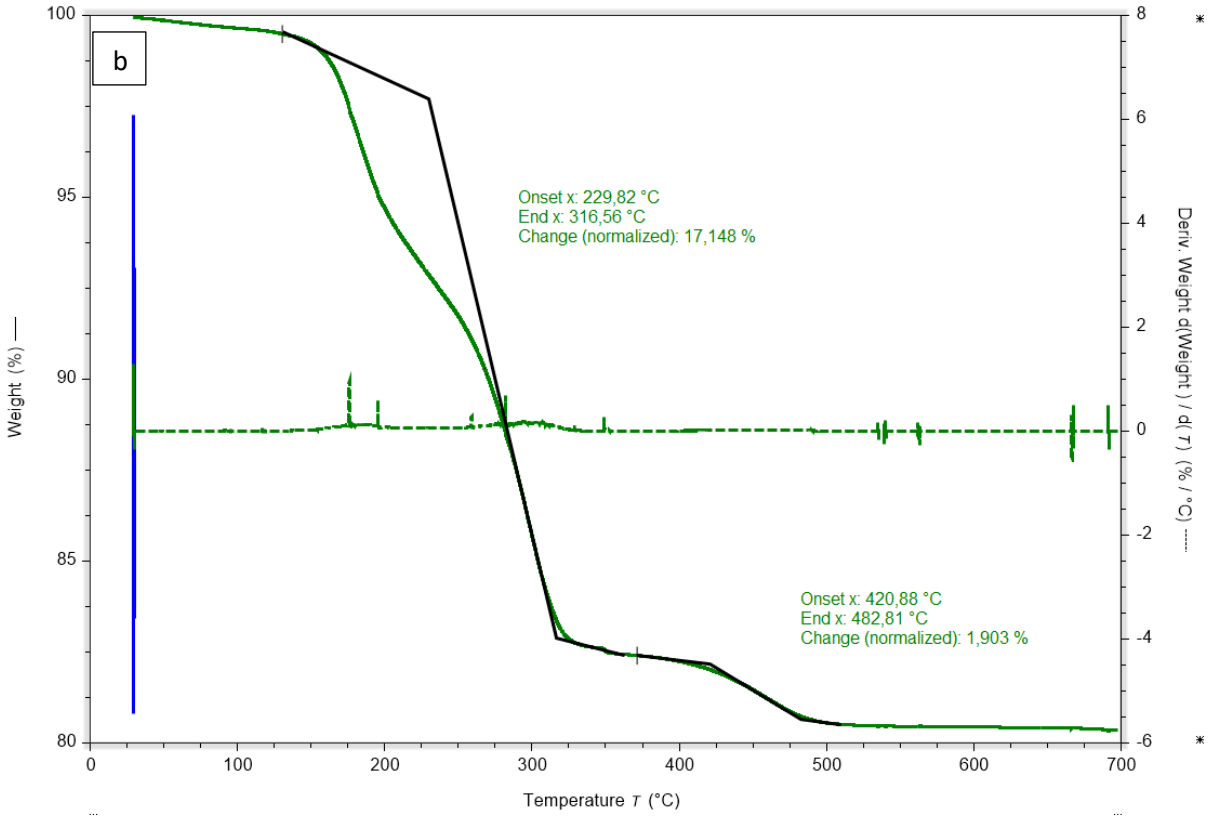

Figure 3.8 (b): TGA thermogram of Fe_3O_4@$PO_4C_{12}H_{25}$.

3.4 Adsorption studies

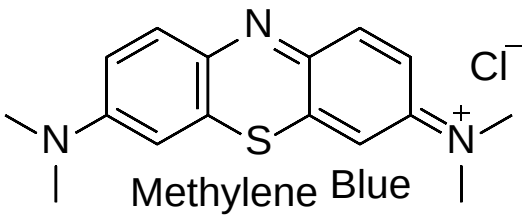

Figure 3.9: Chemical structure of methylene blue dye.

3.4.1 Effect of pH

The pH of a solution is important in dye sorption efficiency because it influences the degree of ionization and the surface properties of the sorbent, which affects the MB (adsorbate) charge. This further regulates the adsorption process by adjusting the adsorbent's adsorption capacity [141]. The effect of solution pH was investigated during these adsorption studies in the pH range of 4–10 with methylene blue initial dye

concentration of 300 mg/L, sorbent amount of 10 mg, and sonicated for 30 minutes. As can be seen from **Figure 3.10**, the significant difference in the removal percentages of MB dye from pH 4 to 10. This can be caused by the reduction of the phosphate ester on the magnetite surface due to the phosphate group protonation (142) and desorption. Whereas in high pH (>10) values, it becomes too basic for practical [143]. Better removal dye efficiencies are observed in the pH range of 8-10 with 10 having the optimum efficiency (81% dye removal %).

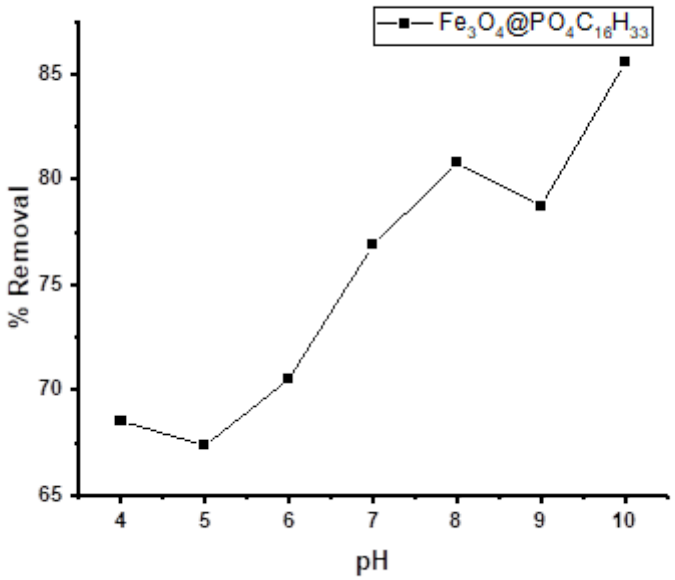

Figure 3.10: Effect of solution pH on the adsorption of MB C_o = 300 mg/L, sorbent amount = 10 mg, t = 30 min sonicated at 25 ^oC.

3.4.2 Effect of sorbent amount

The adsorption capacity of these mono-alkyl phosphate functionalized magnetite nanoparticles was investigated using sorbent amounts ranging from 0.01–0.05 g sonicated for 40 minutes. The sorbent amount, size, and surface area play a significant role in determining the adsorption capacity of an adsorbent. The availability of vacant sites on the surface of the adsorbent limits the movement of the dye molecules toward the adsorbent surface [144,145]. These mono-alkyl phosphate esters functionalized magnetite molecules adsorb dye molecules on their surfaces via the dispersion forces and weak Van Der Waals attraction through the alkyl chain of the functionalization

molecules and also due to electrostatic effects, if the NP surface is charged. Nanoparticles and functionalized nanoparticles have high adsorption capacity for dye molecules due to their small particle sizes of less than 20 nm making them have high specific surface area. The sorbent amount for removal of MB was investigated at different sorbent doses (0.01, 0.02, 0.03, 0.04, and 0.05 g) while other adsorption factors such as pH = 10, contact time = 30 min at room temperature (25 ^{o}C) as shown in **Figure 3.11** below. As can be seen from **Figure 3.11** below, as the amount of adsorbent increased from 0.01–0.05 g removal percentage of MB increased significantly (from 67 to 76 % for C16, from 67 to 74 % for C12, from 65 % to 70 % for C8 and from 62 to 68 % for Fe_3O_4 bare NPs). This high MB removal amount for increased adsorbent dosage is caused by the increased amount of adsorption sites due to the increased specific surface area of the adsorbent [145]. At lower adsorbent amounts, less amount of MB is removed due to the lower amount of adsorption sites on the adsorbent [146]. As can be seen from **Figure 3.11** below, the plot of q_t (mg/g) vs sorbent amount (g), 0.01 g of the adsorbent was chosen as the optimum sorbent dosage for all other studies since it gave the highest adsorption capacity (mg/g) using the mass balance equation (**eq. 4.2**) **Chapter 4**. The mass-balance equation for determining adsorption capacity takes into consideration the amount of adsorbent used and adsorbate solution volume [147].

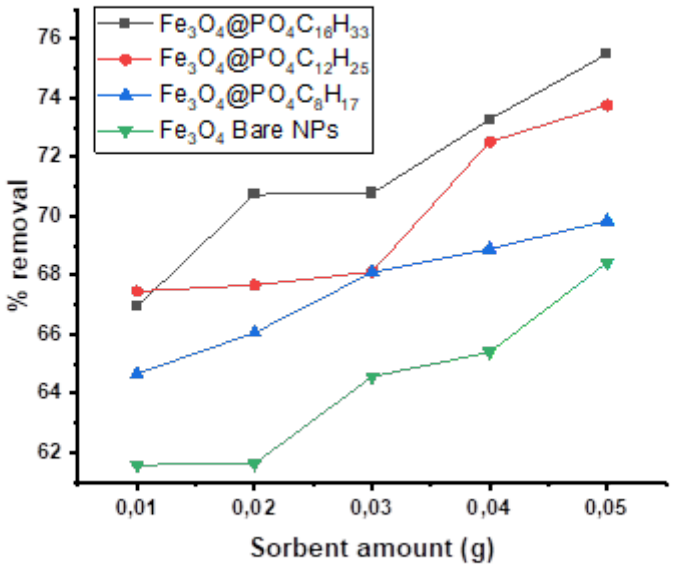

Figure 3.11: Sorbent amount effect on the adsorption of MB onto the as-synthesized adsorbents C_o = 500 mg/L, pH = 10, t = 40 min and sonicated at 25 ^oC.

3.4.3 Effect of temperature

The temperature of the solution at which adsorption takes place is one of the factors that affect the adsorption process. It tells us whether the process is exothermic or endothermic and it is important to determine the optimum temperature that can be used to obtain a high adsorption efficiency. Temperature effect on the adsorption process was investigated at different temperatures of 20 ^oC, 30 ^oC, 40 ^oC, 50 ^oC, and 60 ^oC. **Figure 3.12** shows the obtained results from these studies that the removal percentage increased with an increase in temperature from 20 ^oC to 60 ^oC meaning that the adsorption process depends on temperature (endothermic process). Similar results for the adsorption of MB using similar adsorbers are reported in the literature [148,149,150], and increase in temperature also increases the number of active sites on the surface of the adsorbent [150].

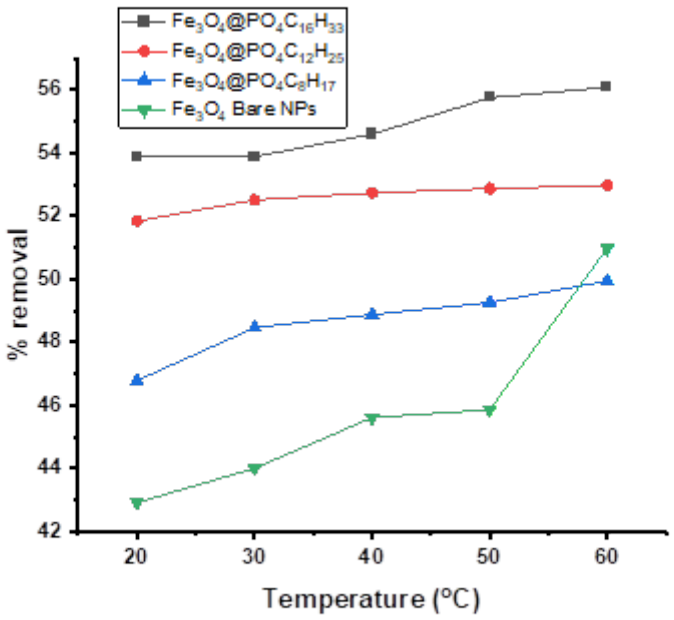

Figure 3.12: Temperature effect on the adsorption of MB onto the as-synthesized adsorbents, C_o = 500 mg/L, sorbent amount = 10 mg, pH = 10, and t = 30 min.

3.4.4 Effect of contact time

To determine the equilibrium adsorption capacity of as-synthesized adsorbents, four solutions of 500 mg/L, pH = 10 were prepared and 10 mg of adsorbent was added and sonicated according to the time intervals as shown in **Figure 3.13** below. As observed from **Figure 3.13** below, the dye removal efficiency increased for a longer contact time till equilibrium was reached (within 120 min). A similar trend has been seen by other researchers for MB adsorption studies [151,152]. A slight difference in the time it took for the adsorbents to reach equilibrium was observed. During the initial times of adsorption, more vacant adsorption sites are available hence the faster adsorption rates and decreases as the MB molecules in the solution attach on the surface of the adsorbents with time. It was difficult for the dye molecules to attach on the remaining vacant adsorption sites because of the repulsion forces between the adsorbate molecules (MB) already attached and bulk phases [153–155]. Fe_3O_4@C16 showed better adsorption capacity at equilibrium compared to the other three adsorbents, this can be attributed to the longer alkyl chain giving the adsorbent better affinity towards adsorption of MB via the weak dispersion forces and hydrophobic effect. It is observed (**Figure 3.13**) that the longer the alkyl chain the better the adsorption capacity for MB

and the longer the time it takes to reach equilibrium. Bare Fe_3O_4 NPs showed lower adsorption capacity for MB because of the repulsive forces between the dye molecules and the surface of the naked magnetite nanoparticles.

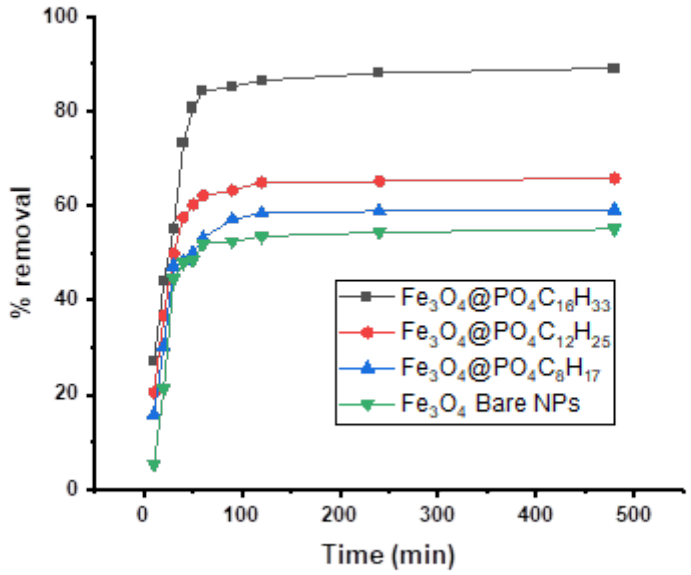

Figure 3.13: Contact time effect of the dye solution and the adsorbent, C_o = 500 mg/L, sorbent amount = 10 mg, pH = 10, and sonicated at 25 ^oC.

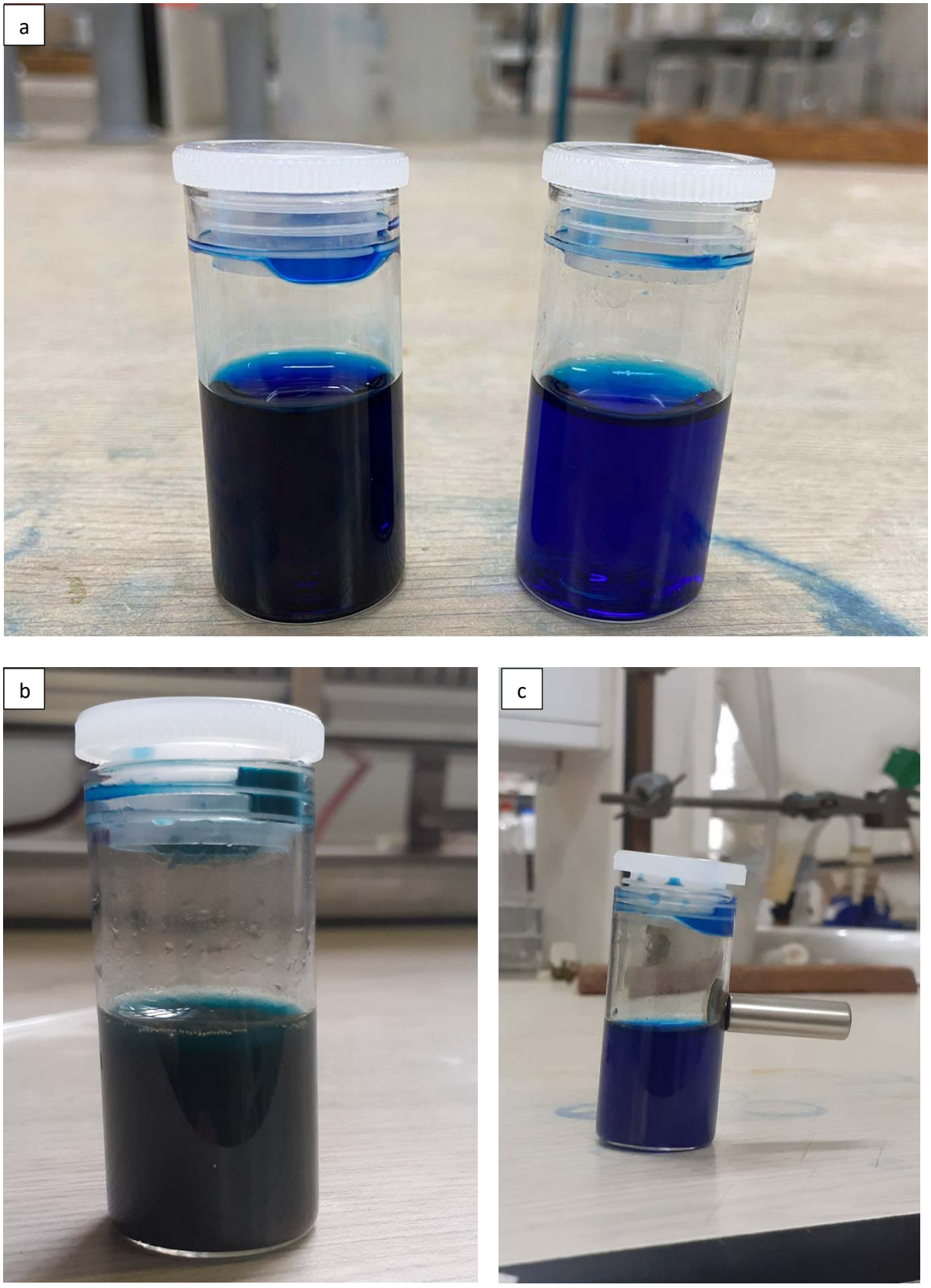

Figure 3.14: (a) Shows initial and final MB solutions, (b) during the sonication process, and (c) removal of magnetite nanoparticles using neodymium magnetic, after 480 min of sonication.

3.4.5 Recycle use of adsorbents

The reusability study results of the as-synthesized adsorbents are shown in **Figure 3.15.** Reusability is an important factor for adsorbents when considering their practical application in wastewater treatment industries because it will save overall costs in preparing the materials and minimize secondary pollution that can be caused by adsorbents [156]. These adsorbents were sonicated in ethanol to remove the adsorbed MB molecules adsorbed on their surfaces, and dried in a vacuum oven overnight at 60 ^{o}C as other researchers reported [157]. MB dye removal percentage slightly decreased after the adsorption-desorption cycles which can be attributed to the increase in the amount of MB molecules that strongly attached to the functionalized magnetite nanoparticles via dispersion forces [151]. All four adsorbents showed better resilience for the first four adsorption-desorption cycles. Bare NPs showed higher resilience than the functionalized nanoparticles this can be attributed to the repulsive forces between the adsorbent and MB molecules. These adsorbents can be employed in water purification plants for the removal of dyes, and they can at least be used 5 times with a significant decrease in the adsorption capacity. But since iron is the second most abundant element on earth it is cheaper, and the co-precipitation method for the synthesis of magnetite nanoparticles is easy and environmentally friendly these adsorbents can be synthesized in large quantities and be used once. It has also been reported that these magnetite nanoparticles are not toxic to the environment and can be utilized using a standard industrial process to produce iron from the iron ore, whereas the possible toxic pollutant immobilized on the particles will be incinerated during this process [31,46].

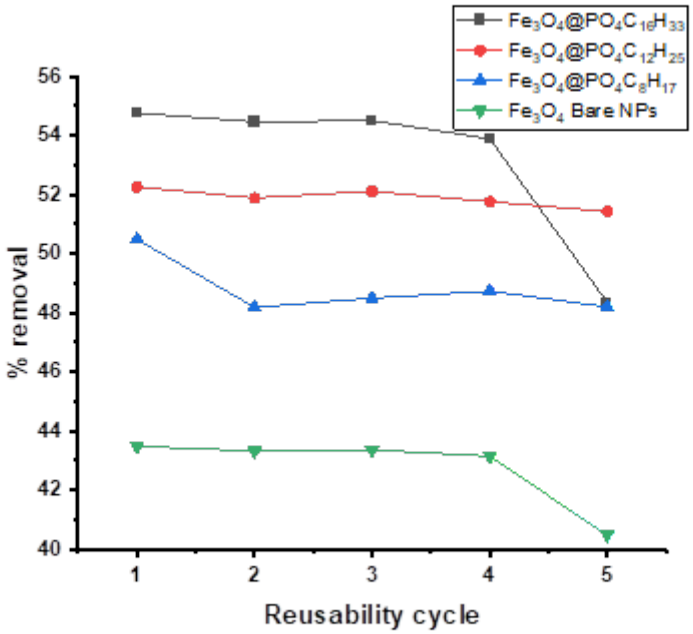

Figure 3.15: Reusability cycle effect on the adsorption of MB onto the as-synthesized adsorbents C_o = 500 mg/L, sorbent amount = 10 mg, pH = 10, t = 30 min and sonicated at 25 ^oC.

3.5 Adsorption isotherms

Several adsorption isotherm models have been studied in the literature in order to understand and analyse the experimental data. Freundlich and Langmuir's models are the most commonly used of all available models. These two models will be used to fit the obtained experimental data in this study.

3.5.1 Freundlich isotherm

The Freundlich isotherm suggests that there is a multi-layer formation of the adsorbate on the surface of the adsorbent, and this occurs via heterogeneous adsorption sites on the adsorbent.

The linearized form of the Freundlich isotherm is given by the equation below:

$$\log q_e = \log K_F + 1/n \log C_e \qquad \text{(eq. 3.2)}$$

where C_e is the equilibrium concentration (mg/L), K_F is the Freundlich isotherm constant (L/mg), and n is the Freundlich adsorption intensity. With n less than 1 showing poor affinity of the adsorbent for adsorbing the contaminants of interest. A linear plot of log q_e versus log C_e as shown in **Figure 3.16 (b)**, gives the Freundlich isotherm parameters, where the Freundlich isotherm constant can be obtained from the intercept and n from the slope.

3.5.2 Langmuir isotherm

A Langmuir isotherm predicts that during an adsorption process an adsorbate monolayer form on the surface of the adsorbent and all the adsorption sites available are equivalent. According to this model, adsorbate saturates after the formation of the monolayer. The linearized form of the Langmuir isotherm is given by the following equation:

$$C_e/q_e = 1/bq_{max} + 1/q_{max}\ (C_e) \qquad \text{(eq. 3.3)}$$

where q_e is the amount of dye adsorbed at equilibrium (mg/g), q_{max} is the maximum monolayer adsorption capacity (mg/g) related to the Langmuir isotherm model and b is the Langmuir isotherm constant (L/mg) associated to adsorption energy. A linearized plot of the Langmuir isotherm is shown in **Figure 3.16 (a)** below, a plot of C_e/q_e versus C_e. The Langmuir model parameters q_{max} and b were calculated from the slope and intercept respectively.

The obtained isotherm parameters and correlation coefficients (R^2) for both Freundlich and Langmuir isotherm models are summarized in **Table 3.1**. As seen from the linearized adsorption isotherm plots in **Figure 3.16 (a) & (b)**, the adsorption process in this study well fitted for the Langmuir model (R^2 ranging 0.975 - 0.982) compared to those of the Freundlich model (R^2 ranging 0.771 - 0.942). From the Langmuir model, the values of the maximum monolayer adsorption capacity were found to be 317, 301, 265, and 241 mg/g for Fe_3O_4@C16, Fe_3O_4@C16, Fe_3O_4@C16, and Fe_3O_4. Bare NPs respectively, and the b values were found to be 0.028, 0.030, 0.074, and 0.062 L/mg for Fe_3O_4@C16, Fe_3O_4@C16, Fe_3O_4@C16, and Fe_3O_4 Bare NPs respectively. From the Freundlich model, the Freundlich adsorption intensity constants (n) were obtained to be greater than one meaning that the affinity between the adsorbents and MB dye

molecules was strong as seen from the thermodynamic parameters. Good correlation coefficients were obtained for the Langmuir model meaning that the experimental data fitted well with the Langmuir isotherm model for the adsorption of MB dye.

Table 3.1: Data summary of Langmuir and Freundlich isotherm parameters

$C_e/q_e = 1/q_{max}b + C_e/q_e$ $\quad\quad$ $\log q_e = \log K_f + 1/n \log C_e$

Material	Langmuir isotherm				Freundlich isotherm			
	Equation	q_{max} (mg/g)	b (L/mg)	R^2	Equation	n	K_f (L/mg)	R^2
Fe_3O_4@C16	Y = 0.00315x + 0.11143	317	0.028	0.978	Y = 0.33072x + 3.89262	3.024	49.039	0.771
Fe_3O_4@C12	Y= 0.00332x + 0.11241	301	0.030	0.975	Y = 0.3408x + 3.76932	2.934	43.351	0.942
Fe_3O_4@C8	Y = 0.00377x + 0.05066	265	0.074	0.982	Y = 0.28906x + 4.06455	3.459	58.239	0.906
Bare NPs	Y = 0.00415x + 0.06662	241	0.062	0.978	Y = 0.721x + 4.01017	1.387	55.156	0.909

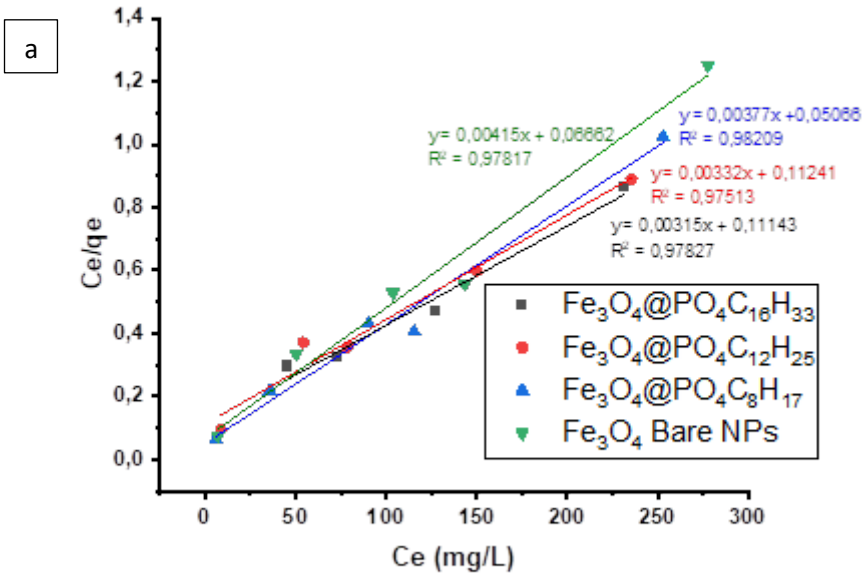

Figure 3.16 (a): Experimental data fitted into the linearized Langmuir isotherm model.

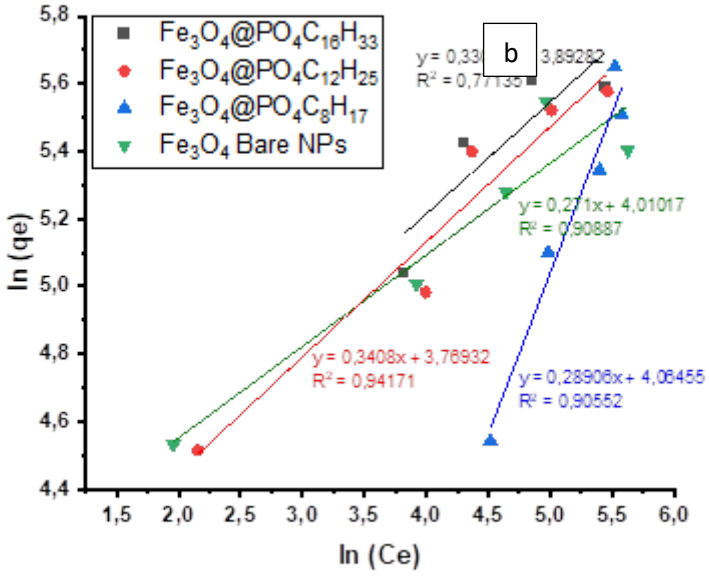

Figure 3.16 (b): Experimental data fitted into the linearized Freundlich isotherm model.

3.6 Adsorption kinetics

Kinetic studies of the adsorption process of MB dye onto the surface of different adsorbents provide crucial adsorption parameters such adsorption rate of dye onto the adsorbent, maximum adsorption capacity (q_e) values, etc. In this project, the two most used kinetic models in adsorption studies which are pseudo-first order and Ho's pseudo-second-order kinetic models were evaluated for a better understanding of the adsorption mechanism. These studies were performed at ambient temperature (25 ^oC), initial concentration = 500 mg/L of MB dye solution, 10 mg of adsorbent, and at pH = 10. The solutions were sonicated for time intervals ranging from 0 - 480 min as shown in **Figure 3.13**. As observed from **Figure 3.13** the adsorption rate of MB was fast for the initial stages (0 - 90 min) of the adsorption process.

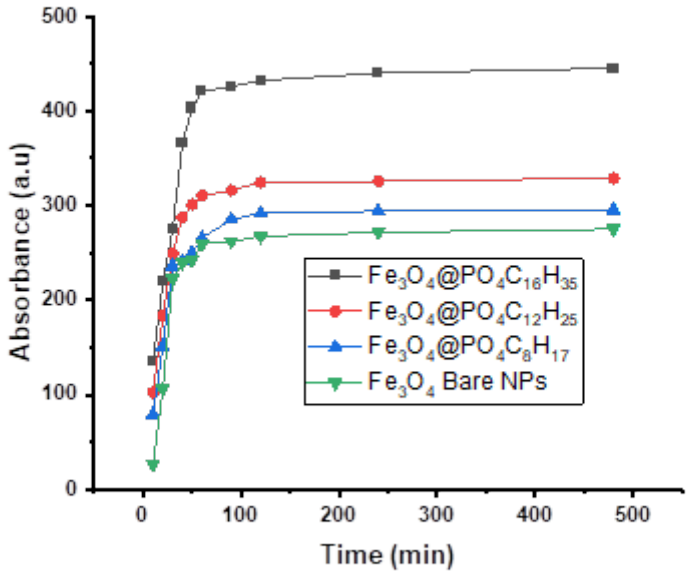

Figure 3.17: Kinetic studies for adsorption of MB using the as-synthesized nanoparticles.

3.6.1 Pseudo-first-order equation

The experimental data were fitted in pseudo-first order and pseudo-second-order kinetic models. Linearized forms of the kinetic models were plotted for the determination of the kinetic parameters. A plot of ln (q_e - q_t) versus t (min) used to determine the kinetic parameters from the pseudo-first-order model:

$$\ln (q_e - q_t) = \ln q_e - k_1 t \qquad \text{(eq. 3.7)}$$

where k_1 (min^{-1}) is the equilibrium rate constant related to the pseudo-first-order equation, q_t and q_e are the adsorption capacity at time t (min) and equilibrium respectively, and t (min) is the adsorption time. k_1 and q_e were determined from the slope and intercept of the linear plot of ln (q_e - q_t) versus t (min) as shown in **Figure 3.18**, the results are summarized in **Table 3.3**.

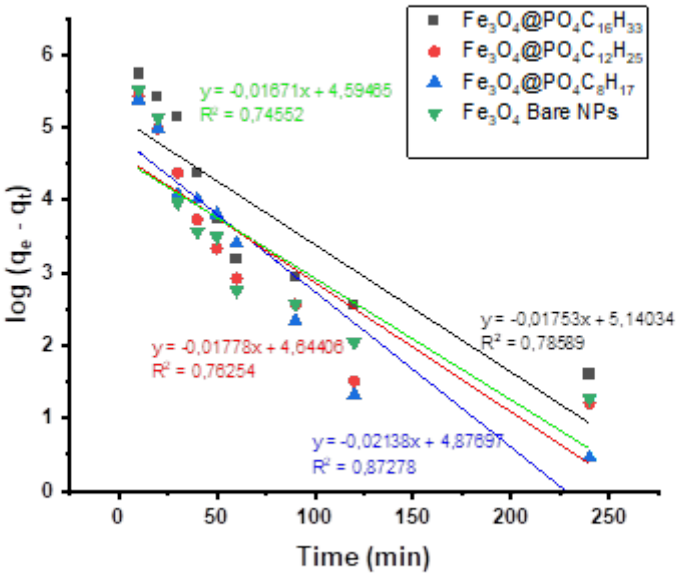

Figure 3.18: Experimental data fitted into the Pseudo-first-order kinetic model for as-synthesized adsorbents.

3.6.2 Pseudo-second-order equation

The pseudo-second-order model parameters were obtained from a plot of t/q_t (min.g/mg) versus t (min). The following equilibrium adsorption pseudo-second-order equation was used to determine pseudo-second-order parameters:

$$t/q_t = 1/k_2 q_e^2 + t/q_e \qquad \text{(eq. 3.8)}$$

where k_2 (g mg^{-1} min^{-1}) is the equilibrium rate constant related to the pseudo-second order. The pseudo-second-order rate constant was determined from the linear plot of t/q_t (min.g/mg) versus t (min) from **Figure 3.19** below.

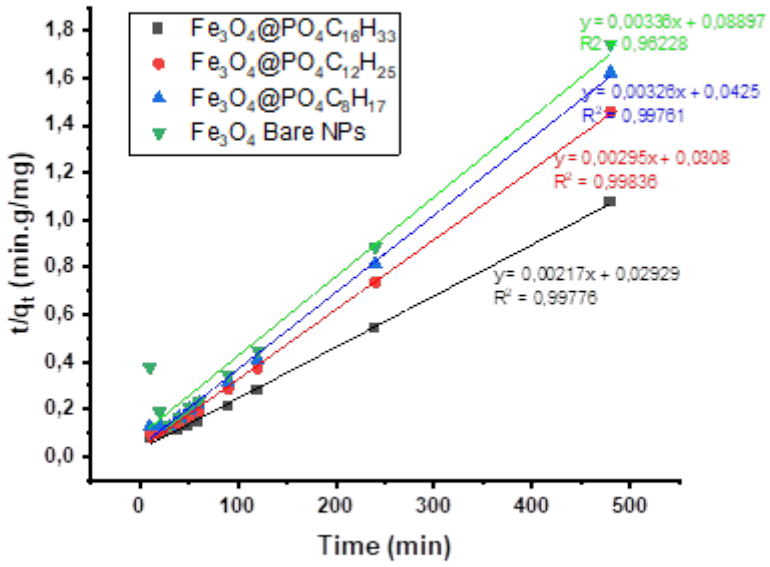

Figure 3.19: Experimental data fitted into the Pseudo-second-order kinetic model for as-synthesized adsorbents.

Table 3.2: Kinetic parameters for adsorption of MB.

$\ln(q_e-q_t) = \ln q_e - k_1 t$ $\qquad$ $t/q_e = 1/(k_2 q_e^2) + 1/q_e$

Adsorbent	C_o (mg/L)	$q_{e,exp}$ (mg/g)	Pseudo-first order			Pseudo-second order		
			k_1 (min^{-1})	q_e (mg/g)	R^2	K_2 ($g.mg^{-1}.min^{-1}$)	q_e (mg/g)	R^2
C16	500	445	-0.000037	171	0.7859	0.000016	461	0.9978
C12	500	329	-0.000037	104	0.7625	0.000283	338	0.9984
C8	500	296	-0.000045	131	0.8728	0.000250	306	0.9976
Bare NPs	500	275	-0.000035	99	0.7455	0.000127	298	0.9623

According to the correlation coefficients (R^2) values obtained ranging from 0.746 - 0.873 for the pseudo-first-order model and ranging from 0.962 - 0.998 for the pseudo-second-order model, kinetic data fitted well the pseudo-second-order model. This decision was not only taken by considering the correlation coefficients (R^2) only, but also the experimental adsorption capacities of 445, 329, 296, and 275 mg/g for Fe_3O_4@C16, Fe_3O_4@C12, Fe_3O_4@C8, and Fe_3O_4 Bare NPs respectively were

compared to the adsorption capacities obtained from the pseudo-second-order model were 461, 338, 306, and 298 for Fe_3O_4@C16, Fe_3O_4@C12, Fe_3O_4@C8, and Fe_3O_4 Bare NPs, respectively. These results show good comparability between the experimental q_e ($q_{e,exp}$) and the pseudo-second-order calculated q_e ($q_{e,cal}$) adsorption values as reported from literature for similar studies [156]. From these results, it can be concluded that the adsorption process of MB onto these as-synthesized nano-adsorbents can be described using the pseudo-second-order model. This model predicts that the rate of adsorption strongly depends on the adsorption capacity of the adsorbent not on the adsorbate concentration. Using this model one can predict the adsorption capacity of an adsorbent by assuming that chemisorption is the rate-limiting step [158-161].

Table 3.3: Comparison of the mono-alkyl phosphate ester coated magnetite nanoparticles with other adsorbents for removal of MB dye.

Adsorbent	q (mg/g)	Reference
Fe_3O_4@C16	445	This work
Fe_3O_4@C12	329	This work
Fe_3O_4@C8	296	This work
Fe_3O_4 Bare NPs	275	This work
Peach gum	298	[158]
Graphene	153	[159]
Natural bentonite	300	[160]
Fe_3O_4@Carbon	35	[161]
Magnetic Fe_3O_4@Activated carbon nanocomposite	321	[162]
Aminoguanidine coated magnetic Fe_3O_4 NPs	246	[163]

Table 3.3 above shows the comparison of the adsorption capacities of different adsorbents with the as-synthesized adsorbents. From literature as shown if the reference column of **Table 3.3** these magnetite-based adsorbents can be used as alternatives for removal of organic dyes (specifically MB) from contaminated water. It can also be seen that these mono-alkyl phosphate esters render a better affinity towards methylene blue dye via hydrophobic effect compared to activated carbon coated magnetite nanoparticles. The advantage of the as-prepared adsorbents being easily prepared from cheap precursors of Fe^{2+} and Fe^{3+}, and long chain alkyl alcohols can be used at least three times without a significant decrease in the adsorption capacity makes them more preferrable compared to the above mentioned adsorbents.

Chapter 4

Synthesis and Characterisation techniques

In this chapter will discuss the synthetic methods used to synthesize magnetite nanoparticles and amphiphile organic shells and the characterization techniques used.

4.1 Materials and reagents

Ferrous chloride tetrahydrate ($FeCl_2.4H_2O$), ferric chloride hexahydrate ($FeCl_3.6H_2O$), ammonium hydroxide (NH_4OH, 25% v/v), 1-octanol ($C_8H_{17}OH$), 1-dodecanol ($C_{12}H_{25}OH$), 1-hexadodecanol ($C_{16}H_{33}OH$), ethanol (EtOH), methanol (MeOH), toluene (C_7H_8), diethyl ether $O(CH_3)_2$, anhydrous sodium sulphate (Na_2SO_4), phosphorus oxychloride ($POCl_3$) and methylene blue were purchased from Merck (Germany). All the chemical reagents used in this project were of analytical grade.

4.2 Synthesis of materials

4.2.1 Synthesis of Fe_3O_4 Nanoparticles

Synthesis of Fe_3O_4 nanoparticles was done by applying a conventional co-precipitation method that has been previously published with minor modifications [162,163]. 10.105 g of $FeCl_3{\cdot}6H_2O$ and 5.026 g of $FeCl_2{\cdot}4H_2O$ in a ratio of Fe^{3+}**:** Fe^{2+} is 2**:**1, were dissolved in 200 mL of deionized water under an argon atmosphere with vigorous stirring (1000 rpm) at 80 ^oC. Then, 40 mL of ammonia solution (25% v/v) was added to the mixture slowly. The colour of the solution changed from orange to black. The mixture was stirred for further 2 hours under the same conditions before it was cooled down to room temperature. The black Fe_3O_4 nanoparticles were separated from the supernatant by applying an external magnet (magnetic decantation) and washed with deionized water to a final pH of 9. The as-synthesized Fe_3O_4 NPs were dried in a vacuum oven overnight at 60 ^oC and then grinded into a fine powder using a pestle and mortar before characterization and application.

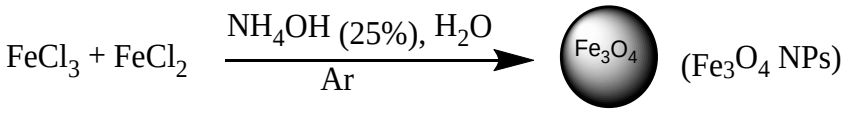

Figure 4.1: Reaction scheme for the synthesis of magnetite nanoparticles.

4.2.2 General synthesis of the mono-alkyl phosphate esters.

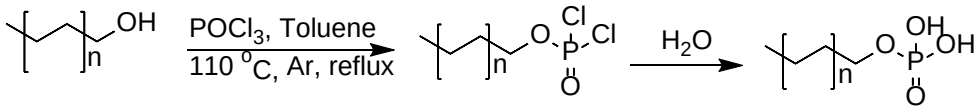

Figure 4.2: Reaction scheme for the synthesis of mono-alkyl phosphates, where n = 3,5,7.

4.2.3 Synthesis of octyl dihydrogen phosphate ester and dodecyl dihydrogen phosphate ester

The synthetic procedure for octyl dihydrogen phosphate and dodecyl dihydrogen phosphate was modified from a synthetic procedure reported for the synthesis of (1,6-bis[(dihydroxyphosphinyl)oxy]hexane) and similar compounds [124]. Under an argon atmosphere, 120 mL of toluene was mixed with 24 and 19 mL of phosphorus oxychloride for the synthesis of octyl dihydrogen phosphate and dodecyl dihydrogen phosphate respectively. Octanol (8 mL, 6.562 g, 50 mmol) and dodecanol (lauryl alcohol) (11 mL, 9.317 g, 50 mmol) were slowly added to toluene/ phosphorus oxychloride mixture respectively under reflux at 110 ^{o}C, stirring at 500 rpm for 5 and 6 hours. After stirring was done, the solution was concentrated with a rotary evaporator and the residue was co-evaporated twice with 150 mL of toluene to remove all the unreacted phosphorus oxychloride molecules. During the hydrolysis step, 250 mL of cold (0-5 ^{O}C) deionized water was slowly added since the reaction is exothermic. A white precipitate formed during the hydrolysis step. The mixture was left to stir for 2 hours at 90 ^{O}C. To the mixture, 200 mL of diethyl ether was added, and the organic layer was extracted with diethyl ether. The organic layer was dried in anhydrous sodium sulphate before it was concentrated on a rotary evaporator. The viscous

residue was co-evaporated three times with 150 mL of ethanol on a rotary evaporator to remove HCl that might have formed during the synthetic process. The residue was then crystalized in methanol/ ethyl acetate (1/4) (v/v) and the solution was left overnight in a fume hood at room temperature. The formed white amorphous solid was filtered, washed with diethyl ether, and dried in a vacuum pump, and a 71% yield was obtained with a 62 ^{o}C melting point (literature 85% yield, 39–45 ^{o}C). Octyl dihydrogen phosphate ester formed an oil, it was purified by vacuum distillation, 60% percentage yield.

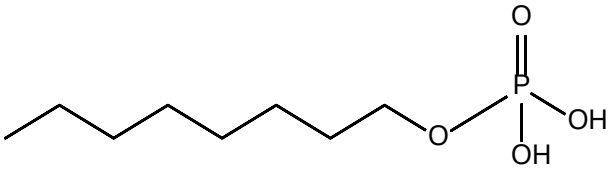

Compound 1 ($C_8H_{19}OP$): m/z = 209.2 $[M-H]^-$. **^{1}H NMR** (400 MHz, Acetone-d_6): ɞ: 10.82 (s, 2H, PO(**OH**)$_2$), 3.99 (q, *J* = 6.7 Hz, 2H, PO**CH$_2$**), 1.70 – 1.61 (m, 2H, POCH$_2$**CH$_2$**), 1.45- 1.21 (m, 10H, -(**CH$_2$**)$_5$-), 0.88 (t, *J* = 6.9 Hz, 3H, -**CH$_3$**). **^{13}C NMR** (101 MHz, Acetone-d_6) ɞ : 67.49 (d, *J* = 5.5 Hz, C8), 32.59 (C6), 31.07 (d, *J* = 7.0 Hz, C7), 30.01 (C5), 29.94 (C4), 26.28 (C3), 23.34 (C2), 14.38 (C1). **^{31}P NMR** (162 MHz, Acetone-d_6): ɞ : -1.15 (OPO(OH)$_2$).

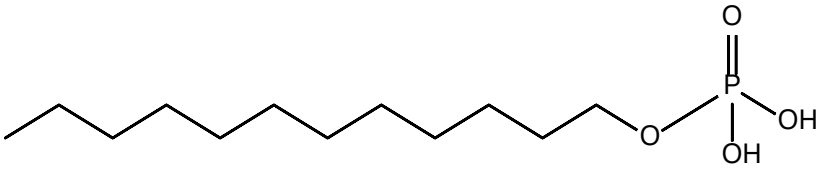

Compound 2 ($C_{12}H_{27}O_4P$): mp 62 ^{o}C. m/z = 265.6 $[M-H]^-$. **^{1}H NMR** (400 MHz, Acetone-d_6) δ: 9.52 (s, 2H, PO(**OH**)$_2$), 4.01 (q, *J* = 6.7 Hz, 2H, PO**CH$_2$**), 1.73 – 1.64 (m, 2H, POCH$_2$**CH$_2$**), 1.46 – 1.26 (m, 18H, -(**CH$_2$**)$_9$-), 0.89 (t, *J* = 6.8 Hz, 3H, **CH$_3$**). **^{13}C NMR** (101 MHz, Acetone-d_6) δ: 66.57 (d, *J* = 5.5 Hz, C12), 31.76 (C10), 30.16 (d, *J* = 7.2 Hz, C11), 29.56 – 29.41 (m, C4-C7), 29.02 (m, C8 & C9), 25.37 (C3), 22.45 (C2), 13.47 (C1). **^{31}P NMR** (162 MHz, Acetone-d6) δ:1.11 (O**P**O(OH)$_2$).

4.2.4 Synthesis of hexadecyl dihydrogen phosphate

The method used for the synthesis of hexadecyl dihydrogen phosphate ($C_{16}H_{35}O_4P$) was modified from a reported procedure [164]. In a dry round bottom flask under an argon atmosphere at 50 ^{O}C, stirring at 300 rpm, 12.966 g of hexadecanol was dissolved in 20 mL of phosphorus oxychloride ($POCl_3$). The mixture was left to stir at the same conditions for 1.5 hours. Then, 250 mL of cold (0–5 ^{o}C) deionized water was added slowly to the mixture, and it was heated under reflux for 7 hours to ensure complete hydrolysis. During the hydrolysis process, a white solid formed. The formed white organic solid was dissolved in diethyl ether. Which was then extracted using diethyl ether and dried in anhydrous sodium sulphate before it was concentrated in a rotary evaporator. The white solid compound was recrystallized in hexane forming an amorphous white solid with a 76% percentage yield and a melting point of 121–123 ^{o}C.

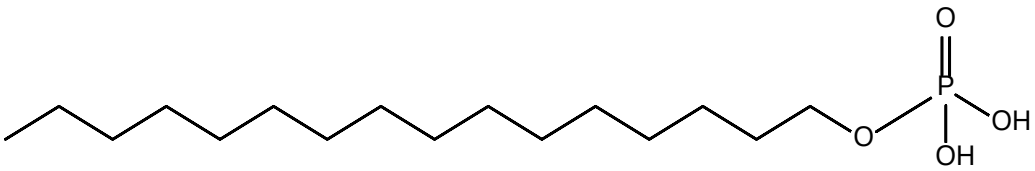

Compound 3 ($C_{16}H_{35}O_4P$): mp 121–123 ^{o}C. m/z = 321.6 $[M\text{-}H]^-$. **^{1}H NMR** (400 MHz, Acetone-d_6) **δ**: 4.00 (q, *J* = 6.7 Hz, 2H, PO**CH_2**), 1.68 (p, *J* = 6.6 Hz, 2H, $POCH_2$**CH_2**), 1.44 – 1.26 (m, 26H, -(**CH_2**)$_{13}$-), 0.89 (t, *J* = 6.7 Hz, 3H, **CH_3**). **^{13}C NMR** (101 MHz, Acetone-d_6) δ: 66.46 (d, *J* = 5.5 Hz, C16), 31.75 (C14), 30.18 (d, *J* = 7.2 Hz, C15), 29.50 (q, *J* = 4.4 Hz, C11 – C13), 29.33 (C9 & C10), 29.14 (C6 – C8), 28.94 (C5), 28.75 (C4), 25.38 (C3), 22.44 (C2), 13.46 (C1). **^{31}P NMR** (162 MHz, Acetone-d_6): ɣ = 1.11 (O**P**O(OH)$_2$).

4.3 Coating of magnetic Fe_3O_4 NPs with surfactants

The procedure used to coat the Fe_3O_4 NPs was modified from already published procedures [129,165]. 50 mM solutions of the different surfactants (differing in alkyl chain length) were prepared. These solutions were prepared by weighing 10.00, 10.03, and 9.991 mg for C8, C12, and C16 phosphate esters, respectively, and dissolved in 200 mL of methanol. Each surfactant solution was mixed with 0.1 g of the as-synthesized Fe_3O_4 (3mg/mL) NPs that were first dispersed in 35 mL of methanol. The mixture was placed in an ultrasonic bath at 25 ^{o}C for an hour. The functionalized iron oxide nanoparticles were collected by applying an external magnet and the

supernatant was discarded. The excess functionalizing surfactant molecules were removed by dispersing the coated nanoparticles in methanol and the coated nanoparticles were obtained by applying an external magnet. This washing process was repeated three times to ensure the complete removal of the excess functionalization molecules. Then the functionalized iron oxide nanoparticles were dried at 60 ^{O}C in a vacuum oven overnight before characterization and applying for removal of organic dyes from water matrixes, respectively.

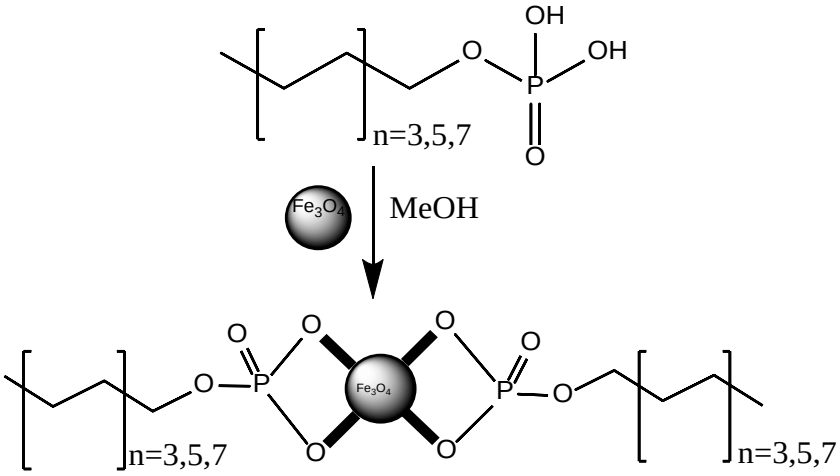

Figure 4.3: Reaction scheme for coating of magnetite nanoparticles with alkyl mono-phosphate esters of different chains.

4.4 Adsorption studies

Different adsorption parameters including pH value, initial dye concentration, the dosage of adsorbent, temperature, and contact time of the adsorbent with the dye solution were evaluated for the removal of methylene blue from spiked water samples with methylene blue.

Calibration curve: A stock solution of 1000 ppm of the dye (methylene blue) was prepared by dissolving 100.0 mg of an analytical grade dye (methylene blue) in a 100 ml volumetric flask using distilled water and five standard solutions (100-500 ppm) were prepared from this by pipetting right amounts of the stock to a 10 mL volumetric flask and fill to the mark using distilled water. UV-Vis spectrophotometer was used to determine the absorbances (intensities) of the standard solutions and to plot the

absorbances vs concentration curve to obtain a calibration curve. The equation of the linear regression ($y = 0.3463x + 9.1135$, $R^2 = 0.9997$) shows a good linear relationship between the intensities and corresponding concentrations, this equation was used to determine concentrations of the unknown dye solutions after adsorption studies.

To study the effect of pH during the adsorption studies for dye removal, 300 ppm solution of each dye solution was prepared from the stock solution by pipetting 3 mL to a 10 mL volumetric flask and filled to the mark using distilled water and the pH (3–10) was adjusted using 0.1 M NaOH and 0.1 M HCl. 10 mL of the dye solution (300 ppm) was added in 9 different Erlenmeyer flasks with pH values varies from 3 to 10. The pH measurements were taken using a pH meter. To each flask 10 mg of the adsorbent ($Fe_3O_4@PO_4C_{16}H_{33}$) was added and shaken for 30 minutes (ultra-sonicator) after adsorption the magnetic nanoparticles were separated by an external magnetic bar and the supernatant was analyzed using UV-Vis spectrophotometer to determine the concentration of the dye adsorbed by the adsorbent. A graph of removal % vs pH was plotted as shown in **Figure 3.10** in **Chapter 3** to determine at what pH value most dye concentration was adsorbed.

To study the effect of the adsorbent dosage (**Figure 3.11 in Chapter 3**) on the dye removal, different amounts of the adsorbent's (Fe_3O_4@Surfactant) dosages (10–50 mg) were added to 10 mL dye solutions with 300 ppm concentration at pH 10. Contact time influence was investigated by preparing ten dye solutions of 500 ppm and 10 mg of the adsorbent was added and sonicated for (10, 20, 30 ,40, 50, 60, 90, 120, 240, and 480 min). A graph of removal % vs time (min) was plotted as shown in **Figure 3.13** in **Chapter 3**.

The reusability studies of the adsorbent were investigated by preparing a 500 ppm dye solution in a 10 mL volumetric flask and transferred it to a weighing vail, 10 mg of the adsorbent was added and sonicated for 30 minutes. The adsorbent was removed by magnetic decantation, the supernatant was analysed using UV/Vis spectroscopy and the adsorbed dye on the surface of the adsorbent was removed by sonicating it in methanol (20 mL, x 4) till all the dye was removed. These nanoparticles were then dried in a vacuum oven at 60 ^oC overnight and then grinded into a fine powder using a pestle and mortar before they were reused. This process was repeated four more

times. A graph removal % vs reusability cycle was plotted as shown in **Figure 3.15** in **Chapter 3.**

The effect of initial dye concentration was investigated by preparing five solutions (100–500 ppm) where the pH of these solutions was adjusted to 10, and 10 mg of the adsorbent was added to each dye solution and sonicated for 30 minutes at 25 ^{o}C. From these results, the data were fit to adsorption isotherms (Langmuir and Freundlich) ad was seen that these adsorption studies follow Langmuir isotherms.

For all the adsorption factors the studies were done for each adsorbent: bare magnetite nanoparticles and nanoparticles coated with each mono-phosphate ester (n = 3, 5,7). These magnetic adsorbents were removed by magnetic decantation and UV/Vis spectroscopy to determine the concentration of dye removed. Before UV/Vis spectroscopy the dye solutions were diluted 100 times to give accurate absorbance values of less than 1.5 for the reliable instrument measurement.

To determine methylene blue removal percentage using the surfactant-covered magnetite nanoparticles, the following formula was used:

$$\% \text{ removal} = \frac{C_0 - C_f}{C_0} x\ 100\% \qquad \text{(eq. 4.1)}$$

Where C_0 is the initial dye concentration (ppm) and C_f is the dye concentration (ppm) at equilibrium.

To determine the adsorption capacity of the adsorbent, the mass balance equation (**eq. 4.2**) was used.

$$q = \frac{(C_o - C_f)V}{W} \qquad \text{(eq. 4.2)}$$

Where C_0 is the initial dye concentration (mg/L), C_f is the final dye concentration (mg/L) at equilibrium, V is the volume of methylene blue solution (L), W is the amount of the adsorbent (g), and q is the adsorption capacity (mg/g) of the adsorbent.

The obtained data were fitted to the Langmuir and Freundlich isotherms and their parameters were calculated and shown in **Table 3.1** in **Chapter 3**. The adsorption isotherms in **Chapter 3 (Figure 3.16)** were plotted using all 5 points.

4.5 Characterization techniques

4.5.1 Microscopic characterization

Microscopic techniques such as transmission electron microscopy (TEM) and scanning electron microscopy (SEM) images objects that cannot be seen by the naked eye, using a specialized microscope. Conventional microscopy has three main parts namely optical, reflection, and scanning probe microscopy. In electron microscopes, micrographs are produced from the gathering of the scattered radiation from diffraction, reflection, or refraction of electromagnetic radiation associated with the analyzed sample. High-resolution TEM and SEM produce microstructures with high resolution compared to light microscopes. These high-resolution images are produced because of the shorter wavelength in electron microscopes, they have a wavelength that is ten thousand times shorter than visible light. This shorter wavelength of electron microscopes makes it possible to see objects with at least 0.1 nm in radius [165].

4.5.1.1 Transmission Electron Microscopy (TEM)

TEM enables researchers to know the material's inner structure such as crystal structure and morphology [166,167].

TEM was performed on a Philips (FEI) CM100 instrument coupled with a digital camera (Mega-view III) at the Centre of Microscopy, University of the Free State. The images were analysed using Soft Imaging System Analysis software. Metal particle size determination was also performed on the above-mentioned software.

4.5.1.2 Scanning Electron Microscope (SEM)

SEM offers surface information of the sample such as morphology and it can be coupled to instruments such as energy dispersive x-ray for the chemical composition of the sample [166].

The JEOL JSM-6610 Scanning Electron Microscope was used to perform the microscopic analysis with the image shown below.

Figure 4.4: JEOL JSM-6610 Scanning electron microscope.

4.5.2 Spectroscopic characterization

Spectroscopic techniques measures and interprets the electromagnetic spectra produced from the interaction of electromagnetic radiation and matter measured as a function of the wavelength or frequency of the radiation.

4.5.2.1 Ultraviolet-Visible spectroscopy (UV-Vis)

UV-Vis spectroscopy measures the amount of ultraviolet or visible light that is absorbed or transmitted through a sample at a certain wavelength, compared to the blank sample [168].

UV/Vis spectra were recorded for dilute solutions i.e. diluted using distilled water, in quarts cuvettes on a Varian Cary 50 UV/Vis spectrophotometer.

Figure 4.5: Varian Cary 50 UV/Vis spectrophotometer.

4.5.2.2. Nuclear Magnetic Resonance (NMR) Spectroscope

NMR spectrometer can be used to get information about the molecular structure of the sample at the atomic level and can also be used to study conformational and configurational alterations of the sample [169].

^{1}H, ^{13}C, and ^{31}P Nuclear Magnetic Resonance Spectra were recorded on a Bruker Advance DPX 400 MHz spectrometer. The spectra were analysed with TopSpin v4.1.4 2021 Bruker BioSpin GmbH software. The deuterated solvent used for the surfactants is acetone.

Figure 4.6: 400 MHz Bruker Advance DPX NMR spectrometer.

4.5.2.3. Fourier-Transform Infrared (FTIR)

FTIR spectroscopy helps to determine to obtain an infrared spectrum of absorption or emission of a solid, liquid, or gas. From an infrared spectrum, one can get information about the different functional groups present in the sample [170].

Spectra were med on a Bruker Tensor 27 IR spectrometer, fitted with a Pike Miracle single bounce diamond ATR crystal, and analysed with OPUS v1.1 and Origin 2021 software. Alternatively, Thermo Scientific Nicolet iS50 ATR Infrared Spectrometer with OMNIC v9.2.86 software was used.

Figure 4.7: Bruker Tensor 27 FT-IR spectrometer.

4.5.2.4 Powder X-ray Diffraction (PXRD)

PXRD gives information about the crystal structure of the sample and its atomic spacing resulting from the constructive interference of monochromatic X-rays of a crystalline sample. Information about the crystal structure of the sample is obtained when the incident rays interact with the sample and meet the conditions of Bragg's Law: nλ = $2d\sin\theta$ where n is an integer, λ is the wavelength (nm) of the X-rays, d is the interplanar spacing, and θ is the diffraction angle [171].

The PXRD analysis of the as-synthesized nanoparticles was performed on a Bruker AXS D8 Advance. A Cu-Kα radiation tube with LynxEye detector was used for the experiment, with 2θ between 5° and 80° and an increment of $2\theta = 0.0103°$.

Figure 4.8: Bruker AXS D8 Advance PXRD spectrometer.

4.5.2.5 Mass Spectrometry (MS)

Mass spectrometry measures the mass-to-charge ratios of fragments (ions). This technique is used for the chemical elucidation of the compound. In general, a sample is bombarded with a beam of electrons to form ions. The sample breaks down into positively charged fragments and these fragments are analysed according to their mass-to-charge ratios. Results are obtained as a plot of the signal intensity of the detected fragments versus the mass-to-charge ratios. The mass-to-charge ratios of the molecules or atoms in the sample can then be matched with the known masses of the molecules in the sample according to its characteristic fragmentation pattern [172].

Several different mass spectrometers with ESI ionization technique operated both in positive and negative ionization mode were used to characterize the synthesized phosphate esters.

4.6 Other characterization techniques

4.6.1 Energy Dispersive X-ray analysis (EDS)

Elemental analysis of a sample can be performed using an energy-dispersive spectrometer. During this analysis technique, a core-shell electron is ejected when the material is excited using an energy source such as a beam of electrons creating a vacant space. Then an electron with higher energy from the outer shell fills the vacant space. The difference in energy of the two electrons is measured as an X-ray spectrum which is unique for each atom. The spectrum peaks can be used to identify the elements present in the sample and their signal intensities give information about the concentration of those elements [173].

4.6.2 Thermogravimetric analysis (TGA)

TGA investigates the thermal stability of the sample. It gives a thermogram as a function of weight loss percentage vs temperature. As the heating temperature increases the sample loses weight till it becomes stable, calling that point where the sample(material) is stable. Results obtained from this technique can also be used to evaluate the number of molecules that a nanoparticle can be coated with [174].

For Thermo-Gravimetric Analyses, the TA-TGA 5000 Discovery Series instrument was used under a nitrogen atmosphere. The TGA thermograms were analysed by TA-TRIOS v2.1.2.60 software. Approximately 5 mg of the sample was heated to 700 ^{o}C at a heating rate of 10 ^{o}C/min, during a typical TGA measurement.

Figure 4.9: TA-TGA 5000 Discovery Series Thermal Gravimetric Analyser.

Chapter 5

Conclusion and Recommendations

5.1 Conclusion

All the objectives for this project as stated in **Chapter 1 (Section 1.4)** were achieved, based on the obtained results (**Chapter 3**) the following conclusion was drawn. All three mono-alkyl phosphate esters ($C_8H_{17}O_4P$ (**C16**), $C_{12}H_{27}O_4P$ (**C12**), and $C_{16}H_{35}O_4P$ (**C8**)) were prepared successfully from alkyl alcohol chains using phosphorus oxychloride as the phosphorylating agent. **C16** and **C12** were obtained as amorphous white solids whereas **C8** was a yellowish oil. They were characterized using mass spectrometry (**C8** and **C12**), NMR (^{1}H, ^{13}C, and ^{31}P), and FTIR (for **C12** and **C16**) spectroscopy which confirmed their successful synthesis. Quite high yields were obtained for these phosphate esters: 60%, 76%, and 85% for C8, C16, and C12 respectively.

Black magnetic iron oxide nanoparticles were successfully synthesized using the co-precipitation method and were characterized using FTIR, EDS, PXRD, SEM, and TEM analysis. These characterization techniques confirmed the formation of the magnetite nanoparticles. Presence of the vibrational band at 586 nm for Fe–O bond of iron oxide nanoparticles confirmed the successful formation of iron oxide nanoparticles. Characteristic peaks for magnetite nanoparticles from PRXD spectra were obtained with particle average size diameter of 12–16 nm. They were functionalized using the prepared mono-alkyl phosphate esters of different alkyl chain lengths. Successful functionalization of the magnetite nanoparticles was confirmed by the presence of P–O, P=O, C–C, and C–H bonds on the surface of the magnetite nanoparticles, these vibrational bands were seen from the FTIR spectra of the functionalized magnetite nanoparticles. Also, the presence of phosphorus (P) and carbon (C) on the EDS results and an increase in average particle diameter sizes seen from TEM and SEM micrographs (before and after functionalization) confirmed the successful coating of the as-synthesized magnetite nanoparticles.

Functionalized magnetite nanoparticles were tested for the removal of organic dyes from dye-spiked water samples. The mono-alkyl phosphate esters rendered affinity for the removal of the organic dye (MB). To test the adsorption efficiency of these

adsorbents' adsorption factors such as sorption pH, sorbent amount, initial dye concentration, temperature, and contact time were investigated. These factors seemed to play a big role in the adsorption of MB by these as-synthesized adsorbents. Better dye percentage removal (%) was observed at pH = 10 and an adsorbent amount of 10 mg at 60 ^{o}C.

Obtained experimental data were fitted to Langmuir and Freundlich isotherm models. Data fitted well the Langmuir isotherm model with a maximum adsorption monolayer of 317, 301, 265, and 241 mg/g with R^2 values of 0.978, 0.975, 0.982, and 0.978 for **C16**, **C12**, **C8**, and bare magnetite NPs respectively. Functionalizing magnetite nanoparticles with esters showed better adsorption efficiency for the removal of MB. Longer alkyl chain length ($Fe_3O_4@C_{16}$) showed better dye percentage removal of 81%. These nano-adsorbents can be reused at least 3 times without much significant decrease in the adsorption capacity. Experimental data were also fitted on the pseudo-first order and pseudo-second-order kinetic models and found to follow the pseudo-second-order kinetic model with equilibrium adsorption capacity relates well with the obtained experimental adsorption capacity.

With these results, one can say that mono-alkyl phosphate ester functionalized magnetite nanoparticles show better adsorption capacities for the removal of organic dyes (MB dye) from wastewater, especially mono-hexadecyl phosphate ester covered magnetite nanoparticles. These nanoparticles are synthesized using easy, cheaper, non-toxic, green chemistry methods with the advantage of easy separation by using an external magnet and they can be recycled at least three times. This project aimed to find a better cheaper method for the removal of the model MB dye from wastewater, these adsorbents show promising results with 81% percentage removal and can be used in industry for wastewater treatment as an alternative method.

5.2 Future recommendations

The results obtained from this project demonstrated that mono-alkyl phosphate functionalized magnetite NPs have the potential to be used as adsorbents for the removal of charged organic dyes in water. The testing of these functionalized nano-adsorbents with neutral dyes will be done next. We expect to see more promising

adsorption capacities because neutral molecules should be better absorbed by the lypophilic alkyl shells of the magnetite NPs.

Preparation of another type of organic shells is planned. The use of more guest specific coatings will be aimed at the preparation of NPs tailored for the removal of specific water pollutants.

A better understanding of the toxicity of the phosphate ester functionalized nanoparticles can also open another branch of research.

APPENDICES

^{1}H NMR (400 MHz, Acetone-d_6) δ: 10.82 (s, 2H, PO(**OH**)$_2$), 3.99 (q, J = 6.7 Hz, 2H, -O**CH**$_2$), 1.70 – 1.61 (m, 2H, -OCH$_2$**CH**$_2$), 1.45 – 1.21 (m, 10H, -(**CH**$_2$)$_n$-), 0.88 (t, J = 6.9 Hz, 3H, -**CH**$_3$).

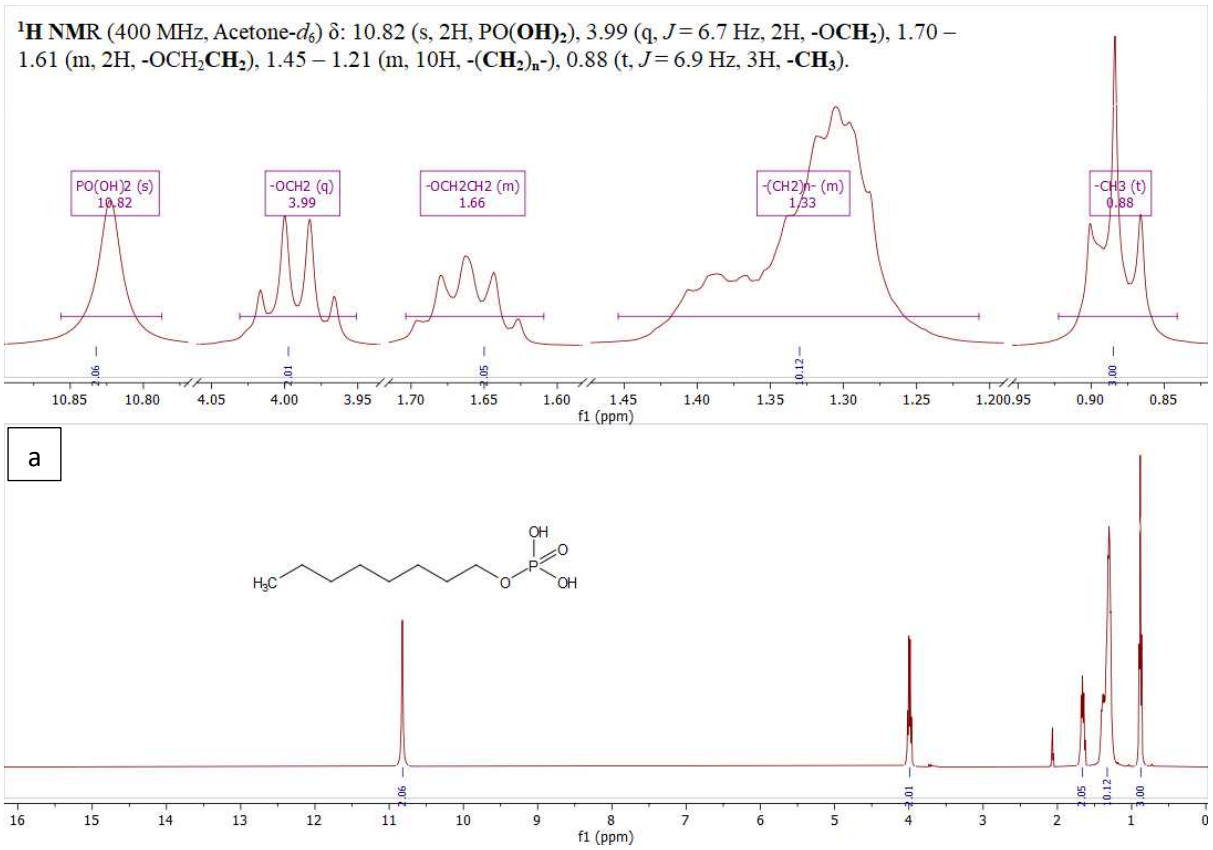

^{1}H NMR (400 MHz, Acetone-d_6) **δ:** 9.52 (s, 2H, PO(**OH**)$_2$), 4.01 (q, J = 6.7 Hz, 2H, -O**CH**$_2$), 1.73 – 1.64 (m, 2H, -OCH$_2$**CH**$_2$), 1.46 – 1.26 (m, 18H, -(**CH**$_2$)$_9$-), 0.89 (t, J = 6.8 Hz, 3H, -**CH**$_3$).

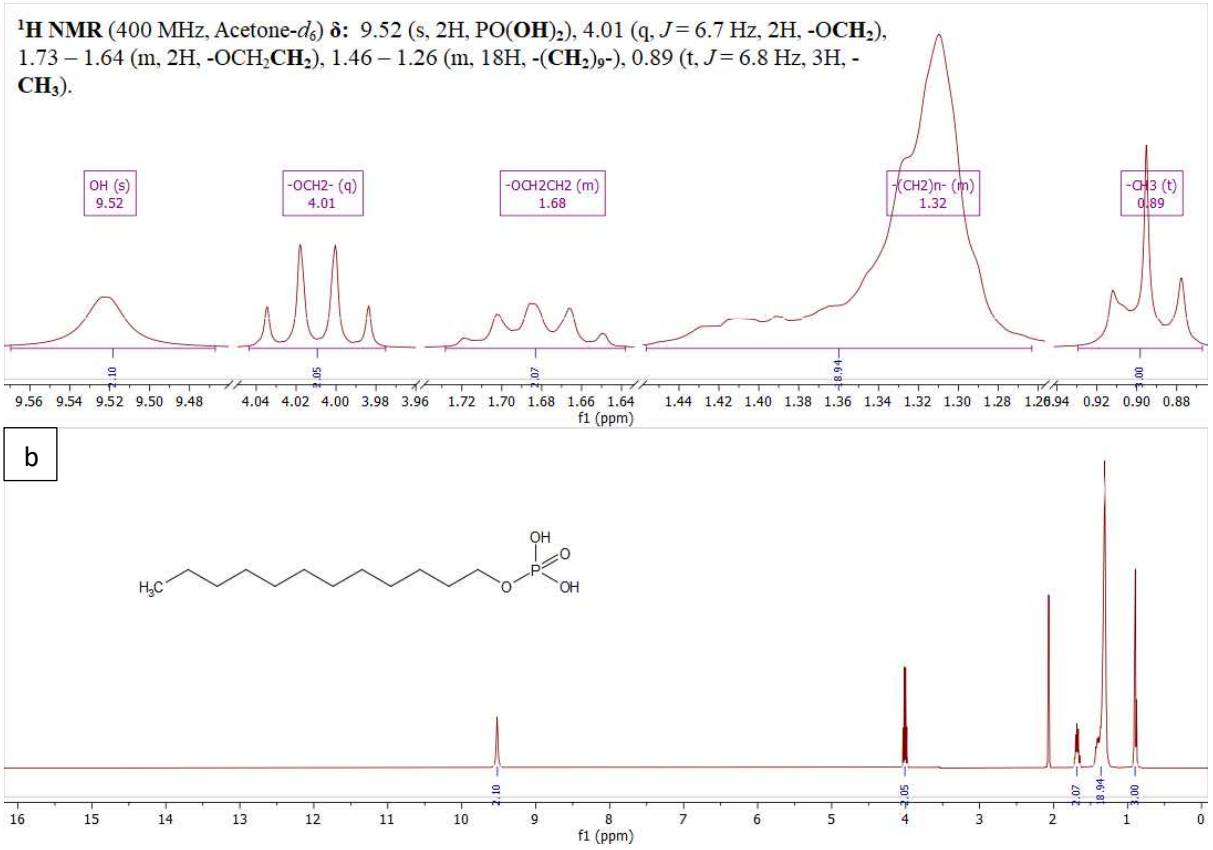

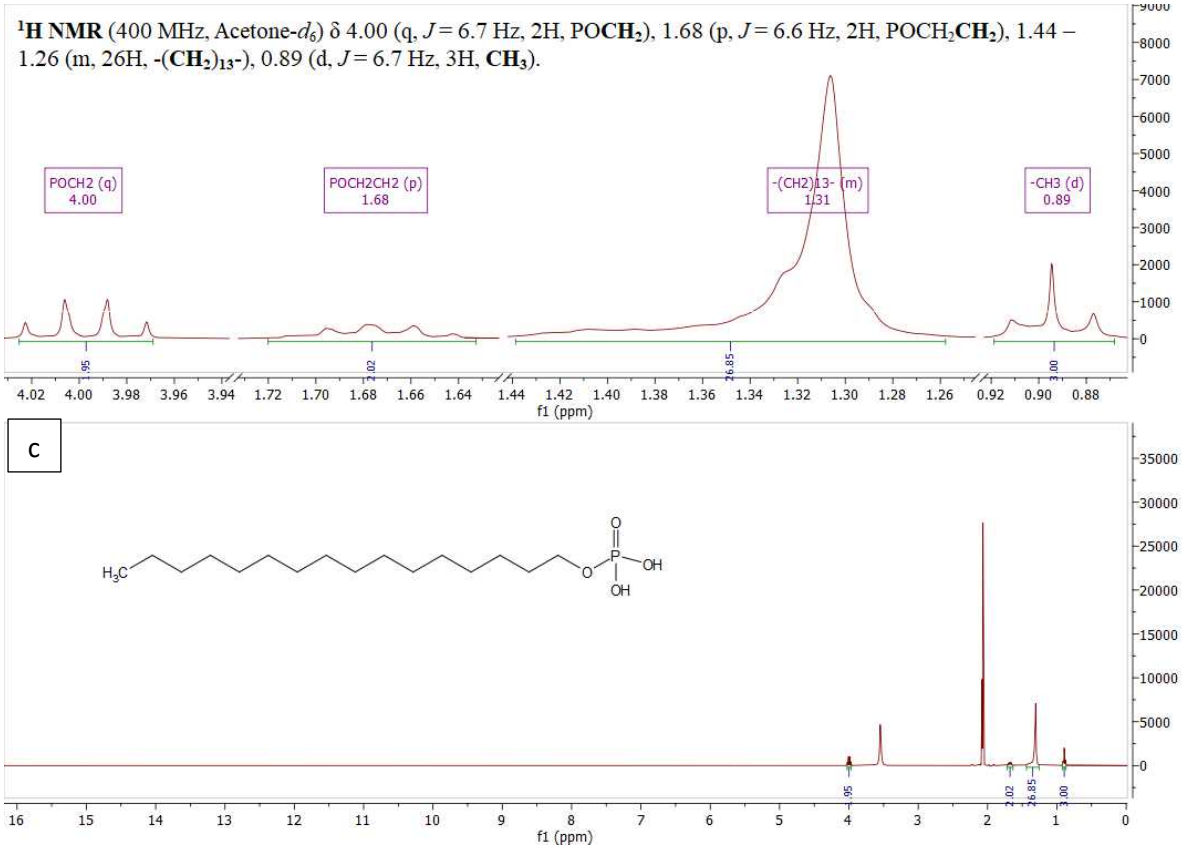

Figure 5: ^{1}H NMR spectra of (a) $C_8H_{17}O_4P$, (b) $C_{12}H_{27}O_4P$, and (c) $C_{16}H_{35}O_4P$.

^{13}C NMR (101 MHz, Acetone-d_6) δ 67.49 (d, J = 5.5 Hz, C8), 32.59 (C6), 31.07 (d, J = 7.0 Hz, C7), 30.01 (C5), 29.94 (C4), 26.28 (C3), 23.34 (C2), 14.38 (C1).

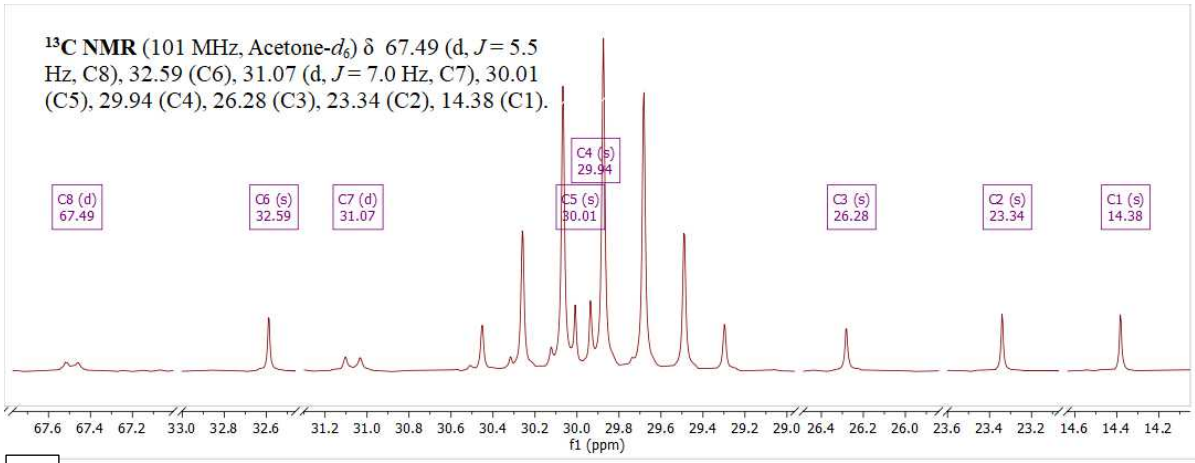

a

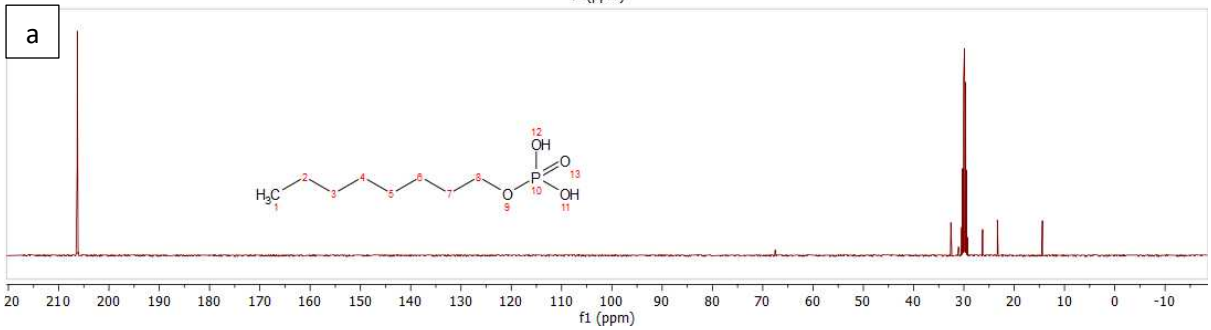

^{13}C NMR (101 MHz, Acetone-d_6) δ 66.57 (d, J = 5.5 Hz, C12), 31.76 (C10), 30.16 (d, J = 7.2 Hz, C11), 29.56 – 29.41 (m, C4-C7), 29.25 – 29.02 (m, C8&C9), 25.37(C3), 22.45 (C2), 13.47 (C1).

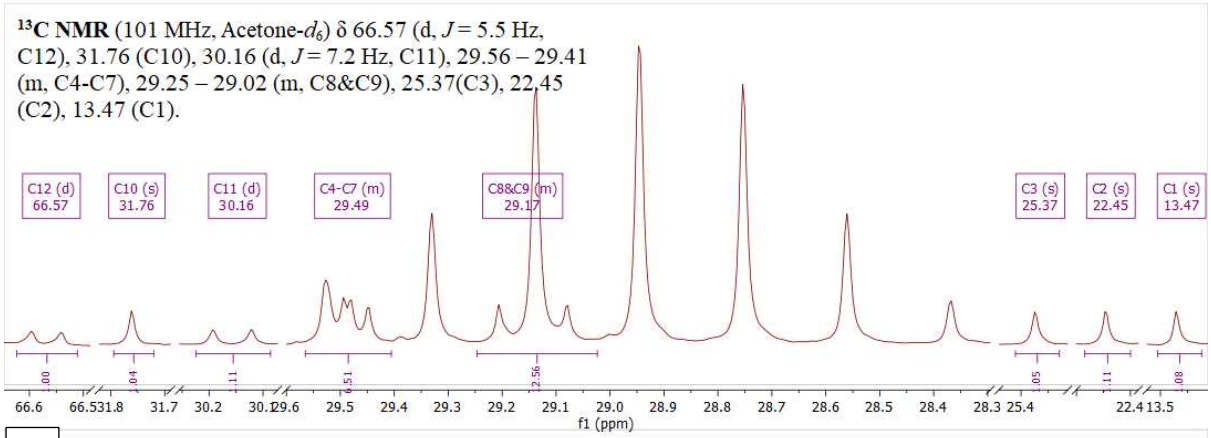

b

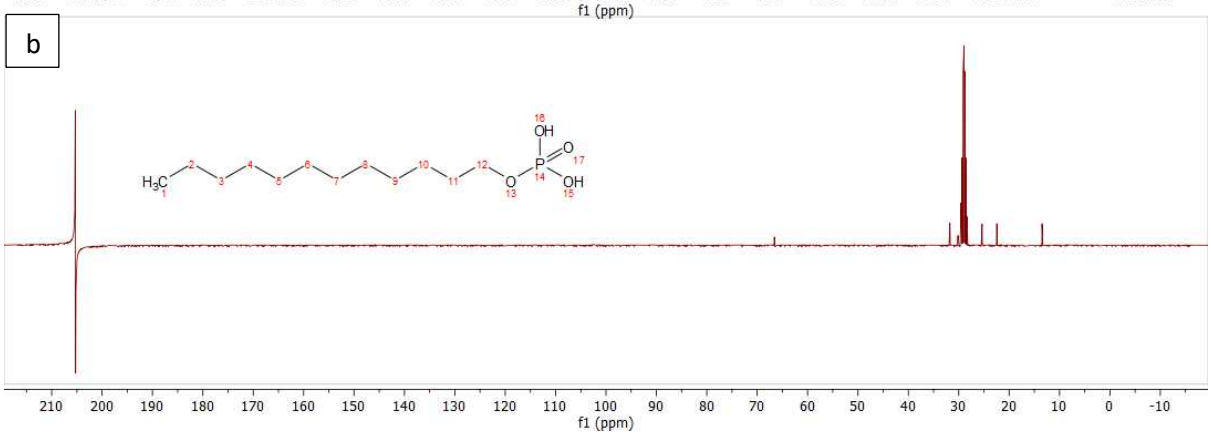

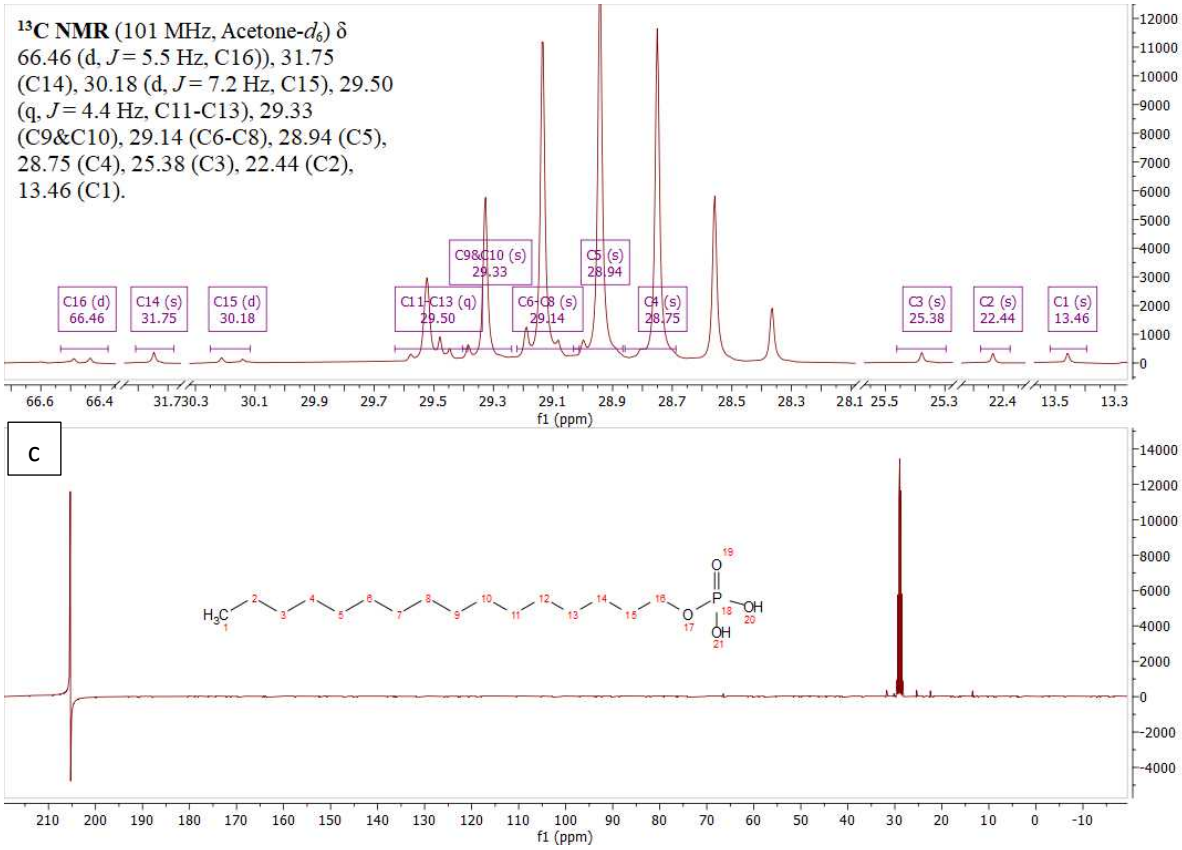

Figure 6: ^{13}C NMR spectra of (a) $C_8H_{17}O_4P$, (b) $C_{12}H_{27}O_4P$, and (c) $C_{16}H_{35}O_4P$.

^{31}P NMR (162 MHz, DMSO-d_6) δ -1.15 (OPO(OH)$_2$).

a

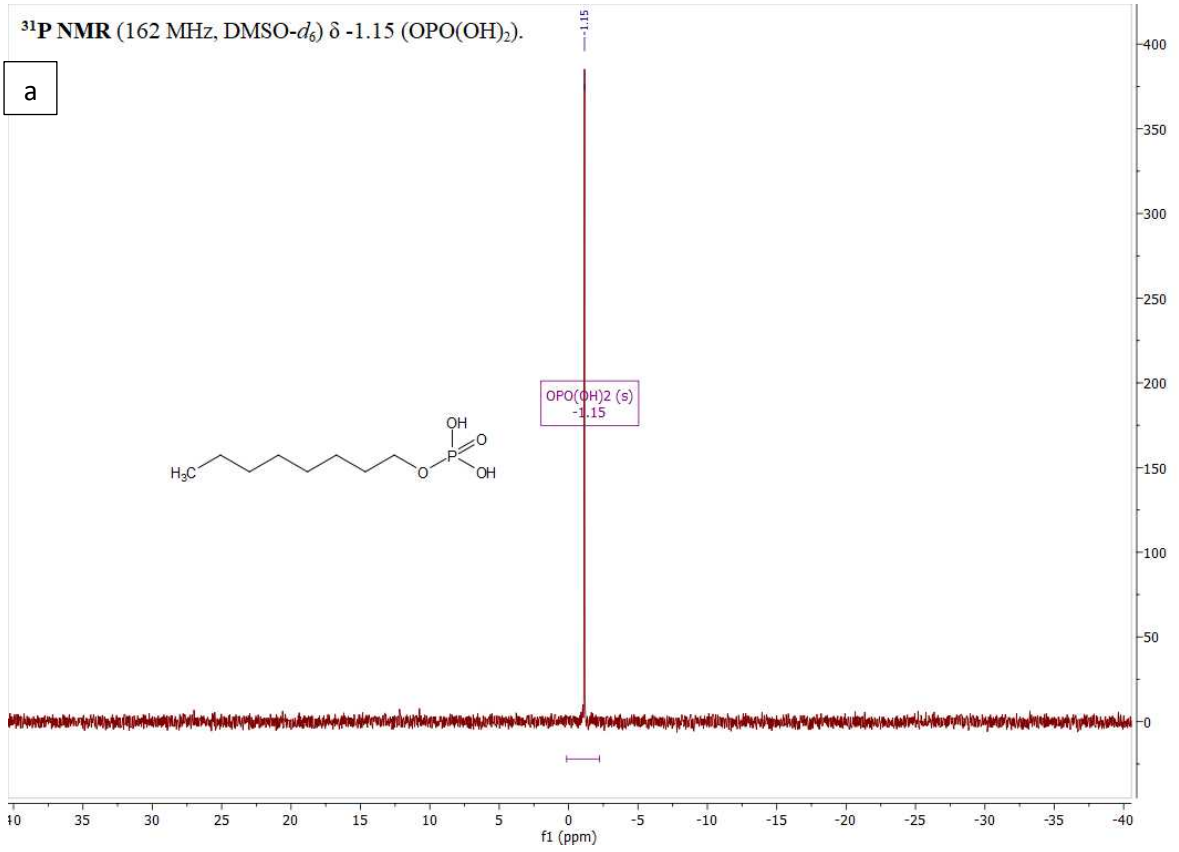

^{31}P NMR (162 MHz, Acetone-d_6) δ 1.11 (O**P**O(OH)$_2$).

b

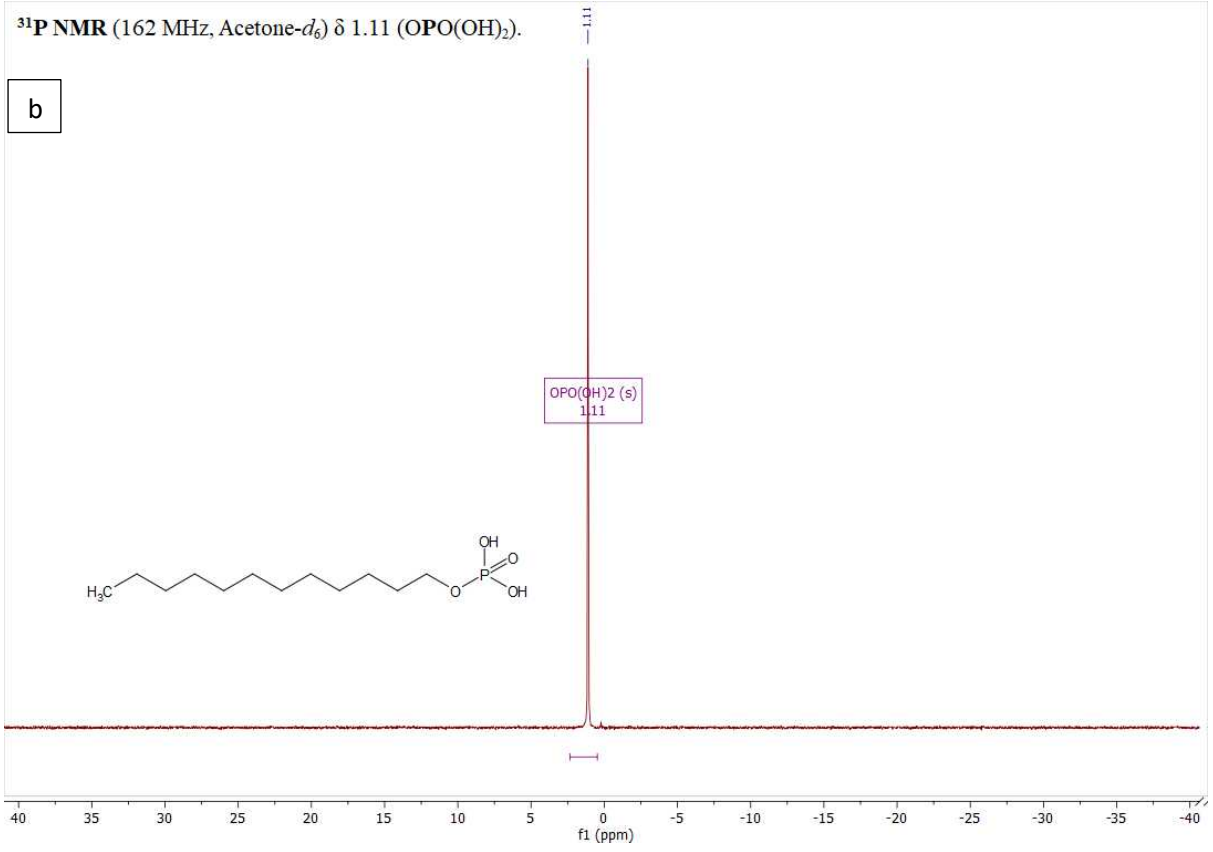

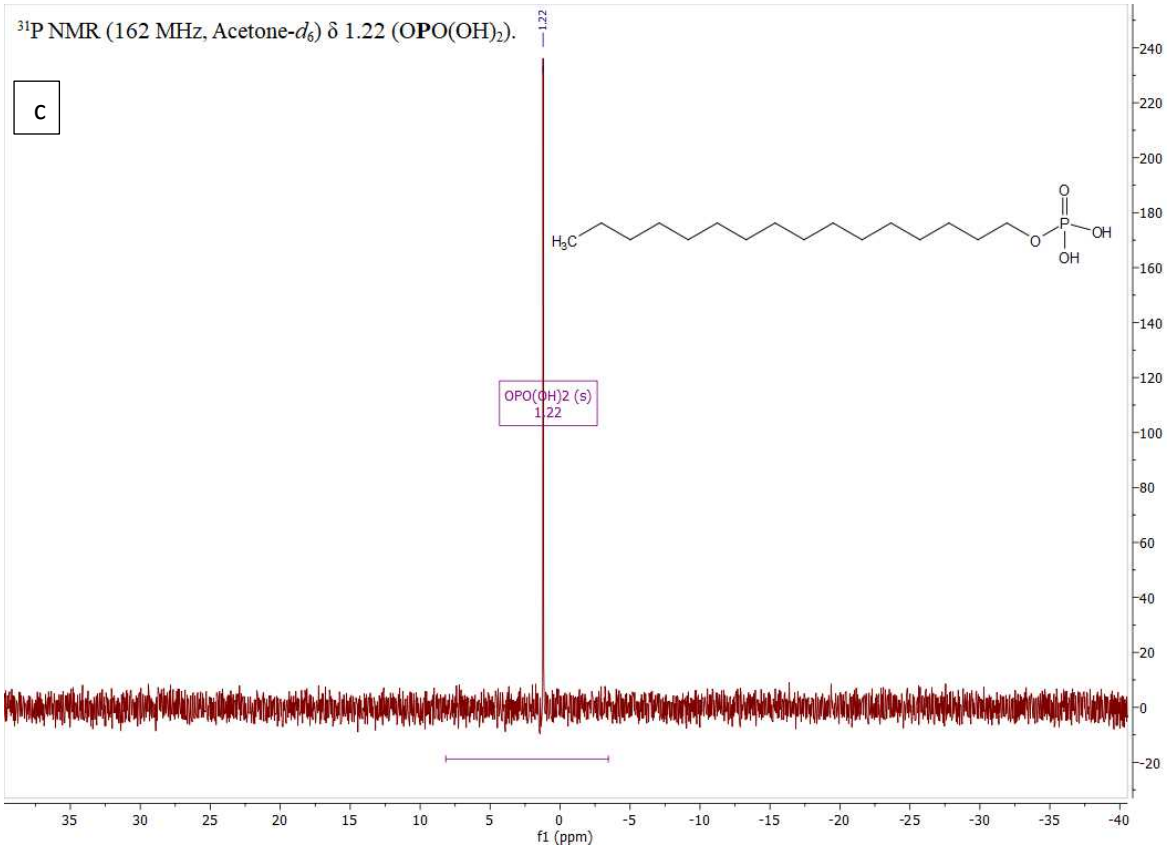

Figure 7: ^{31}P NMR spectra of (a) $C_8H_{17}O_4P$, (b) $C_{12}H_{27}O_4P$, and (c) $C_{16}H_{35}O_4P$.

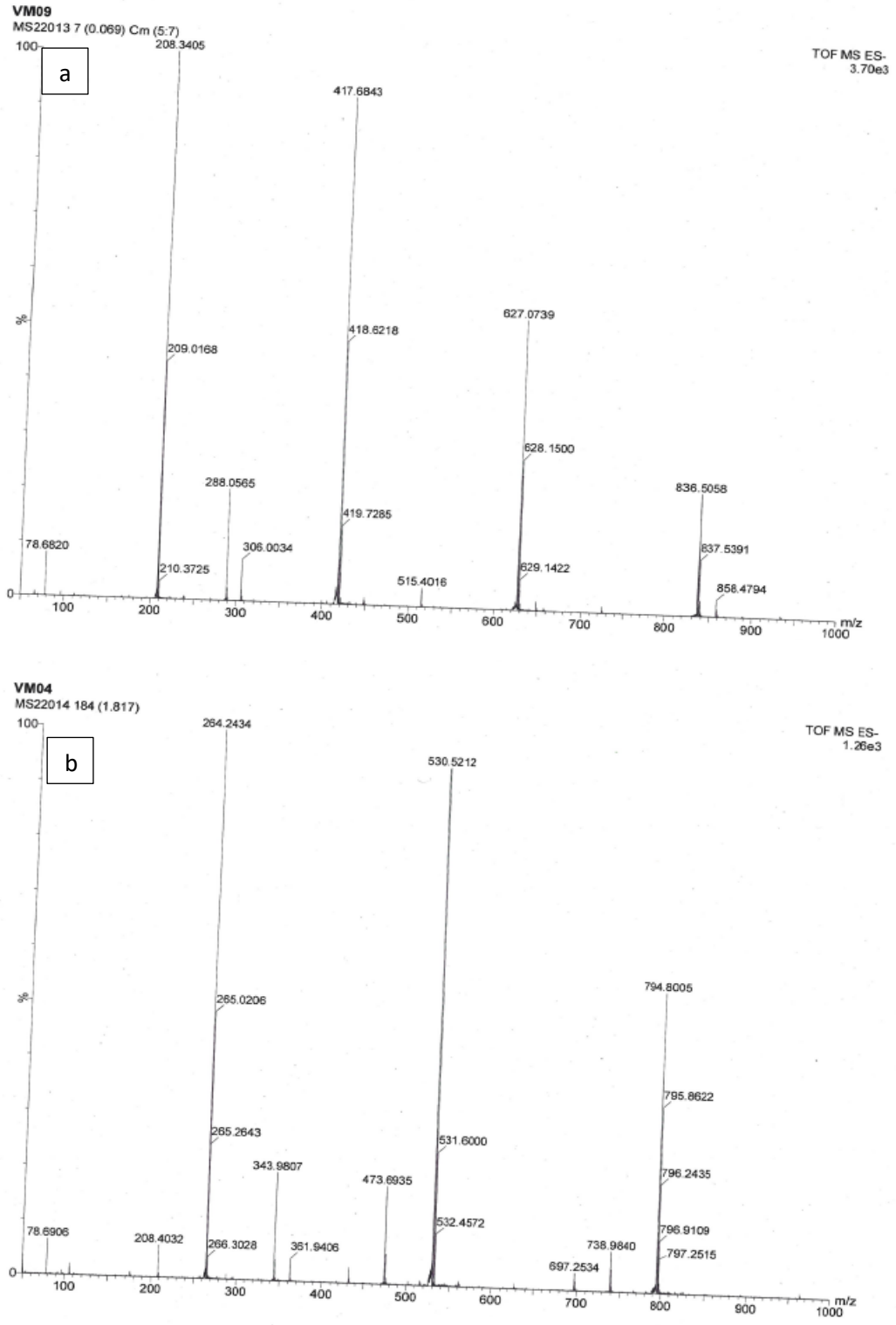

Figure 8: ESI-MS-(–) spectra of the synthesized mono-alkyl phosphate esters (a) C8, (b) C12. Note: in (a,b) peaks with higher molecular masses correspond due to the formation of dimeric and trimeric aggregates.

REFERENCES

1. Dimpe KM, Nyaba L, Magoda C, Ngila JC, Nomngongo PN. Synthesis, modification, characterization and application of AC@Fe_2O_3@MnO_2 composite for ultrasound assisted dispersive solid phase microextraction of refractory metals in environmental samples. Chem Eng J. 2017;308(19):169–76.

2. Dimpe KM, Ngila JC, Nomngongo PN. Application of waste tyre-based activated carbon for the removal of heavy metals in wastewater. Cogent Eng. 2017;4(1):3–11.

3. Fu F, Wang Q. Removal of heavy metal ions from wastewaters: A review. J Environ Manage. 2011;92(3):407–18.

4. Wang X, Fan X, Lin H, Fu H, Wang T, Zheng J, et al. An efficient Co-N-C oxygen reduction catalyst with highly dispersed Co sites derived from a ZnCo bimetallic zeolitic imidazolate framework. RSC Adv. 2016;6(44):37965–73.

5. Chan OS, Cheung WH, McKay G. Single and multicomponent acid dye adsorption equilibrium studies on tyre demineralised activated carbon. Chem Eng J. 2012;15(191):162–70.

6. Pai CW, Leong D, Chen CY, Wang GS. Occurrences of pharmaceuticals and personal care products in the drinking water of Taiwan and their removal in conventional water treatment processes. Chemosphere.2020;256(25):12700-2

7. Metcalfe CD. Contaminants of emerging concern in effluents from wastewater treatment plants in the Lake Simcoe watershed. Environ Sci Technol. 2014;16(4):1–8.

8. Rivera-Utrilla J, Sánchez-Polo M, Ferro-García MÁ, Prados-Joya G, Ocampo-Pérez R. Pharmaceuticals as emerging contaminants and their removal from water. A review. Chemosphere. 2013;93(7):1268–87.

9. Ocampo-Pérez R, Rivera-Utrilla J, Sánchez-Polo M, López-Peñalver JJ, Leyva-Ramos R. Degradation of antineoplastic cytarabine in aqueous solution by gamma radiation. Chem Eng J. 2011;174(1):1–8.

10. Kümmerer K. The presence of pharmaceuticals in the environment due to human use - present knowledge and future challenges. J Environ Manage. 2009;90(8):2354–66.

11. Kolpin DW, Furlong ET, Meyer MT, Thurman EM, Zaugg SD, Barber LB, et al. Pharmaceuticals, hormones, and other organic wastewater contaminants in U.S. streams, 1999-2000: A national reconnaissance. Environ Sci Technol. 2002;36(6):1202–11.

12. Yuan F, Hu C, Hu X, Qu J, Yang M. Degradation of selected pharmaceuticals in aqueous solution with UV and UV/H2O2. Water Res. 2009;43(6):1766–74.

13. Yuan D, Zhang T, Guo Q, Qiu F, Yang D, Ou Z. A novel hierarchical hollow SiO_2@MnO_2 cubes reinforced elastic polyurethane foam for the highly efficient removal of oil from water. Chem Eng J. 2017;327(61):539–47.

14. Park H, May A, Portilla L, Dietrich H, Münch F, Rejek T, et al. Magnetite nanoparticles as efficient materials for removal of glyphosate from water. Nat

Sustain. 2020;3(2):129–35.

15. Halik M, Sarcletti M, Zahn D. Magnetic water cleaning. Nachrichten aus der Chemie. 2021;69(9):43–6.

16. Yan J, Smith JE, Wang K, He X, Wang L, Tan W. Dye-doped nanoparticles for bioanalysis. Elsevier. 2007;2(3):44–50.

17. Gul S, Khan SB, Rehman IU, Khan MA, Khan MI. A Comprehensive Review of Magnetic Nanomaterials Modern Day Theranostics. Front Mater. 2019;6(179):1–15.

18. Alvarez, Pedro J J. Xiaolei, Qu. Jonathon, Brame. Qilin L. Nanotechnology for a Safe and Sustainable Water Supply : Enabling Integrated Water Treatment and Reuse. Acc Chem Res. 2013;46(3):834–43.

19. Pan BO, Xing B. Adsorption Mechanisms of Organic Chemicals on Carbon Nanotubes. Environ Sci Technol. 2008;42(24):9005–13.

20. Yang KUN, Wu W, Jing Q, Zhu L. Aqueous Adsorption of Aniline , Phenol , and their Substitutes by Multi-Walled Carbon Nanotubes. Environ Sci Technol. 2008;42(21):7931–6.

21. Ji L, Chen W, Duan L, Zhu D. Mechanisms for strong adsorption of tetracycline to carbon nanotubes: A comparative study using activated carbon and graphite as adsorbents. Environ Sci Technol. 2009;43(7):2322–7.

22. Rao GP, Lu C, Su F. Sorption of divalent metal ions from aqueous solution by carbon nanotubes : A review. Elsevier. 2007;58(1):224–31.

23. Yang K, Xing B. Adsorption of organic compounds by carbon nanomaterials in aqueous phase: Polanyi theory and its application. Chem Rev. 2010;110(10):5989–6008.

24. Kumari P, Alam M, Siddiqi WA. Usage of nanoparticles as adsorbents for waste water treatment: An emerging trend. Sustain Mater and Technol. Elsevier B.V.; 2019;22(10):128

25. Khan I, Saeed K, Khan I. Nanoparticles: Properties, applications and toxicities. Arab J Chem. 2019;12(7):908–31.

26. Winkelmann KBB. Global Perspectives Of Nanoscience and Engineering Education. 1st ed. Kuert, Winkelmann. Bharat B, editor. Melbourne: Springer International Publishing; 2016. 3–20 p.

27. Madras IIT, Roy SC, John S. Environmental Nanotechnology Laboratory. 1st ed. Eric, Lichtfouse. Jan, Schwarzbauer. Didier R, editor. Vol. 1. Vellore: Springer International Publishing; 2000. 75–124

28. Liang H, Chen W, Wang R, Qi Z, Mi J, Wang Z. X-shaped hollow α-FeOOH penetration twins and their conversion to α-Fe2O3 nanocrystals bound by high-index facets with enhanced photocatalytic activity. Chem Eng J. 2015;274(1):224–30.

29. Andreescu S, Njagi J, Ispas C, Ravalli MT. JEM spotlight: Applications of advanced nanomaterials for environmental monitoring. J Environ Monit.

2009;11(1):27–40.

30. Singh T, Shukla S, Kumar P, Wahla V, Bajpai VK. Application of nanotechnology in food science: Perception and overview. Front Microbiol. 2017;8(1501):1–7.

31. Qu X, Alvarez PJJ, Li Q. Applications of nanotechnology in water and wastewater treatment. Water Res [Internet]. 2013;47(12):3931–46.

32. Theron J, Walker JA, Cloete TE. Nanotechnology and water treatment: Applications and emerging opportunities. Crit Rev Microbiol. 2008;34(1):43–69.

33. Adegoke AA, Stenström TA. Metal oxide nanoparticles in removing residual pharmaceutical products and pathogens from water and wastewater. In: A, A, Adegoke. T, A A, editor. Nanoparticles in Pharmacotherapy. 1st ed. Durban: Elsevier; 2019. p. 561–89.

34. Anjum M, Miandad R, Waqas M, Gehany F, Barakat MA. Remediation of wastewater using various nano-materials. Arab J Chem. 2019;12(8):4897–919.

35. Mukhopadhyay R, Bhaduri D, Sarkar B, Rusmin R, Hou D, Khanam R, et al. Clay–polymer nanocomposites: Progress and challenges for use in sustainable water treatment. J Hazard Mater. 2020;383(1):121–5.

36. Hasbullah H, Sabri NSM, Said N, Rosid SM, Roslan MI, Ismail AF, et al. 16 - Nanoengineered Materials for Water and Wastewater Treatments. Nanotechnol Water Wastewater Treat Theory Appl. 2018;5(12):303–35.

37. Baruah A, Chaudhary V, Malik R, Tomer VK. 17 -Nanotechnology Based Solutions for Wastewater Treatment. Nanotechnology in Water and Wastewater Treatment: Theory and Applications. Elsevier Inc.; 2018.5(13):337–368

38. Manikandan S, Karmegam N, Subbaiya R, Karthiga Devi G, Arulvel R, Ravindran B, et al. Emerging nano-structured innovative materials as adsorbents in wastewater treatment. Bioresour Technol. 2021;320(1):124–394.

39. Ling L, Huang XY, Zhang WX. Enrichment of Precious Metals from Wastewater with Core–Shell Nanoparticles of Iron. Adv Mater. 2018;30(17):1–6.

40. Anastasiou E, Lorentz KO, Stein GJ, Mitchell PD. Prehistoric schistosomiasis parasite found in the Middle East. Lancet Infect Dis. 2014;14(7):553–4.

41. El Sayed Zaki M. Nanotechnology and Advances in Medicine. Nanotechnology and Advances in Medicine. 2011;6(5):89–117.

42. Gaur M, Misra C, Yadav AB, Swaroop S, Maolmhuaidh F, Bechelany M, et al. Biomedical applications of carbon nanomaterials: Fullerenes, quantum dots, nanotubes, nanofibers, and graphene. Materials (Basel). 2021;14(20):5978.

43. Hao Y, Teja AS. Continuous hydrothermal crystallization of Fe_2O_3 and Co_3O_4 nanoparticles. Mater Res Soc. 2014;18(2):415–22.

44. Hao Y, Teja AS. Continuous hydrothermal crystallization of alpha-Fe_2O_3 and CoO_4 nanoparticles. 2003;100(3):415–22.

45. Pinkas J, Reichlova V, Zboril R, Moravec Z, Bezdicka P, Matejkova J. Sonochemical synthesis of amorphous nanoscopic iron(III) oxide from $Fe(acac)_3$. Ultrason Sonochem. 2008;15(3):257–64.

46. Ali A, Zafar H, Zia M, ul Haq I, Phull AR, Ali JS, et al. Synthesis, characterization, applications, and challenges of iron oxide nanoparticles. Nanotechnol Sci Appl. 2016;9(1):49–67.

47. Wu S, Sun A, Zhai F, Wang J, Xu W, Zhang Q, et al. Fe_3O_4 magnetic nanoparticles synthesis from tailings by ultrasonic chemical co-precipitation. Mater Lett. 2011;65(12):1882–4.

48. Wu W, He Q, Jiang C. Magnetic iron oxide nanoparticles: Synthesis and surface functionalization strategies. Nanoscale Res Lett. 2008;3(11):397–415.

49. Cuenya BR. Synthesis and catalytic properties of metal nanoparticles: Size, shape, support, composition, and oxidation state effects. Thin Solid Films. 2010;518(12):3127–50.

50. Narayanan KB, Sakthivel N. Biological synthesis of metal nanoparticles by microbes. Adv Colloid Interface Sci. 2010;156(1–2):1–13.

51. Parveen K, Banse V, Ledwani L. Green synthesis of nanoparticles: Their advantages and disadvantages. AIP Conf Proc. 2016;1724(1):2564–965.

52. Samrot A V, Sai C, A JS, Keeyari S. Current Research in Green and Sustainable Chemistry A review on synthesis , characterization and potential biological applications of superparamagnetic iron oxide nanoparticles. Curr Res Green Sustain Chem. 2021;4(11):1000-42.

53. Dadfar SM, Roemhild K, Drude NI, Von S. Iron Oxide Nanoparticles : Diagnostic , Therapeutic and Theranostic Applications. Adv Drug Deliv Rev. 2020;138(5):302–25.

54. Fernández-Barahona I, Muñoz-Hernando M, Herranz F. Microwave-driven synthesis of iron-oxide nanoparticles for molecular imaging. Molecules. 2019;24(7):1224.

55. Surowiec Z, Budzyński M, Durak K, Czernel G. Synthesis and characterization of iron oxide magnetic nanoparticles. Nukleonika. 2017;62(2):73–7.

56. Bala R, Dixit A, Pareek B, Singh J, Chaudhary A, Arora S, et al. Synthesis and biochemical characterization of iron oxide nanoparticles. Ann Biol. 2021;37(2):148–52.

57. Justin C, Philip SA, Samrot A V. Synthesis and characterization of superparamagnetic iron-oxide nanoparticles (SPIONs) and utilization of SPIONs in X-ray imaging. Appl Nanosci. 2017;7(7):463–75.

58. Ahn T, Kim JH, Yang HM, Lee JW, Kim JD. Formation pathways of magnetite nanoparticles by coprecipitation method. J Phys Chem C. 2012;116(10):6069–76.

59. De Freitas JC, Branco RM, Lisboa IGO, Da Costa TP, Campos MGN, Júnior MJ, et al. Magnetic nanoparticles obtained by homogeneous coprecipitation sonochemically assisted. Mater Res. 2015;18(2):220–4.

60. Mohapatra SK, Misra M, Mahajan VK, Raja KS. A novel method for the synthesis of titania nanotubes using sonoelectrochemical method and its application for photoelectrochemical splitting of water. J Catal. 2007;246(2):362–9.

61. Mascolo MC, Pei Y, Ring TA. Room Temperature Co-Precipitation Synthesis of Magnetite Nanoparticles in a Large ph Window with Different Bases. Materials (Basel). 2013;6(12):5549–67.

62. Massart R. Preparation of Aqueous Magnetic Liquids in Alkaline and Acidic Media. IEEE Trans Magn. 1981;17(2):1247–8.

63. Roca AG, Morales MP, Serna CJ. Synthesis of Monodispersed Magnetite Particles From Different Organometallic Precursors. IEEE Trans Magn. 2006;42(10):3025–9.

64. Kumar NS, Kumar KV. Synthesis and Structural Properties of Bismuth Doped Cobalt Nanoferrites Prepared by Sol-Gel Combustion Method. World J Nano Sci Eng. 2015;5(4):140–51.

65. Bustamante-torres M, Romero-fierro D, Estrella-nuñez J, Arcentales-vera B, Chichande-proaño E, Bucio E. Polymeric Composite of Magnetite Iron Oxide Nanoparticles and Their Application in Biomedicine : A Review. Polymers (Basel). 2022;14(752):1–26.

66. Samrot A V, Sai C, A JS, Keeyari S. Current Research in Green and Sustainable Chemistry A review on synthesis , characterization and potential biological applications of superparamagnetic iron oxide nanoparticles. Curr Res Green Sustain Chem. 2021;4(1):1000-42.

67. Malo De Molina P, Zhang M, Bayles A V., Helgeson ME. Oil-in-Water-in-Oil Multinanoemulsions for Templating Complex Nanoparticles. Nano Lett. 2016;16(12):7325–32.

68. Cai H, An X, Cui J, Li J, Wen S, Li K, et al. Facile hydrothermal synthesis and surface functionalization of polyethyleneimine-coated iron oxide nanoparticles for biomedical applications. ACS Appl Mater Interfaces. 2013;5(5):1722–31.

69. Madadlou A, Jaberipour S, Eskandari MH. Nanoparticulation of enzymatically cross-linked whey proteins to encapsulate caffeine via microemulsification/heat gelation procedure. LWT - Food Sci Technol. 2014;57(2):725–30.

70. Yelenich O V., Solopan SO, Kolodiazhnyi T V., Greneche JM, Belous AG. Synthesis of iron oxide nanoparticles by different methods and study of their properties. Solid State Phenom. 2015;230(10):108–13.

71. Hayashi H, Hakuta Y. Hydrothermal Synthesis of Metal Oxide Nanoparticles in Supercritical Water. Materials (Basel). 2010;3(9):3794–817.

72. Takami S, Sato T, Mousavand T, Ohara S, Umetsu M, Adschiri T. Hydrothermal synthesis of surface-modified iron oxide nanoparticles. Mater Lett. 2007;61(6):4769–72.

73. Vatta LL, Sanderson RD, Koch KR. Magnetic Nanoparticles : Properties and Potential Applications Magnetic nanoparticles : Properties and potential applications *. Pure Appl Chem. 2006;78(9):1793–801.

74. Xu C, Lee J, Teja AS. Continuous hydrothermal synthesis of lithium iron phosphate particles in subcritical and supercritical water. Elsevier. 2008;44(1):92–7.

75. Guo Y, Wang Z, Shao H, Jiang X. Hydrothermal synthesis of highly fluorescent carbon nanoparticles from sodium citrate and their use for the detection of mercury ions. Carbon N Y. 2012;52(8):583–9.

76. Naghibi S, Ali M, Sani F, Reza H, Hosseini M. Application of the statistical Taguchi method to optimize TiO2 nanoparticles synthesis by the hydrothermal assisted sol-gel technique. Ceram Int. 2013;8(77):1–30.

77. Lopez Perez JA, Lopez Quintela MA, Mira J, Rivas J, Charles SW. Advances in the preparation of magnetic nanoparticles by the microemulsion method. J Phys Chem B. 1997;101(41):8045–7.

78. James M, Revia RA, Stephen Z, Zhang M. Microfluidic synthesis of iron oxide nanoparticles. Nanomaterials. 2020;10(11):1–19.

79. Santra S, Tapec R, Theodoropoulou N, Dobson J, Hebard A, Tan W. Synthesis and characterization of silica-coated iron oxide nanoparticles in microemulsion: The effect of nonionic surfactants. Langmuir. 2001;17(10):2900–6.

80. Chin AB, Yaacob II. Synthesis and characterization of magnetic iron oxide nanoparticles via w/o microemulsion and Massart's procedure. J Mater Process Technol. 2007;191(1–3):235–7.

81. Tartaj P, Del Puerto Morales M, Veintemillas-Verdaguer S, González-Carreño T, Serna CJ. The preparation of magnetic nanoparticles for applications in biomedicine. J Phys D Appl Phys. 2003;36(13):3727–42.

82. Sheikh L, Vohra R, Verma AK, Nayar S. Biomimetically Synthesized Aqueous Ferrofluids Having Antibacterial and Anticancer Properties. Mater Sci Appl. 2015;06(3):242–50.

83. Lam UT, Mammucari R, Suzuki K, Foster NR. Processing of iron oxide nanoparticles by supercritical fluids. Ind Eng Chem Res. 2008;47(3):599–614.

84. Kojima K, Miyazaki M, Mizukami F, Maeda K. Selective Formation of Spinel Iron Oxide in Thin Films by Complexing Agent-Assisted Sol-Gel Processing. J Sol-Gel Sci Technol. 1997;8(3):77–81.

85. Thiagarajan S, Sanmugam A, Vikraman D. Facile Methodology of Sol-Gel Synthesis for Metal Oxide Nanostructures. Recent Appl Sol-Gel Synth. 2017;4(10):1–16.

86. Thakur P, Taneja S, Sindhu D, Lüders U, Sharma A, Ravelo B, et al. Manganese Zinc Ferrites : a Short Review on Synthesis and Characterization. J Supperconductivity Nov Magn. 2020;10(21):1023–40.

87. Ennas G, Musinu A, Piccaluga G, Zedda D, Gatteschi D, Sangregorio C, et al. Characterization of Iron Oxide Nanoparticles in an Fe2O3-SiO2 Composite Prepared by a Sol-Gel Method. Chem Mater. 1998;10(2):495–502.

88. Laurent S, Forge D, Port M, Roch A, Robic C, Vander Elst L, et al. Magnetic iron oxide nanoparticles: Synthesis, stabilization, vectorization, physicochemical characterizations and biological applications. Chem Rev. 2008;108(6):2064–110.

89. Gonzales-Weimuller M, Zeisberger M, Krishnan KM. Size-dependant heating

rates of iron oxide nanoparticles for magnetic fluid hyperthermia. J Magn Magn Mater. 2009;321(13):1947–50.

90. Hyeon T, Su Seong Lee, Park J, Chung Y, Hyon Bin Na. Synthesis of highly crystalline and monodisperse maghemite nanocrystallites without a size-selection process. J Am Chem Soc. 2001;123(51):12798–801.

91. Ansari SAMK, Ficiarà E, Ruffinatti FA, Stura I, Argenziano M, Abollino O, et al. Magnetic iron oxide nanoparticles: Synthesis, characterization and functionalization for biomedical applications in the Central Nervous System. Materials (Basel). 2019;12(3):465–94.

92. Kruis FE, Fissan H, Peled A. Synthesis of Nanoparticles in the gas phase for electronic, optical and magnetic applications - A review. 1998;29(5):511–35.

93. Bauri R, Yadav D. Metal matrix composites by friction stir processing. Metal Matrix Composites by Friction Stir Processing. Elsevier Inc.; 2017;15(3):1–119 p.

94. Mattox DM. Ion plating - past, present and future. Surf Coatings Technol. 2000;134(23):517–21.

95. González-Carreño T, Morales MP, Gracia M, Serna CJ. Preparation of uniform γ-Fe2O3 particles with nanometer size by spray pyrolysis. Mater Lett. 1993;18(3):151–5.

96. Tavakoli A, Sohrabi M, Kargari A. A Review of Methods for Synthesis of Nanostructured Metals with Emphasis on Iron Compounds. Chem Rev. 2007;61(3):151–70.

97. Liu P, Cai W, Zeng H. Fabrication and size-dependent optical properties of FeO nanoparticles induced by laser ablation in a liquid medium. J Phys Chem C. 2008;112(9):3261–6.

98. Franzel L, Bertino MF, Huba ZJ, Carpenter EE. Synthesis of magnetic nanoparticles by pulsed laser ablation. Appl Surf Sci. 2012;261(89):332–6.

99. Maneeratanasarn P, Van Khai T, Kim SY, Choi BG, Shim KB. Synthesis of phase-controlled iron oxide nanoparticles by pulsed laser ablation in different liquid media. Phys Status Solidi Appl Mater Sci. 2013;210(3):563–9.

100. Hou Y, Xu Z, Sun S. Controlled Synthesis and Chemical Conversions of FeO Nanoparticles. Angew Chemie. 2007;119(10):6445–8.

101. Yang GW. Laser ablation in liquids: Applications in the synthesis of nanocrystals. Prog Mater Sci. 2007;52(4):648–98.

102. Amendola V, Meneghetti M. Laser ablation synthesis in solution and size manipulation of noble metal nanoparticles. Phys Chem Chem Phys. 2009;11(56):3805–21.

103. Amendola V, Riello P, Meneghetti M. Magnetic nanoparticles of iron carbide, iron oxide, iron@iron oxide, and metal iron synthesized by laser ablation in organic solvents. J Phys Chem C. 2011;115(12):5140–6.

104. Amendola V, Riello P, Polizzi S, Fiameni S, Innocenti C, Sangregorio C, et al.

Magnetic iron oxide nanoparticles with tunable size and free surface obtained via a “green” approach based on laser irradiation in water. J Mater Chem. 2011;21(46):18665–73.

105. Willmott PR, Huber JR. Pulsed laser vaporization and deposition. Rev Mod Phys. 2000;72(1):315–28.

106. Zysler RD, Fiorani D, Testa AM. Investigation of magnetic properties of interacting Fe2O3 nanoparticles. J Magn Magn Mater. 2001;224(1):5–11.

107. Hassanien H, Darweesh M. Nanomaterials : Classification and Properties-Part I. Nanomaterials. 2018;1(1):1–11.

108. Senthil Kumar P, Narayan AS, Dutta A. Nanochemicals and Effluent Treatment in Textile Industries. 3rd ed. Senthil Kumar, P. Abishek S NAD, editor. Chennai: Springer International Publishing; 2017. 57–96.

109. Samrot A V., Sahithya CS, Selvarani A J, Purayil SK, Ponnaiah P. A review on synthesis, characterization and potential biological applications of superparamagnetic iron oxide nanoparticles. Curr Res Green Sustain Chem. 2021;4(20):1000–42.

110. Rosei F. Nanostructured surfaces: Challenges and frontiers in nanotechnology. J Phys Condens Matter. 2004;16(17):1373–436.

111. Stafiej A, Pyrzynska K. Adsorption of heavy metal ions with carbon nanotubes. Sep Purif Technol. 2007;58(1):49–52.

112. Shubayev VI, Pisanic TR, Jin S. Magnetic nanoparticles for theragnostics. Adv Drug Deliv Rev. 2009;61(6):467–77.

113. GIUSTINI AJ, PETRYK AA, CASSIM SM, TATE JA, BAKER I, HOOPES PJ. Magnetic Nanoparticle Hyperthermia in Cancer Treatment. Nano Life. 2010;1(2):17–32.

114. Bae YH, Park K. Targeted drug delivery to tumors: Myths, reality and possibility. J Control Release. 2011;153(3):198–205.

115. Veiseh O, Gunn JW, Zhang M. Design and fabrication of magnetic nanoparticles for targeted drug delivery and imaging. Adv Drug Deliv Rev. 2010;62(3):284–304.

116. Venkateswarlu S, Kumar BN, Prathima B, SubbaRao Y, Jyothi NVV. A novel green synthesis of Fe_3O_4 magnetic nanorods using Punica Granatum rind extract and its application for removal of Pb(II) from aqueous environment. Arab J Chem. 2019;12(4):588–96.

117. Baldez EE, Robaina NF, Cassella RJ. Study of rhodamine b retention by polyurethane foam from aqueous medium in presence of sodium dodecylsulfate. Sep Sci Technol. 2009;44(13):3128–49.

118. Kosanke RM. Metallic nanostructures from controlled synthesis to applications. 2nd ed. Yujie, Xiong. Xianmao L, editor. Anhui: Springer International Publishing; 2019. 49–74 p.

119. Jans H, Huo Q. Gold nanoparticle-enabled biological and chemical detection

and analysis. Chem Soc Rev. 2012;41(7):2849–66.

120. Antoniammal P, Arivuoli D. Gallium Nitride Nanoparticles. J Nanomater. 2012;6(13):1–11.

121. Singh M, Lara S, Tlali S. Effects of size and shape on the specific heat , melting entropy and enthalpy of nanomaterials. Integr Med Res. 2016;9(11):1–8.

122. Yang X, Hong H, Grailer JJ, Rowland IJ, Javadi A, Hurley SA, et al. CRGD-functionalized, DOX-conjugated, and 64Cu-labeled superparamagnetic iron oxide nanoparticles for targeted anticancer drug delivery and PET/MR imaging. Biomaterials. 2011;32(17):4151–60.

123. Lee H, Mi KY, Park S, Moon S, Jung JM, Yong YJ, et al. Thermally cross-linked superparamagnetic iron oxide nanoparticles: Synthesis and application as a dual imaging probe for cancer in vivo. J Am Chem Soc. 2007;129(42):12739–45.

124. Meziane D, Elias A, Guénin E. Rapid and Efficient Synthesis of ω-Alkylenediphosphoric Acids from Phosphorus Oxychloride. J Chem. 2016;2016(55):1–8.

125. Kuiper JM, Hulst R, Engberts JBFN. A Selective and Mild Synthetic Route to Dialkyl Phosphates. Synthesis (Stuttg). 2003;34(28):695–8.

126. Miller D, Wiener EM, Turowski A, Thunig C, Hoffmann H. O/W emulsions for cosmetics products stabilized by alkyl phosphates - Rheology and storage tests. Colloids Surfaces A Physicochem Eng Asp. 1999;152(1–2):155–60.

127. Li H, Jin Y, Fan B, Qi R, Cheng X, Peng S. Synthesis and surface activity of mono- and diphosphate ester mixture with different alkyl chain length. J Dispers Sci Technol. 2017;38(5):704–11.

128. Dueymes C, Pirat C, Pascal R. Facile synthesis of simple mono-alkyl phosphates from phosphoric acid and alcohols. Tetrahedron Lett. 2008;49(36):5300–1.

129. Sarcletti M, Vivod D, Luchs T, Rejek T, Portilla L, Müller L, et al. Superoleophilic Magnetic Iron Oxide Nanoparticles for Effective Hydrocarbon Removal from Water. Adv Funct Mater. 2019;29(15):1–7.

130. Zaytseva MP, Muradova AG, Sharapaev AI, Yurtov E V., Grebennikov IS, Savchenko AG. Fe_3O_4/SiO_2 Core Shell Nanostructures: Preparation and Characterization. Russ J Inorg Chem. 2018;63(12):1684–8.

131. Xu Y, Zhou Y, Ma W, Wang S. A fluorescent sensor for zinc detection and removal based on core-shell functionalized $Fe_3O_4@SiO_2$ nanoparticles. J Nanomater. 2013;25(3):1–6.

132. Punia P, Bharti MK, Chalia S, Dhar R, Ravelo B, Thakur P, et al. Recent advances in synthesis, characterization, and applications of nanoparticles for contaminated water treatment- A review. Ceram Int. 2021;47(2):1526–50.

133. Petcharoen K, Sirivat A. Synthesis and characterization of magnetite nanoparticles via the chemical co-precipitation method. Mater Sci Eng B Solid-State Mater Adv Technol. 2012;177(5):421–7.

134. Park H, May A, Portilla L, Dietrich H, Münch F, Rejek T, et al. Magnetite nanoparticles as efficient materials for removal of glyphosate from water. Nat Sustain. 2020;3(2):129–35.

135. Sahoo Y, Pizem H, Fried T, Golodnitsky D, Burstein L, Sukenik CN, et al. Alkyl Phosphonate / Phosphate Coating on Magnetite Nanoparticles : A Comparison with Fatty Acids. Langmuir. 2001;17(23):7907–11.

136. Gosens I, Post JA, Jj L, Fonteyne D, Jansen EHJM, Geus JW, et al. Impact of agglomeration state of nano- and submicron sized gold particles on pulmonary inflammation. Part Fibre Toxicol. 2010;7(1):37. 7

137. Afkhami A, Saber-tehrani M, Bagheri H. Modi fi ed maghemite nanoparticles as an ef fi cient adsorbent for removing some cationic dyes from aqueous solution. DES. 2010;263(1–3):240–8.

138. Gugushe AS, Mpupa A, Nomngongo PN. Ultrasound-assisted magnetic solid phase extraction of lead and thallium in complex environmental samples using magnetic multi-walled carbon nanotubes/zeolite nanocomposite. Microchem J [Internet]. 2019;149(5):1039-60.

139. Antonio J, Costa-Filho. Daniel Reinaldo, Cornejo. Ernanni, Viera. Lionel Frnel G. Synthesis and characterization of magnetite nanoparticles coated with lauric Synthesis and characterization of magnetite nanoparticles coated with lauric acid. Mater Charact. 2013;81(7):28–36.

140. Jannah NR, Onggo D. Synthesis of Fe3O4 nanoparticles for colour removal of printing ink solution. J Phys Conf Ser. 2019;1245(1):2–6.

141. Ghaedi M, Ghaedi AM, Hossainpour M, Ansari A, Habibi MH, Asghari AR. Least square-support vector (LS-SVM) method for modeling of methylene blue dye adsorption using copper oxide loaded on activated carbon: Kinetic and isotherm study. J Ind Eng Chem. 2014;20(4):1641–9.

142. Yamini Y, Faraji M, Rajabi AA, Nourmohammadian F. Ultra efficient removal of Basic Blue 41 from textile industry’s wastewaters by sodium dodecyl sulphate coated magnetite nanoparticles: Removal, kinetic and isotherm study. Anal Bioanal Chem Res. 2018;5(2):205–15.

143. Keyhanian F, Shariati S, Faraji M, Hesabi M. Magnetite nanoparticles with surface modification for removal of methyl violet from aqueous solutions. Arab J Chem. 2016;9(4):348–54.

144. Ghaedi M, Nasab AG, Khodadoust S, Rajabi M, Azizian S. Journal of Industrial and Engineering Chemistry Application of activated carbon as adsorbents for efficient removal of methylene blue : Kinetics and equilibrium study. J Ind Eng Chem. 2014;20(4):2317–24.

145. Kannan N, Sundaram MM. Kinetics and mechanism of removal of methylene blue by adsorption on various carbons — a comparative study. Dye Pigment. 2001;51(8):25–40.

146. Rida K, Bouraoui S, Hadnine S. Applied Clay Science Adsorption of methylene blue from aqueous solution by kaolin and zeolite. Appl Clay Sci. 2013;84(83):99–105.

147. Makayonke NT. The Use of Carbon Nanotubes Co-Polymerized With Calixarenes for the Removal of Cadmium and Organic Contaminants From Water. 1st ed. Makayonke NT, editor. [Johannesburg]: University of Johannesburg; 2010. Thesis

148. Rajoriya S, Kumar V, Singh A, Nigam M, Roy K. Adsorption of methyl red dye from aqueous solution onto eggshell waste material : Kinetics , isotherms and thermodynamic studies. Curr Res Green Sustain Chem. 2021;4(9):1001–80.

149. Hameed BH, Ahmad AA. Batch adsorption of methylene blue from aqueous solution by garlic peel , an agricultural waste biomass. Chem Eng J. 2009;164(2009):870–5.

150. Khalid D, Amran M, Salleh M, Azlina W, Abdul W, Idris A, et al. Batch adsorption of basic dye using acid treated kenaf fibre char : Equilibrium , kinetic and thermodynamic studies. Chem Eng J. 2012;182(89):449–57.

151. Wang L, Zhang J, Wang A. Fast removal of methylene blue from aqueous solution by adsorption onto chitosan- g -poly (acrylic acid)/ attapulgite composite. DES. 2011;266(1–3):33–9.

152. Elkady MF, Ibrahim AM, El-latif MMA. Assessment of the adsorption kinetics , equilibrium and thermodynamic for the potential removal of reactive red dye using eggshell biocomposite beads. DES. 2011;278(1–3):412–23.

153. Go V, Ferna C. Porous texture of activated carbons prepared by phosphoric acid activation of woods. 2004;238(15):309–13.

154. Nandi BK, Goswami A, Purkait MK. Applied Clay Science Removal of cationic dyes from aqueous solutions by kaolin : Kinetic and equilibrium studies. Appl Clay Sci. 2009;42(3–4):583–90.

155. Kalavathy MH, Miranda LR. Comparison of copper adsorption from aqueous solution using modi fi ed and unmodi fi ed Hevea brasiliensis saw dust. DES. 2010;255(3):165–74.

156. Wang P, Cao M, Wang C, Ao Y, Hou J, Qian J. Kinetics and thermodynamics of adsorption of methylene blue by a magnetic graphene-carbon nanotube composite. Appl Surf Sci. 2014;290(50):116–24.

157. Gong J, Wang B, Zeng G, Yang C, Niu C, Niu Q. Removal of cationic dyes from aqueous solution using magnetic multi-wall carbon nanotube nanocomposite as adsorbent. Hazard Mater. 2009;164:1517–22.

158. Zhou L, Huang J, He B, Zhang F, Li H. Peach gum for efficient removal of methylene blue and methyl violet dyes from aqueous solution. Carbohydr Polym. 2014;101(1):574–81.

159. Liu T, Li Y, Du Q, Sun J, Jiao Y, Yang G, et al. Adsorption of methylene blue from aqueous solution by graphene. Colloids Surfaces Biointerfaces [. 2012;90(1):197–203.

160. Guiza S, Bagane M, Al-Soudani AH, Amore H Ben. Adsorption of basic dyes onto natural clay. Adsorpt Sci Technol. 2004;22(3):245–56.

161. Fan W, Gao W, Zhang C, Tjiu WW, Pan J, Liu T. Hybridization of graphene

sheets and carbon-coated Fe3O 4 nanoparticles as a synergistic adsorbent of organic dyes. J Mater Chem. 2012;22(48):25108–15.

162. Yang N, Zhu S, Zhang D, Xu S. Synthesis and properties of magnetic Fe3O4-activated carbon nanocomposite particles for dye removal. Mater Lett. 2008;62(4–5):645–7.

163. Li DP, Zhang YR, Zhao XX, Zhao BX. Magnetic nanoparticles coated by aminoguanidine for selective adsorption of acid dyes from aqueous solution. Chem Eng J. 2013;232:425–33.

164. Munonde TS, Maxakato NW, Nomngongo PN. Preconcentration and speciation of chromium species using ICP-OES after ultrasound-assisted magnetic solid phase extraction with an amino-modified magnetic nanocomposite prepared from Fe_3O_4, MnO_2 and Al_2O_3. Microchim Acta. 2017;184(4):1223–32.

165. Pourghazi K, Amoli-diva M, Beiraghi A. Speciation of ultra-trace amounts of inorganic arsenic in water and rice samples by electrothermal atomic absorption spectrometry after solid-phase extraction with modified Fe_3O_4 nanoparticles. Int J Environ Anal Chem. 2015;95(4):324–38.

166. Guernelli S, Laganà MF, Mezzina E, Ferroni F, Siani G, Spinelli D. Supramolecular Complex Formation: A Study of the Interactions between β-Cyclodextrin and Some Different Classes of Organic Compounds by ESI-MS, Surface Tension Measurements, and UV/Vis and 1H NMR Spectroscopy. European J Org Chem. 2003;(24):4765–76.

167. Nwambaekwe KC. Tellurium Attenuation of Kesterite Band Gap for Improved Photovoltaic Efficiency. University of theWestern Cape; 2018. Thesis

168. Inkson BJ. Scanning Electron Microscopy (SEM) and Transmission Electron Microscopy (TEM) for Materials Characterization [Internet]. 1st ed. Inkson BJ, editor. Materials Characterization Using Nondestructive Evaluation (NDE) Methods. Sheffield: Elsevier Ltd; 2016. 17–43.

169. Escalante CF, Fabian C, Sierra E. Fundamentals of transmission electron microscopy, the technique with the best resolution in the world. Screen [Internet]. 2019;2(9):10–8. Available from: https://www.researchgate.net/publication/330999184

170. Evanoff DD, Chumanov G. Synthesis and optical properties of silver nanoparticles and arrays. ChemPhysChem. 2005;6(7):1221–31.

171. Labbé N, De Jéso B, Lartigue JC, Daudé G, Pétraud M, Ratier M. Time-domain 1H NMR characterization of the liquid phase in greenwood. Holzforschung. 2006;60(3):265–70.

172. Berthomieu C, Hienerwadel R. Fourier transform infrared (FTIR) spectroscopy. Photosynth Res. 2009;101(3):157–70.

173. Whittig LD, Allardice WR. X-ray diffraction techniques. Methods Soil Anal Part 1 Phys Mineral Methods. 2018;9(9):331–62.

174. Dempster AJ. New Methods in Mass Spectroscopy. Proc Am Philos Soc. 1935;75(8):755–67.

175. Ngo PD. Energy Dispersive Spectroscopy. Fail Anal Integr Circuits. 1999;494(7):205–15.

176. Verşan Kök M, Varfolomeev MA, Nurgaliev DK. Thermal characterization of crude oils in the presence of limestone matrix by TGA-DTG-FTIR. J Pet Sci Eng. 2017;154(7):495–501.

177. (https://serc.carleton.edu/msu_nanotech/nano_intro.html) (accessed on the 20th of October 2022).

178. (https://dreamcivil.com/water-treatment-process/) (accessed on the 17th of October 2022).

179. (http://www9.open.ac.uk/emsuite/services/sem-eds-0) (accessed on the 22nd of December 2022).